DEVELOPMENT OF ULTRASOUND-RESPONSIVE BIOGENIC GAS VESICLES AS MULTIFUNCTIONAL THERANOSTIC CARRIERS FOR ENHANCED CANCER THERAPY

SONG LIN

The Hong Kong Polytechnic University

2020

The Hong Kong Polytechnic University
Department of Biomedical Engineering

Development of Ultrasound-Responsive Biogenic Gas Vesicles as Multifunctional Theranostic Carriers for Enhanced Cancer Therapy

Song Lin

A thesis submitted in partial fulfillment of the requirements for the degree of Doctor of Philosophy

May 2020

CERTIFICATE OF ORIGINALITY

I hereby declare that this thesis is my own work and that, to the best of my knowledge and belief, it reproduces no material previously published or written, nor material that has been accepted for the award of any other degree or diploma, except where due acknowledgment has been made in the text.

_____

Song Lin

May 2020

ABSTRACT

Nanobubbles, as a kind of special nanoparticles, have been investigated as theranostic particles in cancer nanomedicine. Despite the huge potential of nanobubbles for ultrasonic molecular imaging as well as nanocarrier for gas and drug delivery for tumor therapy, stabilization is still a big limitation of nanobubbles that could affect their function. Gas vesicles (GVs), as a novel kind of nanoparticle, which are naturally occurring gas-filled microcavities, have been demonstrated as the first biomolecular acoustic reporters with gene editability and inherent stability. Here, the theranostic potential of GVs for cancer treatment is investigated in this study.

First, we explored the potential of GVs for tumor imaging. However, this ability is limited by the quick clearance of GVs by the reticuloendothelial system (RES) *in vivo*. Thus, we developed PEGylated HA-GVs (PH-GVs) for in-tumor molecular ultrasound imaging by integrating polyethylene glycol (PEG) and hyaluronic acid (HA) in GV shells. PH-GVs were demonstrated to be able to escape the clearance from the RES and to penetrate tumor vasculature. Further, PH-GVs produced strong ultrasound contrast in the tumor site *in vivo*, with no obvious side-effects detected following intravenous injection. Thus, we demonstrate the potential of PH-GVs as novel, nanosized and targeted UCAs for efficient and specific molecular tumor imaging.

Next, the application of PH-GVs on sonodynamic therapy was further investigated. Sonodynamic therapy (SDT) is a promising alternative treatment method for cancer.

Nanometer-sized GVs have the potential to be a kind of nanosized agent for enhanced cavitation during SDT. Here, the existence of GVs could enhance the production of ROS in the solution, was demonstrated. Besides, GVs were confirmed to be able to enhance SDT both *in vitro* and *in vivo*. Thus, we demonstrated that GVs could function as a kind of targeted nanosized agent for enhanced SDT against cancer.

GVs, as natural gas-filled bubbles, have the potential to be oxygen carriers for tumor therapy. Tumor hypoxia is believed to be a factor limiting successful outcomes of oxygen-consuming cancer therapy, thereby reducing patient survival. In this study, we also explored the potential of biogenic GVs as a new kind of oxygen carrier to alleviate tumor hypoxia. GVs were modified on the surface of their protein shells by a layer of liposome. A substantial improvement of oxygen concentration was observed in subcutaneous tumors when lipid-GVs(O_2) were tail-injected. Significant enhancement of tumor cell apoptosis and necrosis was also observed during photodynamic therapy (PDT) in the presence of lipid-GVs(O_2) both *in vitro* and *in vivo*. In conclusion, lipid-GVs exhibited promising performance for intravenous gas delivery, enhanced PDT efficacy and low toxicity, a quality that may be applied to alleviate hypoxia in cancers, as well as hypoxia-related clinical treatments.

In all, we demonstrate the potential of GVs as novel, nanosized agents for efficient and specific molecular tumor imaging, enhanced SDT as well as oxygen carrier for enhanced PDT, paving the way for the application of GVs in precise and personalized medicine.

LIST OF PUBLICATION AND AWARDS

Journal publications

1. **Song, L.**; Wang, G.; Hou, X.; Kala, S.; Qiu, Z.; Wong, K. F.; Cao, F.; Sun, L., Biogenic nanobubbles for effective oxygen delivery and enhanced photodynamic therapy of cancer. *Acta Biomater* **2020,** *108*, 313-325.

2. Wang, G.*; **Song, L.***; Hou, X.; Kala, S.; Wong, K. F.; Tang, L.; Dai, Y.; Sun, L., Surface-modified GVs as nanosized contrast agents for molecular ultrasound imaging of tumor. Biomaterials 2020, 236, 119803. (co-first author)

3. **Song, L.**; Huang, Y.; Hou, X.; Yang, Y.; Kala, S.; Qiu, Z.; Zhang, R.; Sun, L., PINK1/Parkin-Mediated Mitophagy Promotes Resistance to Sonodynamic Therapy. Cell Physiol Biochem 2018, 49 (5), 1825-1839.

Conference paper

1. **Song, L.**; Wang, G.; Hou, X.; Kala, S.; Qiu, Z.; Sun, L., Development of multifunctional theranostic nanocarrier for enhanced cancer therapy. The International Molecular Imaging Summit 2019 (IMIS), Xiamen, China, 2019/10/18-20. (oral)

2. **Song, L.**; Wang, G.; Hou, X.; Kala, S.; Qiu, Z.; Sun, L., Biogenic gas vesicle-based oxygen delivery for tumor hypoxic microenvironment alteration. International Ultrasonics Symposium (IUS), Kobe, Japan, 2018/10/22-25.

3. **Song, L.**; Wang, G.; Hou, X.; Kala, S.; Qiu, Z.; Sun, L., Biogenic gas vesicle-based oxygen delivery for tumor hypoxic microenvironment alteration. World Molecular Imaging Congress (WMIC), Seattle, USA, 2018/09/12-15.

4. **Song, L.**; Wang, G.; Hou, X.; Kala, S.; Qiu, Z.; Sun, L., Development of ultrasound sensitive gas vesicles for oxygen delivery in cancer therapy. International Conference on Biomedical Engineering 2017 (ICBMU 2017). Hong Kong, 2017/12/02-04.

5. **Song, L.**; Huang, Y.; Hou, X.; Yang, Y.; Kala, S.; Qiu, Z.; Zhang, R.; Sun, L., PINK1/Parkin mediated mitophagy promotes resistance to sonodynamic therapy. The 8th WACBE

World congress on bioengineering. Hong Kong, 2017/07/30-08/02. (oral)

6. **Song, L.**; Huang, Y.; Hou, X.; Yang, Y.; Kala, S.; Qiu, Z.; Zhang, R.; Sun, L., Subcellular localization of sonosensitizer for autophagy cooperated apoptosis in sonodynamic therapy. 17th International Symposium on Therapeutic Ultrasound, Nanjing, China, 2017/05/31-06/02. (oral)

Awards

1. Best **Presentation Award** of 2019 International Molecular Imaging Summit, October 2019, Xiamen, China.

2. Best **Poster Award** of 2019 International Molecular Imaging Summit, October 2019, Xiamen, China.

3. Best student **poster award** of International Conference on Biomedical Ultrasound 2017, December 2017, Hong Kong.

4. The *International Society for Therapeutic Ultrasound* (*ISTU*) conference **travel support**, May 2017, Nanjing, China.

ACKNOWLEDGMENTS

Time flies, I can still remember the first day I entered PolyU, it's a normal day of summer. Now, I can't imagine that I have spent almost four years here in Hong Kong. It's a hard and long journey, I have encountered so many difficulties and frustrations. But I can't deny that I learned so much here among all these years about how to think independently. Still, I have lots of limitations, but I am happy that I have grown up to a certain extent that I can continue my next journey more confidently. Here, I want to express my sincere appreciation to my chief supervisor, associate professor Dr. Lei Sun. Thank you for his patient direction and guidance. Also, I would like to thank my lab mates: Dr. Guo Jinghui, Dr. Liu Cheng, Dr. Qiu Zhihai, Cao Fei, Zhu Jiejun, Xian Quanxiang, Shashwati Kala, Wang Guohao, Huang Yongmin, Hou Xuandi, Zhu Ting, Wong Kin Fung, and Yang Minyi, thank you for their help and suggestion about my project. I will remember the time we spent together to overcome the difficulty of the journey. At final, I would like to thank my dearest parents for their support and caring. Thank you all.

TABLE OF CONTENTS

INDEX OF ABBREVIATIONS

5-aminolevulinic acid	5-ALA
Analysis of variance	ANOVA
Dimethyl sulfoxide	DMSO
Enhanced Permeability and Retention	EPR
Fetal Bovine Serum	FBS
Gas Vesicle	GVs
Photodynamic Therapy	PDT
Photosensitizers	PS
Protoporphyrin IX	PpIX
Propidium Iodide	PI
Phosphate-buffered saline	PBS
Reactive Oxygen Species	ROS
Sonodynamic Therapy	SDT

CHAPTER 1 Introduction

Despite almost a four-decade war against cancer, cancer is still ranking as the first death reason in most countries around the world with a high level of human development. The incidence and mortality of cancer are growing rapidly around the world and there was 18.1 million new cases and 9.6 million deaths from cancer in one year according to World Cancer Report 2019 [1-4] released by World Health Organization (Figure 1.1). This means that more and more people are suffering from cancer as well as a growing heavy financial burden to the whole society.

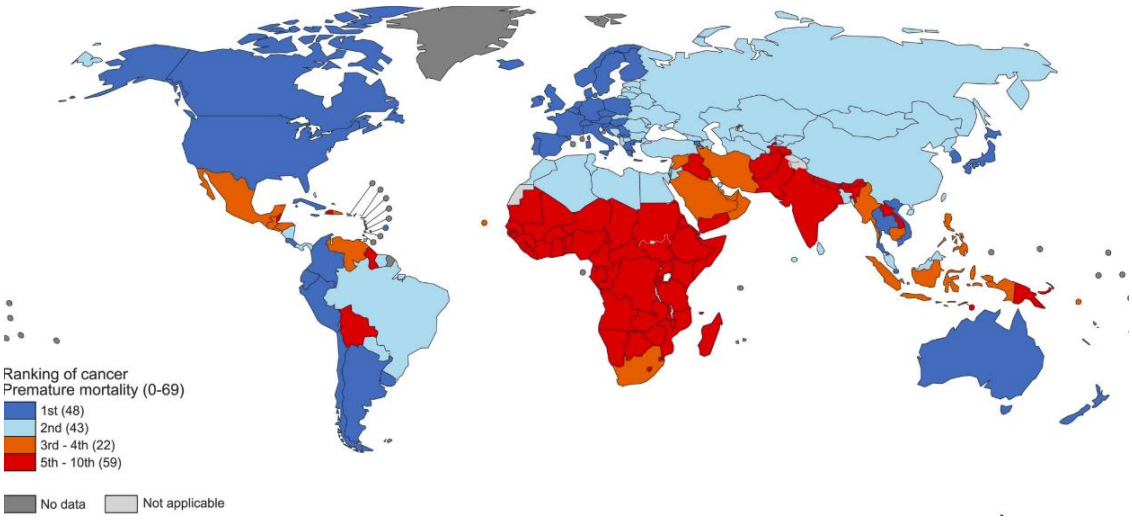

Figure 1.1. Global Map of Cancer Mortality Ranking in 2015. (Adapted from [1])

1.1 Progression of cancer

Cancer begins when cells of the human body undergo uncontrolled growth and spread to surrounding tissues. Several properties make cancer cells totally different

from normal cells. Compared to normal cells, the accumulated abnormalities make cancer cells lose their cell regulatory mechanisms that they keep dividing all the time without further cell differentiation, nor will they begin the process of programmed cell death. Meanwhile, the metabolic way of cancer cells changed, they obtain energy mainly through aerobic glycolysis but not mitochondrial-dependent oxidative phosphorylation (Figure 1.2)[5-8].

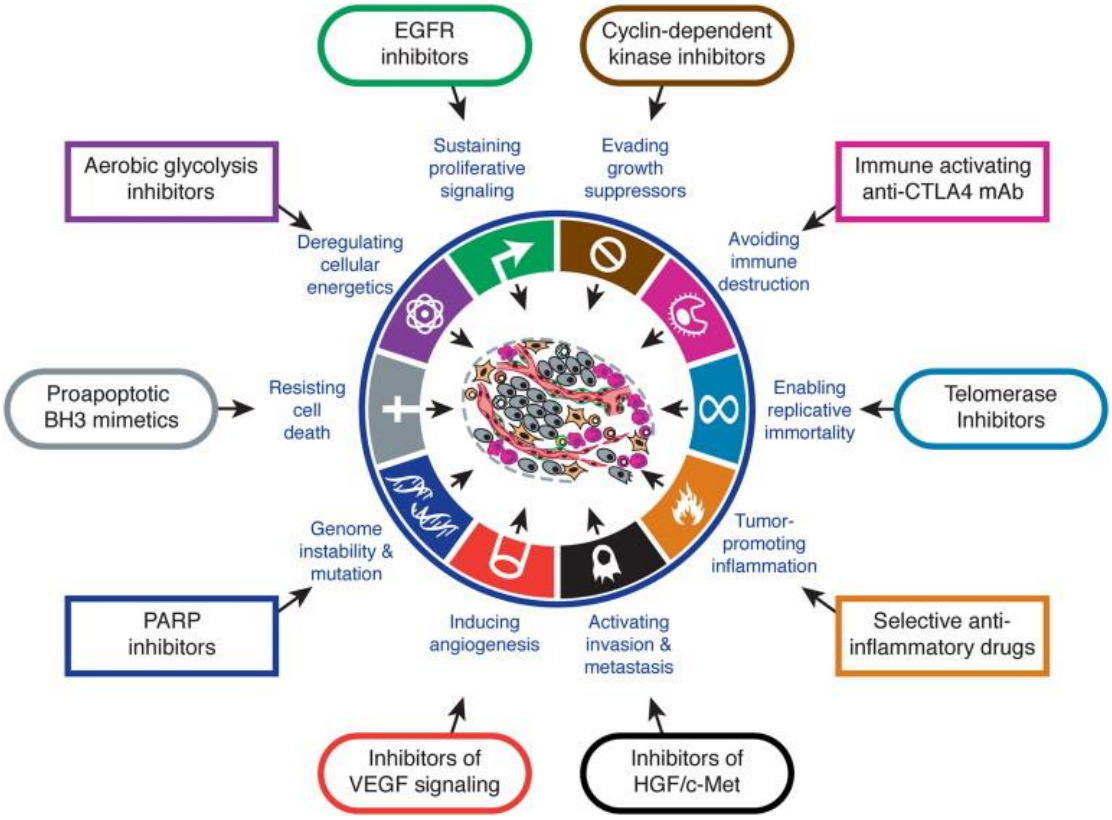

Figure 1.2. Characteristics of cancer cells and normal cells. (Adapted from [8])

This makes cancer cells produce energy at much higher rates than normal cells and enable them for extremely rapid growth. Besides, cancer cells secrete less cell surface adhesion molecules that they are less adhesive. Also, cancer cells could secrete proteases and growth factors that allowing cancer cells to digest extracellular

matrix components and promote angiogenesis. All these properties make tumor cells unrestrained by interactions between cells and matrix, and prone to invade and metastasize(Figure 1.3)[8-10].

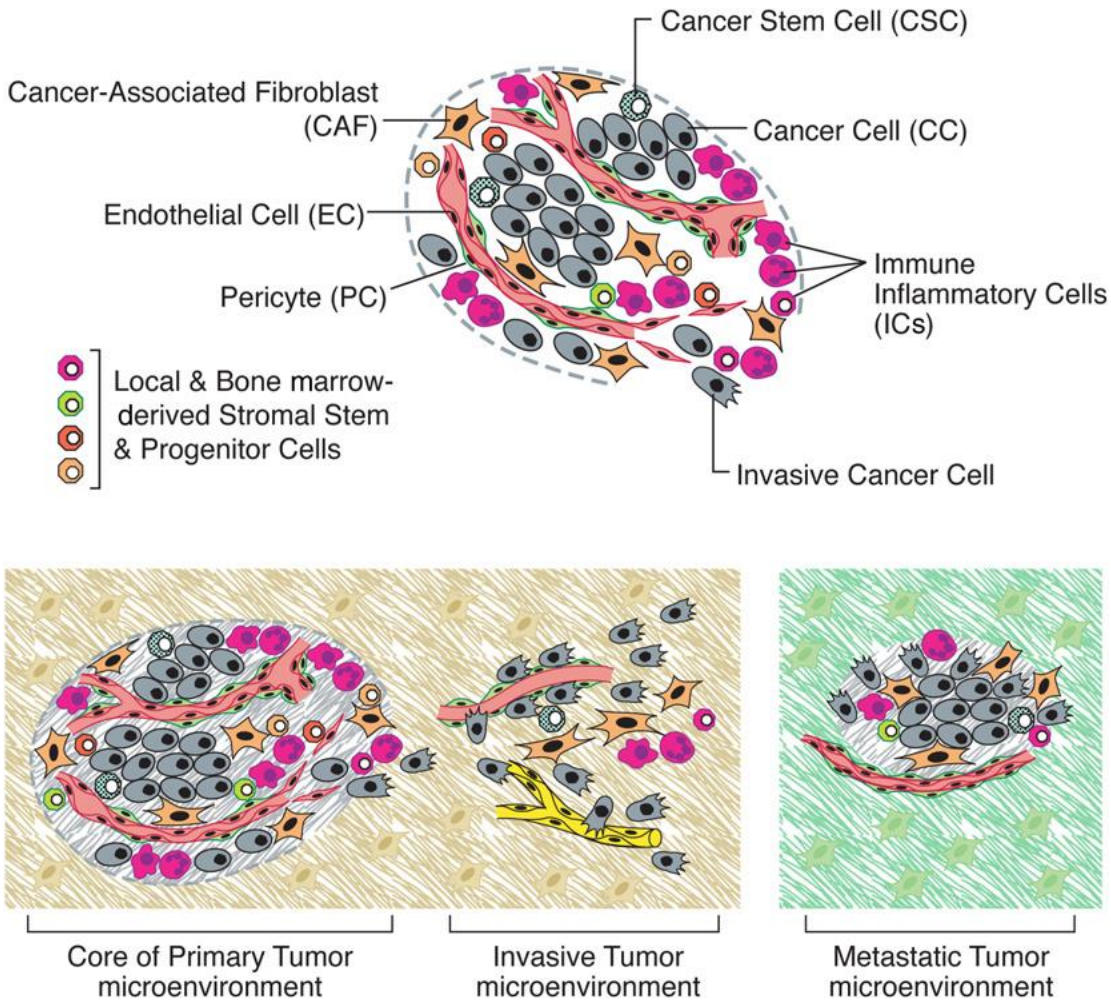

Figure 1.3 Process of tumor growth and metastasis. (Adapted from [8])

In the first step of tumor initiation, genetic alteration is thought to be the cause of abnormal cellular proliferation and tumors stayed at the level called dormant nodules. As tumor progression continues, angiogenesis occurs to enable exponential tumor growth. Different from normal vessels, vessels in tumors are usually tortuous and leaky which makes a vascular network in the tumor becomes more complex. The formation

of new blood vessels continues as tumor grows to provide tumors with essential nutrients and oxygen. At the same time, cancer cells began to show phenotypic changes to escape immune surveillance, such as the activation of epithelial-mesenchymal transition (EMT)[11, 12]. Cancer cells begin to lose cell-cell contact and being able to move and attain local invasion. At the last stage, cancer cells will undergo intravasation and extravasation and finally form metastasis and begin to survival in new location. Thus, cancer is the systemic disorder that involved in many tissues, organs, and even the whole organism, but not only uncontrolled proliferation of individual cells. Currently, more than a hundred types of cancer were found and they differ significantly in their behavior and show different response to various treatment, thus, it is impossible for a single treatment to cure cancer like other infectious diseases. Besides, the complexity of cancer progression and metastasis make cancer so complicated and hard to be cured[13-15].

1.2 Introduction of traditional cancer therapies

The search for cancer treatment over the past 100 years has uncovered several major therapies such as surgery, chemotherapy, and radiotherapy. These conventional therapies are advances in clinical application due to their reliability and effectiveness in killing cancer cells. Still, the severe side effects that may be brought by these therapies limited their efficacy. Surgery works best for local solid tumors that have not undergo metastasis. Surgery could remove the entire tumor or debulk a tumor helping

to ease some symptoms such as pain or pressure caused by tumors. Still, some common problems usually occur after the surgery such as the unbearable pain that patients often feel on the operated part as well as infection, bleeding and unavoidable damage to neighbor tissues, all these problems increase the risk of the surgery[7, 16-19].

Radiotherapy uses high doses of radiation to treat tumors and ease patients' symptoms. Radiation could damage cellular DNA and cancer cells under necrosis or apoptosis days after radiation. Radiation therapy is a good way to slow down the growth rate of cancer, preventing cancer from coming back. In most circumstances, radiotherapy is used in combination with other therapies to improve the treatment efficacy. The limitation of radiotherapy is that radiation could not only kill cancer cells but also damage surrounding healthy cells and the side effects could show up immediately after the treatment or months or years after radiation therapy. Besides, there is an upper limit of the amount of radiation that a human body can safely receive during the whole lifetime. The higher dose of radiation will damage the adjacent normal tissues and lead to severe side effects such as skin erythema, dry and moist desquamation of the skin [20].

Drugs used in chemotherapy could especially stop or slow the rapid growth of cancer cells. Chemotherapy often used as adjuvant treatment after treatment with surgery or radiotherapy. However, chemotherapy could also inhibit the growth of healthy cells which grow and divide rapidly. Immunotherapy is a relatively new kind of adjuvant cancer therapy that has already been approved to treat many types of cancer.

Some immunotherapies are trying to boost or stimulate the immune system to fight against cancer cells. Some are trying to make cancer cells easier to be detected and destroyed. Immunotherapy could also cause some side effects to the patients such as skin reaction and flu-like symptoms. Severe side effects such as nausea, hair loss, and tiredness are usually encountered by patient treated by chemotherapy [21]. Bad reaction to chemotherapy usually forced part of patients to stop the treatment session few times before completion[22]. Interrupted treatment could then compromise the effect of the treatment and may lead to tumor recurrence[23].

Although all these mentioned options have provided significant benefits to slow down the progression of cancer or to relieve the severe symptom of patients, new therapeutic methods with high efficiency and little side-effects are still urgently required against cancer. Besides, cancer is no longer viewed as a group of cells with genetic alterations that lose control of cell cycle. People are considering cancer as heterogeneous tissues which consist of both tumor cells and the surrounding microenvironment (TME) including extracellular matrix (ECM), cytokines, as well as various immune cells. Tumor physiological TEM interactions between cancer cells and affect tumor metabolism, aggressiveness and the response to treatment(Figure 1.4)[24]. Thus, the development of precise theranostic system is particularly critical for early detection and therapy for disease as complex as cancer.

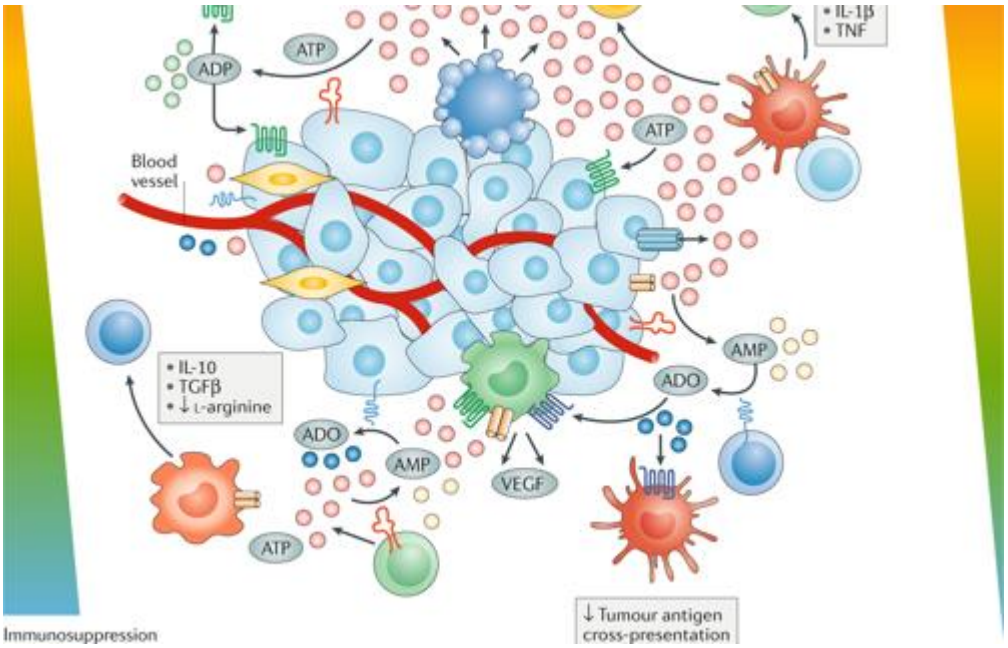

Figure 1.4 Tumor microenvironment. (Adapted from [24])

1.3 Photodynamic therapy

Photodynamic therapy (PDT), has emerged as a successful clinical therapeutic modality for cancer treatment which has already been approved by the Food and Drug Administration (FDA) [25, 26]. PDT relies on the synergistic interaction between photosensitizers, oxygen and the corresponding light. These elements are individually non-toxic, but they could initiate chemical reactions and achieve tumor cell apoptosis when working together. Photosensitizers could selectively enter the tumor site through blood circulation and give rise to large quantity of reactive oxygen species (ROS) when excited by the appropriate activating wavelength of light. ROS, especially singlet oxygen radicals, is believed to be responsible for the necrosis and apoptosis of cancer cells. Besides producing ROS to directly kill cancer cells, PDT could also cause immunoreaction against the cancer cells after treatment as well as inhibit tumor growth

by cutting off the nutrition supply through cancer-associated vasculature damage [27]. Due to the advantages of well-recognized safety, selectivity and repeatability, PDT has been applied not only in the field of dermatology but also used as adjuvant therapy to treat superficial tumors.

The process of photophysical and photochemical change of photosensitizers is the key part of the whole PDT. As shown in Figure 1.5, the ground state PS has two electrons in the orbital of low energy and one of the electrons can be boosted into a higher energy orbital and form a short-lived species after the absorption of light. Part of the excited singlet state PS could lose its energy by emitting light and undergo intersystem crossing to form excited triplet-state. Triplet PS can react with lipid or protein to produce reactive oxygen species or singlet oxygen. In this process, the production of ROS (free radical and singlet oxygen) can induce different biological activities, such as DNA fragmentation, chromatin condensation, and cytoskeletal shrinkage, leading to cell apoptosis[16, 28, 29].

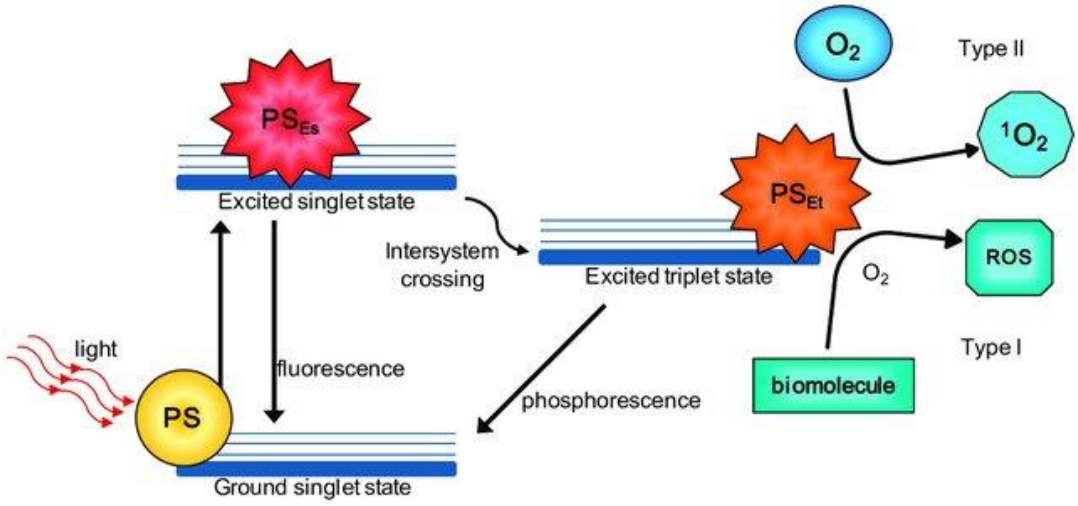

Figure 1.5 Activation of photosensitizers during PDT. (Adapted from [29])

The choose of photosensitizers and the corresponding light is also critical for the efficacy of PDT. Class photosensitizers such as porphyrin have tetrapyrrole structures. Taking the classic photosensitizer PpIX as an example, PpIX has a strong absorption peak between 405 and 415 nm and another smaller absorption peak from 500 to 640 nm. Due to the relatively short wavelength, the penetration depth of blue light is about 2 mm and higher fluence of red light (635 nm) is needed when applied for thicker lesions[16, 30].

Compared with conventional cancer therapies, PDT possesses several advantages. Firstly, photosensitizers could accumulate especially in the tumor site after blood circulation and the location of illumination is limited to the tumor tissue area so that the adjacent tissue will not be affected. Besides, only corresponding wavelengths of light source could activate photosensitizers and the remaining photosensitizers in the human body remain non-active and low toxicity. Light can be focused on a small point and produce the cytotoxicity at that specific point as well. Briefly, the activation of photosensitizers depends on the activation of light and this enables PDT to be conducted in control both spatially and temporally. The excessive ROS produced in the process could damage a wide range of cells in the tumor site and at the same time minimize systematic toxicity. Thus, PDT is regarded as a dual-specificity cancer treatment since PDT offers special local attacks instead of systematic attacks [31] [32].

The non-invasive way of PDT could also reduce the pain as well as the chance of infection for patients. Meanwhile, slight trauma occurs during PDT and no initiating

resistance exists for repeated treatments. All these properties make PDT a good choice for independent cancer treatment or as an auxiliary therapeutic modality. Currently, PDT has already become one of the best choices for skin cancer treatments[33, 34].

However, some limitations still need to be conquered for further improvement of PDT efficacy. Firstly, the application of PDT is limited to superficial tumors due to a limited light penetration depths of laser. Also, the poor accumulation efficacy of photosensitizers may limit the therapeutic efficiency of PDT. Besides, undesired skin photosensitization could be caused when patients were exposed to white light even for a few weeks following the treatment. In addition, PDT is an oxygen-consuming process that the existence of hypoxia in tumor site could compromise the efficacy significantly. To date, combining with nanotechnology, various types of photosensitizers have been developed trying to overcome these limitations.

1.4 Sonodynamic therapy

Sonodynamic therapy (SDT), has emerged as a promising non-invasive therapeutic modality compared to those traditional cancer therapies in the enduring battle against cancer [35]. SDT is a kind of ultrasound therapy in which sonosensitizers are administered to increase the efficacy of ultrasound's cytotoxicity to tumors while leaving normal tissue undamaged and intact. The concept of SDT is very similar to the well-established photodynamic therapy (PDT) which laser is used to activate photosensitizers to produce toxicity. Compared to PDT whose application is limited to

superficial tumors due to the limited penetration of laser light, SDT has the advantage of being able to treat deep-seated cancer since ultrasound can be focused on a single point deep within tissues in three dimensions. The effects of SDT on cancer treatment has been demonstrated widely. Although the generation of reactive oxygen species (ROS) in the presence of acoustic fields is believed to be responsible for SDT cytotoxicity, the mechanism for ROS production in SDT is less clear. The occurrence of inertial cavitation, which includes process of nucleation, growth and the implosive collapse of gas-filled bubbles in the solution upon the irradiation of ultrasound is an important process in SDT. Based on the cavitation phenomenon, sonoluminescence happened in which light is generated from inertial cavitation events and excite the nearby sonosensitizer to generate ROS [16, 18, 30, 36].

Sonodynamic therapy (SDT), has emerged as a promising alternative therapeutic modality compared to those traditional cancer treatment modalities in the enduring battle against cancer. SDT is a kind of ultrasound therapy in which sonosensitizers are administered to increase the efficacy of ultrasound's cytotoxicity to tumors while leaving normal tissue undamaged and intact. The US, as a kind of mechanical waves, transfer energy from one position to another in a form of molecular vibrations. Their physical properties have made them been extensively used in medicine for diagnostic and therapeutic applications. Diagnostic imaging US are used in ultrasound imaging and Doppler imaging while the therapeutic US is used widely in lithotripsy, thrombolysis, bone healing, peripheral nerve blocking and tissue ablation due to their

thermal and/or mechanical effects on the tissue[37, 38].

The concept of SDT is very similar to the well- established PDT which laser is used to activate photosensitizers to produce toxicity. Compared to PDT whose application is limited to superficial tumors due to the limited penetration of laser light, SDT has the advantage of being able to treat deep-seated cancer since ultrasound can be focused on a single point deep within tissues in three dimensions. The effects of SDT on cancer treatment has been demonstrated widely. The generation of reactive oxygen species (ROS) in the presence of acoustic fields is responsible for SDT toxicity, however, detail process about ROS generation is unclear. Cavitation induced by ultrasound is believed to be involved in the interaction of ultrasound and sensitizers to generate ROS (Figure 1.6)[37-39].

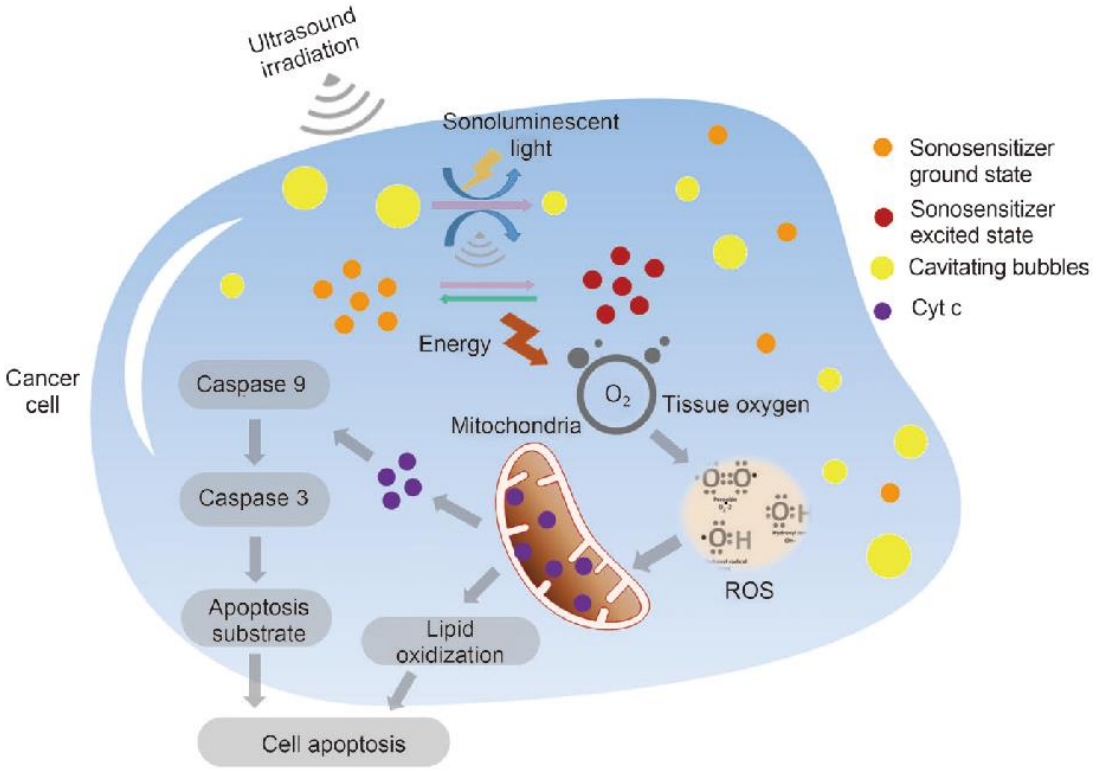

Figure 1.6 Mechanism of sonodynamic therapy. (Adapted from [39])

Cavitation is the behavior of gas bubbles in aqueous environments with the interaction of ultrasound. Cavitation includes the process of nucleation, growth and the implosive collapse of gas-filled bubbles and it can be divided into stable cavitation and inertial cavitation. While microbubbles rapidly expand and violently collapse in a liquid medium during inertial cavitation, the microbubbles do not violently collapse during stable cavitation. Light is generated in the solution upon the irradiation of ultrasound based on inertial cavitation. Despite this unconfirmed mechanism, microbubbles have been used to serve as artificial nuclei for enhanced ultrasound triggered cavitation in SDT[39-41].

1.5 Theranostic ultrasound and contrast agents

Ultrasound imaging, the most commonly used non-invasive imaging modality in clinics, has the advantages of lack of ionizing radiation, outstanding safety profile, good Spatio-temporal resolution, deep penetration compared to other modalities (MRI, PET, and optical). The development of targeted ultrasound contrast agents (UCAs) enables ultrasonic molecular imaging and extends the diagnostic capability and utility of this traditional imaging mode[42-44].

Commercial UCAs are usually gas-filled microbubbles with a modified surface such as ligands which can target cells specifically, thereby significantly increasing the sensitivity and specificity of ultrasound imaging and therapy. Although the huge potential of targeted microbubbles in ultrasound molecular imaging and therapy, their

relatively large size makes them unable to extravasate the vessels and thus limited their application inside vessels. However, the emergence of nanobubbles could overcome this limitation. Their nano-size enables them to extravasate the leaky vasculature of tumor and accumulate in the tumor site. Besides, similar to microbubbles, the ability of nanobubbles to carry either targeting moieties, imaging agents, or drug payloads makes them theranostic multifunctional particles. Despite the huge potential of nanobubbles for ultrasonic molecular imaging as well as nanocarrier for gas and drug delivery for tumor therapy, stabilization is still a big limitation of nanobubbles that could affect their function[45, 46].

1.6 Gas vesicles

Gas vesicles (GVs) are gas filled nanostructures which derived from cyanobacteria. The function of gas vesicles is to provide buoyancy to cyanobacteria making them able towards oxygen-rich layers to prevent oxygen or light limitation in special water bodies. Different species of cyanobacteria have different kinds of gas vesicles with a wide range of sizes and shapes. Isolated from *Anabaena flos-aquae*, GVs used in this passage typically showed a cylindrical morphology closed by a hollow conical cap at each end with length of 500nm, width of 75nm and wall thickness of 2nm. The wall of GVs is a bilayer protein structure with the outer layer of GVs hydrophilic while the inner layer of GVs hydrophobic to exclude water out of the 4.6 nm intervals. Thus, gases can flow in and out of the wall through the interval freely. As a result, no pressure gradient exists

for gas vesicles, making them inherently stable nanostructures[47-50].

Gas vesicles are mainly made by two types of proteins, GvpA and GvpC. GvpA which is a small hydrophobic protein, assembles the main backbone of GVs. GvpC is a relatively larger hydrophilic protein that strengthens the GV shell by binding across GvpA. GVs exclude water but permit gases to diffuse in and out of the shell freely. Thus, there is no pressure gradient between the interior GVs and the surrounding brine, making GVs inherent stable structure despite their nanometer size[47-50]. An in-depth study on genes involved in GVs production and regulation has been performed in Ana GVs. Besides various surface modifications that could confer extra properties to GVs. Thus, GVs establish a good biomolecular platform for further applications. Nowadays, the development of new application of GVs has attracted more and more attention. The ability of GVs to produce ultrasound contrast in purified form was found by *Shapiro et al* in 2014, establishing GVs as the first acoustic biomolecules. Besides their ability as ultrasound contrast agents, GVs could also function as contrast agents for magnetic resonance imaging. [30, 47-51].

CHAPTER 2 Surface-modified GVs as nanosized contrast agents for molecular ultrasound imaging of tumor

2.1 Background

The emergence of molecular imaging for cancer diagnosis and monitoring is considered a major milestone in the field of medical imaging[52]. Molecular imaging allows the noninvasive and continuous monitoring of tumors at the cellular and molecular levels[53-55]. Ultrasound imaging, the most commonly-used non-invasive imaging modality in clinics, has the advantages of low cost, wide availability, outstanding safety profile, lack of ionizing radiation, high spatio-temporal resolution, and portability[56-58]. The development of targeted ultrasound contrast agents (UCAs) enables ultrasonic molecular imaging and extends the diagnostic capability and utility of this traditional imaging mode[59]. Commercial UCAs are usually gas-filled microbubbles, surface-modified with ligands that can target cells specifically, thereby significantly increasing the sensitivity and specificity of ultrasound imaging[60]. Since microbubbles are several micrometers (1–8 μm) in diameter, they remain exclusively within the vascular compartment and this property makes them particularly well-suited for intravascular imaging of inflammation, angiogenesis, thrombi etc.[61]. Although the utilization of microbubbles for ultrasound imaging has shown encouraging results, their potential utility in biomedicine has been constrained by their inability to pass

through vessel walls into non-vascular tumor sites[52, 59, 62].

Nanobubbles, due to their nanoscale size, have greater potential in extravascular molecular applications such as tumor imaging. It is well-established that tumor vasculature exhibits enhanced permeability and retention (EPR) effects and nano-sized particles could efficiently cross the leaky, defective vasculature of tumors, leading to high extravasation and retention of nanoparticles in the tumor site[63]. Recently, targeted and non-targeted nanobubbles with various shells such as phospholipids or polymers have been developed for molecular ultrasonic imaging of tumors[45, 64]. Despite their potential benefits in tumor-targeted imaging, their configuration needs stabilization by the addition of surfactant on the shells as well as by the perfluorocarbon gas core[43, 44, 65, 66]. Gas escape, bubble fragmentation, and nanobubble collapse are phenomena that could occur after in *vivo* administration, negatively affecting their imaging performance.

Gas vesicles (GVs) are nanoscale gas-filled protein structures expressed intracellularly in certain cyanobacteria, which were recently reported as gene-encoded reporters offering significant potential as molecular ultrasound contrast agents[50, 51, 67, 68]. Unlike traditional UCAs, which trap preloaded gas in an unstable configuration, the 2 nm-thick protein shells of GVs exclude water but are freely permeable to gases in the surrounding media, making them physically stable despite their nanometer size[48, 51]. GVs were demonstrated to be able to produce robust ultrasound contrast across a range of frequencies at picomolar concentrations and exhibit harmonic scattering to

enable enhanced detection versus background *in vitro*[50, 51]. Moreover, strong non-linear contrast images of GVs could be acquired on the location of inferior vena cava (IVC) and liver after intravenous injection[51]. Their stable performance and robust ultrasound contrast make GVs good candidates as molecular contrast agents for tumor imaging. However, similar to other common nanoparticles, the majority of GVs after intravenous administration is usually taken up in non-targeted tissues, such as the liver, spleen, and lungs[69]. Foster *et al.* recently reported that the reticuloendothelial system (RES) cleared 84% of native GVs twenty minutes following administration to mice due to capture by phagocytic cells and collapsed GVs through the biliary system, with almost no GVs remaining in the blood 120 minutes after injection[69]. Such rapid clearance could limit the utility of GVs for tumor molecular imaging as they may not be able to circulate long enough to extravasate into tumor tissues.

Surface modifications can be made to GVs to resolve the systemic clearance issue by improving their pharmacokinetic properties. Multiple studies have reported that adding polyethylene glycol (PEG) on the surface of nanoparticles effectively reduced RES uptake and increased circulation time in the blood, leading to selective accumulation of the nanoparticles to the tumor site[70-73]. Likewise, hyaluronic acid (HA) on the surface of nanoparticles has displayed efficacy in targeting particles to CD44-positive malignant cancer cells and selectively enhancing the accumulation and retention of nanoparticles at the tumor site[74-78]. In the present study, PEG-conjugated-HA was conjugated to GVs and the PEGylated HA-GVs (PH-GVs) were

characterized. PH-GVs abd GVs were found to be stable in solution as well as when under ultrasound irradiation. PH-GVs were found to display enhanced targeting and immune escape abilities compared to unmodifed GVs and were not cytotoxic to cells. PH-GVs also showed greater tumor targeting and retention as well as longer duration of sustained signal *in vivo*, without obvious damage to vital organs. Thus, in all, we demonstrate PH-GVs as a potent novel nanoparticle for ultrasound molecular imaging *in vivo* with high biocompatibility and targeting ability.

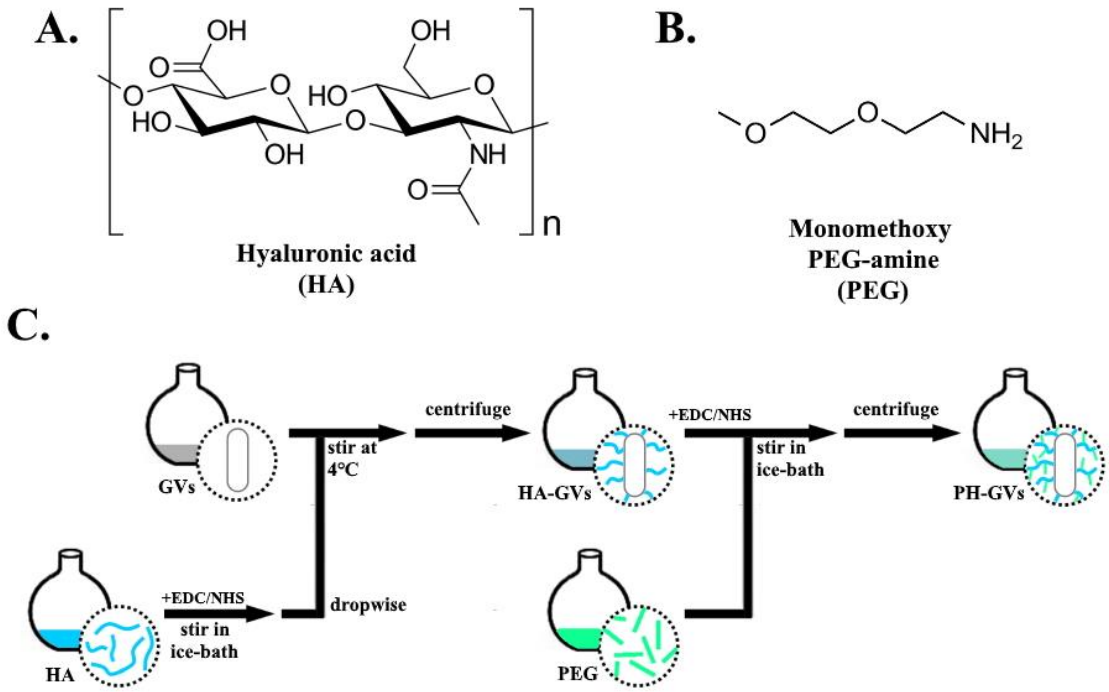

Figure 2.1 Schematic illustration of the preparation process of PEGylated HA-GVs (PH-GVs).

2.2 Materials and methods

2.2.1 Materials

Ethylenediamine (EDA), 1-ethyl-3(3-(dimethylamino)propyl) carbodiimide (EDC), and Nhydroxysuccinimide (NHS) were obtained from J&K company (Beijing, China). Propidium iodide (PI) was purchased from Sigma-Aldrich Co. (St. Louis, MO). ICG-Sulfo-Osu (ICG) was obtained from Dojindo molecular technologies (Tokyo, Japan). CCK-8 assay kit and 4,6-diamidino-2-phenylindole (DAPI) were purchased from Sangon Biotech (Shanghai, China). Calcein-AM was obtained by Invitrogen (Grand Island NY). FITC-conjugated goat anti-rabbit immunoglobulin G was from Life Technologies (NY, USA). Squamous cell carcinoma cell line (SCC7) were bought from ATCC (Manassas, VA). Methoxypolyethylene glycol amine (PEG-amine, molecular weight=5 kDa) was purchased from Shanghai Seebio Biotech (Shanghai, China). Sodium hyaluronic acid (HA, molecular weight= 234 kDa) was bought from Lifecore Biomedical (Chaska, MN).

2.2.2 Preparation of native GVs and PEGylated HA-GVs (PH-GVs)

Anabaena flos-aquae (FACHB-1255, Freshwater Algae Culture Collection, Wuhan, China) was cultured in sterile BG-11 medium at 25°C under fluorescent lighting on a 14h/10h light/dark cycle. GVs were isolated and purified through tonic cell lysis and centrifugally assisted floatation according to Walsby's method (Buckland

and Walsby 1971). Briefly, hypertonic lysis, achieved by quickly adding sucrose solution to a final concentration of 25%, was used to release GVs. GVs were isolated by centrifugation at 400g for 3 h after hypertonic lysis. The isolated GVs formed a white creamy layer on top of the solution and were collected by syringe. To purify the GVs, it was washed by the same centrifugation process three times and stored in phosphate-buffered saline (PBS) at 4°C. The concentration of GVs was estimated using a literature-based formula (450 nM per OD500) (Walsby 1994), where OD500 is the optical density at a 500-nm wavelength measured with a UV-visible spectrophotometer (2100 Pro, GE Healthcare, Piscataway, NJ, USA). Volume fraction was estimated using approximated gas volumes of 8.4 μL/mg and molar weight of 107 MDa as described elsewhere (Walsby and Armstrong 1979).

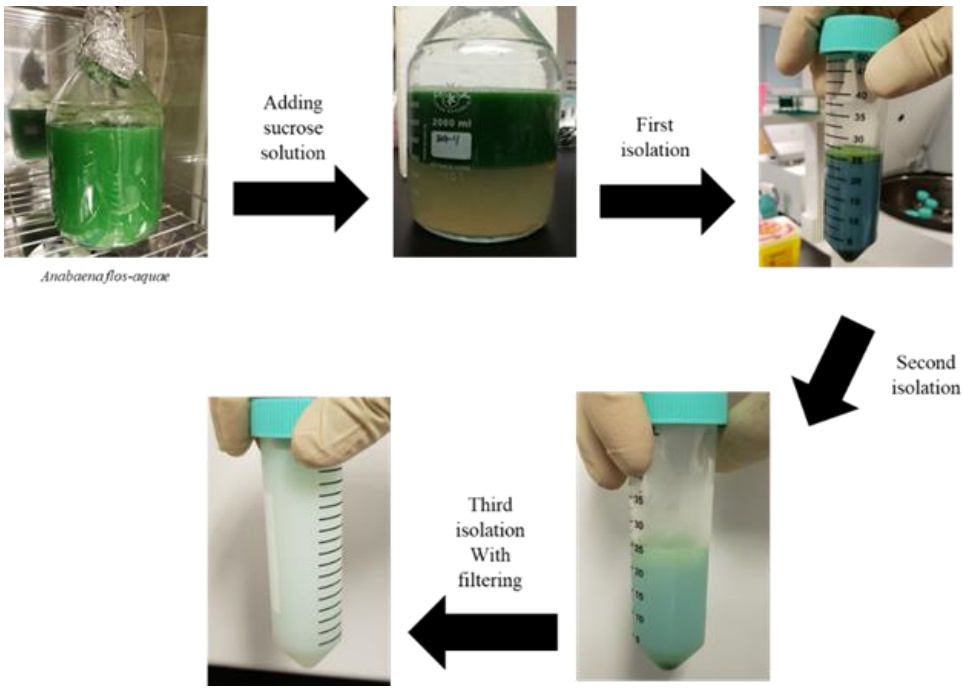

Figure 2.2 Flow chart of GV extraction

For PEGylated HA-GVs (PH-GVs) synthesis, PEG and HA were immobilized to the GVs' protein shells by covalent conjugation. Firstly, EDC (3.37 mg) and NHS (2 mg) were added to HA solution (10 mg) in PBS (pH = 7.4). The solution was then stirred in an ice-bath for 2 h. Then 1 mL of GVs (5 nM) dissolved in PBS (pH = 7.4) was added dropwise. The reaction mixture was stirred for another 24 h at 4°C. The resulting mixture was added into the ultrafiltration tube (2 mL) and centrifuged at 1800 rpm for 5min to remove free EDC, NHS, and HA. The resultant nanoparticles were stored in PBS buffer 4°C. PEG was chemically conjugated to the HA-GVs conjugate through amide formation in the presence of EDC and NHS. The HA-GVs conjugate was dissolved in PBS (pH = 7.4), which was mixed with EDC (3.37 mg) and NHS (2 mg) in PBS. After PEG-amine (73.5 mg) was slowly added, the mixture was stirred for 24 h in an ice-bath. The resulting solution was then centrifuged against the excess amount of EDC, NHS and PEG and washed 4 times with PBS.

The prepared GVs were also labeled with a NIR dye, ICG, for cellular experiments and animal imaging tests, as a first step before the addition of HA and PEG.[79, 80] Briefly, EDC and NHS were added to ICG solution in PBS (pH = 7.4). After 30 mins incubation at room temperature, the solution was added to pure GV solution (molar ratio: ICG/GV=1000/1). Then the mixture was shaken for 4 hours at 4°C and followed by purification 4 times by centrifugation. The resulting mixture was added into an ultrafiltration tube (50 mL) and centrifuged 1800 rpm for 5min to remove free ICG. The resultant nanoparticles were stored in PBS buffer.

2.2.3 Characterizations of GVs and PH-GVs

The particle size and size distribution of PH-GVs were measured by dynamic light scattering DLS (Varian, Palo Alto, USA). Zeta potential measurements were performed at 25 °C on a Malvern Zeta Size-Nano Z instrument. UV-vis absorbance spectra of GVs and PH-GVs were observed by Multiskan Go microplate reader (Thermo Fisher Scientific, Massachusetts, USA). Fluorescent signals of ICG and ICG labeled PH-GVs were measured using a fluorescence spectrophotometer (Varian, Palo Alto, USA). The morphology of GVs was imaged using transmission electron microscopy (TEM) (JEOL 2100 F, JEOL, Tokyo, Japan) operating at 200 kV. GVs in deionized water (0.5 nM) were deposited on a carbon-coated grid and dried at room temperature overnight. Hydrodynamic size was obtained using the dynamic light scattering (DLS) method.

2.2.4 Acoustic imaging of GVs and PH-GVs in vitro

PH-GVs and GVs were put into a dropper (5 mL) before imaging and all the droppers were immersed at the same depth in the deionized water. Ultrasound B-mode and Contrast mode images of GVs were acquired using Vevo 2100 imaging system (FUJIFILM VisualSonics, Toronto, ON, Canada, 21 MHz, B-mode) with a transducer of LZ250 D. The center frequency and output energy level were set to 18 MHz and 4 %, respectively.

2.2.5 Cell Internalization detection of GVs and PH-GVs

Squamous cell carcinoma cell line (SCC7 cells) and murine RAW 264.7 macrophage cells were seeded in an 8-well chamber in Dulbecco's Modified Eagle Medium (DMEM)/high glucose medium supplemented with 10% FBS and 1% antibiotic solution at 37 °C and 5% CO_2. The next day, both cells were washed by cold PBS and incubated with different kinds of GVs at 37 °C for 4 h with 5% CO_2 atmosphere. After incubation, all cells were washed thoroughly with cold PBS. The cells were finally fixed in cold ethanol for 15 min at -20 °C and mounting medium containing DAPI was added and incubated for 10 min in the dark. Cell internalization of ICG labeled PH-GV and ICG labeled GVs were observed by a confocal microscope (Olympus, USA) and the excitation and emission wavelengths were set at 780 nm and 800 nm for ICG, respectively.

2.2.6 Cytotoxicity detection of GVs and PH-GVs

The SCC7 cells were seeded in a 96-well plate at a density of 8000 cells per well and cultured overnight at 37 °C in a 5% CO_2 incubator. The next day, cells were washed with PBS for 3 times and incubated with GVs, collapsed GVs and PH-GVs at a series of concentrations for 24 h and 48 h under the same condition. Cell viability was evaluated by CCK-8 assay kit. The optical density (OD) was measured at 450 nm and recorded by a microplate reader.

2.2.7 Biodistribution of GVs and PH-GVs in nude mice

Animal experiments were conducted under protocols approved by the Animal Care and Use Committee (CC/ACUCC) of Hong Kong Polytechnic University. Subcutaneous sites of athymic nude mice (seven weeks old, female, 20-24 g) were injected a suspension of 4×10^6 SCC7 cells in PBS (80μL). When the tumor size (in the right leg region) reached average size of 120 mm^3, mice were randomly allocated into three groups, (a) Free ICG solution was injected into the tail vein of the mice. (b) ICG labeled GVs solution was injected into the tail vein of the mice. (c) ICG labeled PH-GVs solution was injected into the tail vein of the mice. Fluorescent imagines were acquired at 0, 0.5, 1, 2, 4, 8, 12, 24 and 48 h after injection using IVIS Lumina II (Caliper Life Sciences, USA; Excitation Filter: 780 nm, Emission Filter: 800 nm). At the time of highest accumulation after one-dose injection, tumors and normal organs (heart, liver, spleen, kidney, lung, and muscle) were collected and for acquisition of Fluorescent signal intensity.

2.2.8 In Vivo US imaging of SCC7 Tumor Xenografts in Nude Mice

US images in the tumor sites were recorded on the Vevo 2100 imaging system. When the tumor size (in the right leg region) reached average size of 120 mm^3, mice were randomly allocated into three groups, (a) PBS, (b) GVs and (c) PH-GVs. US imaged were acquired at 0, 0.5, 1, 2, 4, 8, 12, 24 and 48 h following tail injection. At the time of highest accumulation after one-dose injection, the high power of US

stimulation is performed, which can induce the collapse of GVs. The signal intensities of echo imaging were measured using Vevo 2100 Workstation Software.

2.2.9 Statistical analysis

Comparisons among groups were analyzed via independent-samples one-factor ANOVA test using SPASS 17.0 software. All statistical data were obtained using a two-tailed student's t-test and homogeneity of variance tests (p values <0.05 were considered significant).

2.3 Results and discussion

2.3.1 Characterization of native GVs and PEGylated HA-GVs (PH-GVs)

The PH-GVs used in this study were generated by sequential covalent conjugation of HA followed by PEG to native GVs harvested from *Anabaena flos-aquae* (Figure 2.1). The successful synthesis of PH-GVs was confirmed by transmission electron microscopy (TEM). Compared to native GVs which showed clean cylindrical morphology and clear ribs on the shell, PH-GVs were wrapped by a layer of substrate and the ribs on the shell were not easily visible (Figure 2.3a). Zeta potential of native GVs was between −40 ± 5 mV while PH-GVs showed a negative zeta potential of −20 ± 6 mv (Figure 2.3b). Zeta potential is a key indicator of nanoparticle stability, and the values obtained for both native GVs and PH-GVs indicated a suitable surface charge for colloidal stability[81]. Both GV groups showed nanoscale diameters (~400 nm for native GVs, ~500 nm for PH-GVs) with relatively uniform size distributions (Figures 2.3c).

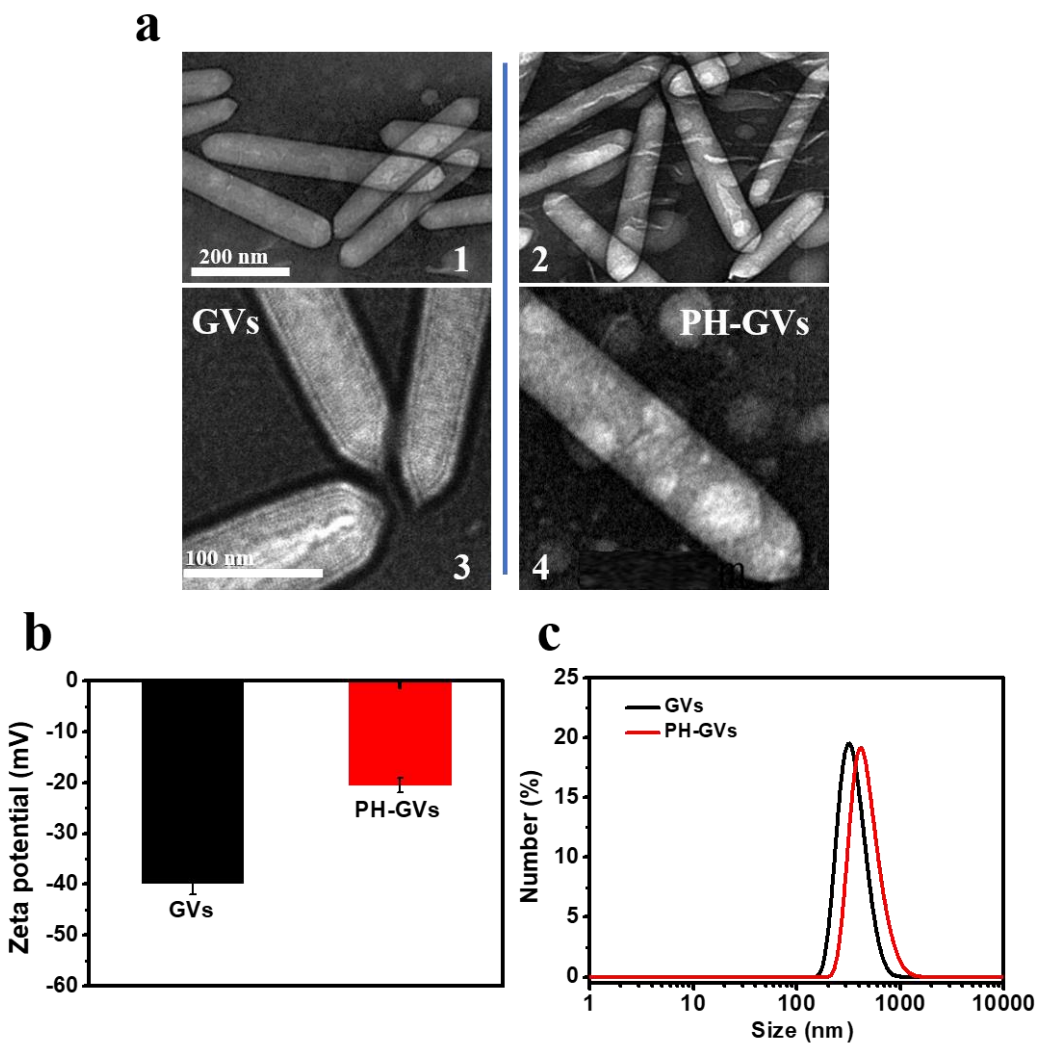

Figure 2.3 Characterization of GVs and PH-GVs. (a) The TEM image of GVs and PH-GVs. Due to the wrapping and folding of GVs by PH-HA, we can find the surface of the GVs have been packed with a heavy substance. Scale bar equals to 200 nm. (b) Zeta potentials and Dynamic light scattering analysis of GVs and PH-GVs in PBS at pH 7.4. Data in (b) and (c) represent the mean ± SD from on 3 independent experiments.

2.3.2 Ultrasound imaging property of PH-GVs

GVs and PH-GVs were next tested for their ultrasound contrast properties using a Vevo 2100 imaging system (FUJIFILM VisualSonics, B-mode) operating at 21 MHz, at different concentrations. Both native GVs and PH-GVs produced robust contrast

relative to buffer controls at concentrations ranging from 250 to 1000 pM, with gas volume fractions of approximately 0.01% to 0.1% (Figure 2.4a). Contrast in both GVs groups increased as the concentration of GVs was increased, with 1000 pM showing the highest contrast in both groups (Figure 2.4b). We also determined the biostability of the GV groups by incubating them in PBS or fetal bovine serum (FBS) and imaging them over the course of 7 days. Native and PH-GVs showed no reduction in echogenicity in either PBS or FBS, thereby demonstrating their physical stability in physiologically relevant conditions (Figure 2.4c-d). These results demonstrate that native and PH-GVs generated by us showed good contrast generation and stability in solution.

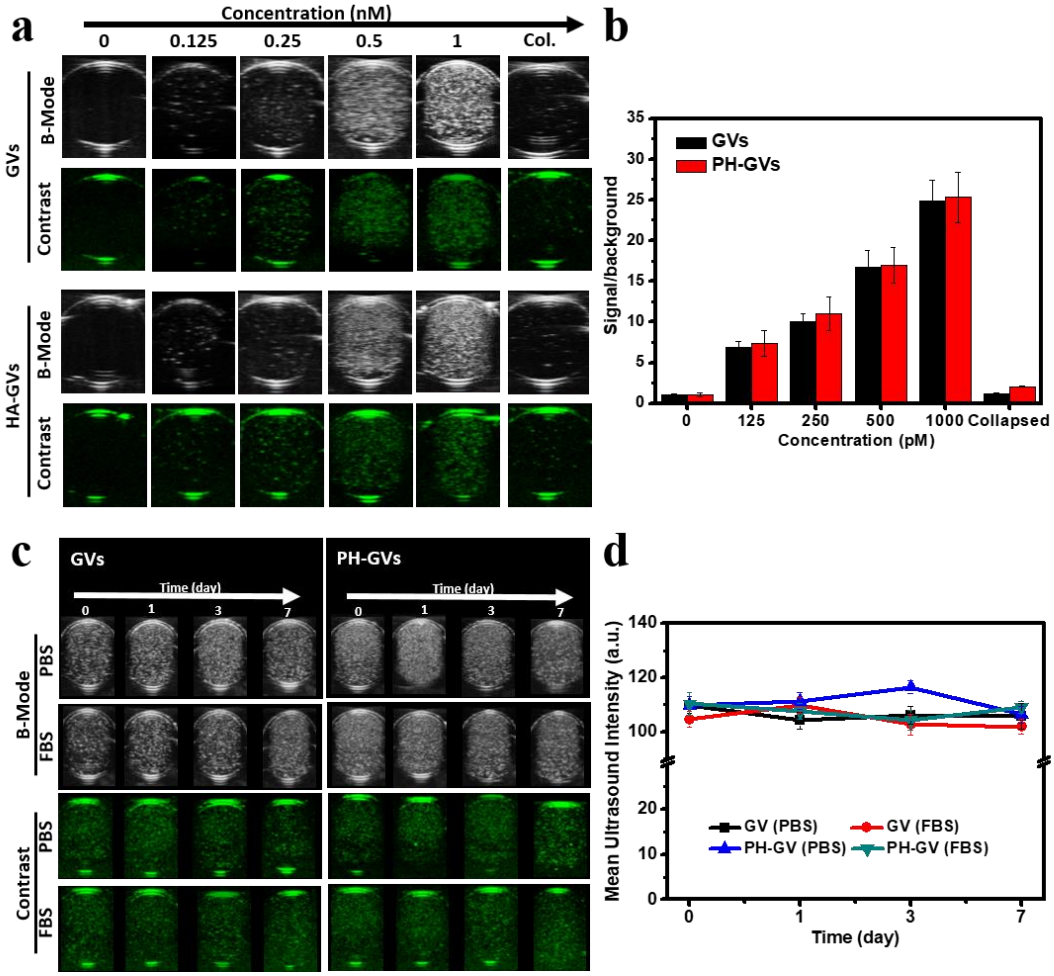

Figure 2.4 In vitro ultrasound image enhancement. (a) Ultrasound images of a dropper phantom containing PBS buffer, GVs, and PH-GVs at concentration ranging from 125 to 1000 pM. Images were acquired at B-mode and contrast mode, as indicated. (b) Total backscattered signal relative to PBS at each GVs concentration. Data represent the mean ± SD based on 4 independent experiments. (c) Ultrasound images of a dropper phantom containing GVs and PH-GVs (GVs concentrations of 500 pM) staying for various time. (d) Quantitative analysis of the images in (c). Data represent the mean ± SD from 4 independent experiments.

Besides, we tested the stability of PH-GVs under some physical or mechanical forces, such as temperature, ultrasonic. We conducted additional experiment to demonstrate the stability of GVs and PH-GVs under different conditions (25 °C, 37 °C, 45 °C) for different time durations, and examined the ultrasound contrast intensity. The echoed ultrasound signals were captured in B-mode images (Figures 2.5a) and quantitative intensity chart (Figure 2.5b) shown below. The results show that the ultrasound intensity of GVs and PH-GVs remained stable for up to 24 hours at all temperatures without obvious decreasing trend. In another experiment, B-mode images were acquired under ultrasound irradiation at imaging intensity level at different time points. The results in Figures 2.5c and 2.5d show no echo contrast decrease of both GVs and PH-GVs, indicating GVs and PH-GVs are stable enough under B-mode imaging intensity. GVs used in the study is *Ana* GVs, and the critical collapse pressure is 440–605 kPa[51]. When applying 650 kPa ultrasound sonication, both GVs and PH-GVs collapsed with immediate echo signal disappeared (Figure 2.5c-d). Both GVs and PH-GVs collapsed with 650 kPa insonation.

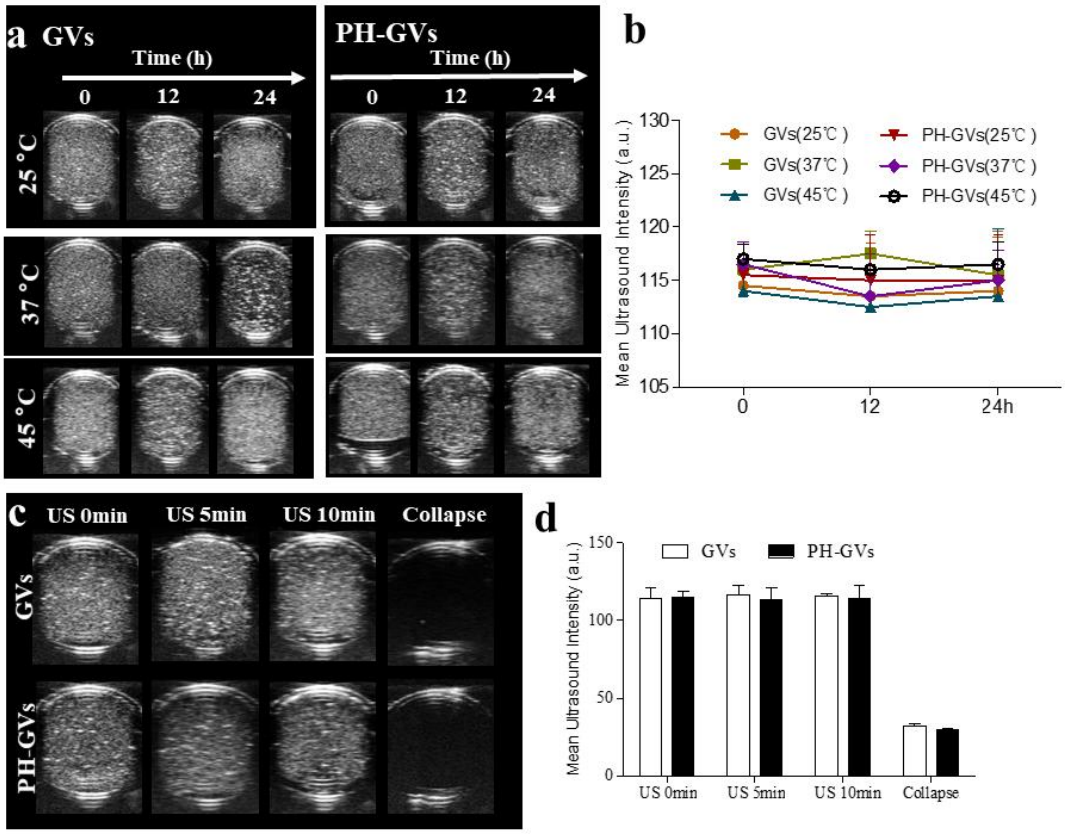

Figure 2.5 (a) Ultrasound B-mode images of a phantom containing GVs and PH-GVs (1nM) under different temperatures for different time durations. (b) Quantitative results of the B-mode image intensity. Data representing the mean ± SD from 4 independent experiments. (c) Ultrasound B-mode images of GVs and PH-GVs under B-mode ultrasound imaging intensity for different time durations. (d) Quantitative results of the B-mode image intensity. Data represent the mean ± SD from 3 independent experiments.

2.3.3 Targeting ability and immune escape ability of PH-GVs in vitro

To validate the active targeting efficiency of PH-GVs, we incubated our PH-GVs with the squamous cell carcinoma cell line (SCC7), known to have high expression of CD44. To monitor the location of our GVs, we labeled both groups of GVs with indocyanine green (ICG), a near infra-red (NIR) fluorophore (Figure 2.6a). ICG-linked

GVs showed a significant broadening of their absorption spectrum compared to free ICG, indicating their successful conjugation (Figure 2.6b). ICG-linked GVs also showed significantly higher fluorescence intensity at increasing concentrations, thereby confirming the successful linkage of the dye to the GVs (Figure S2.6c-d).

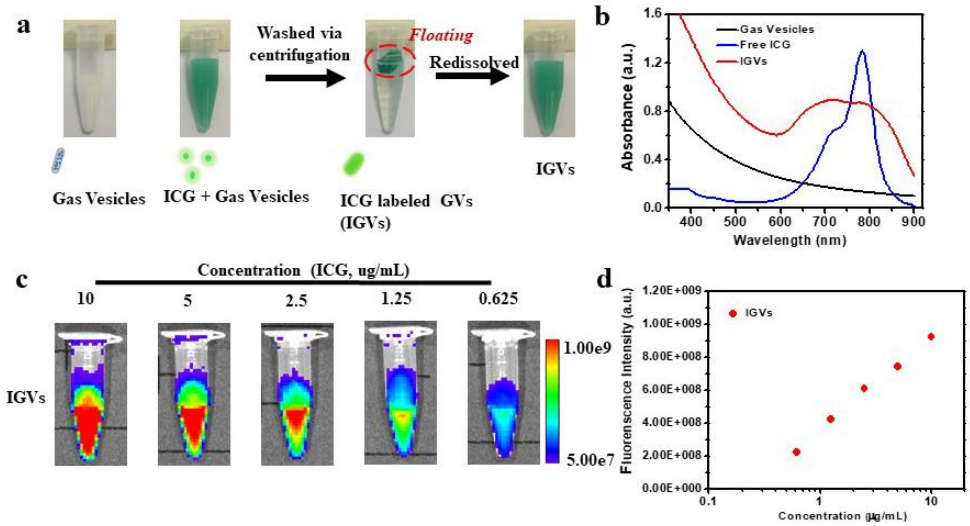

Figure 2.6 (a) The Synthesis of ICG-GV. (b) Absorbance spectra of Gas Vesicles, ICG, ICG-Gas Vesicles in phosphate buffered saline (PBS). (c) Fluorescence images of IGV at diverse concentrations. (d) Fluorescence signals intensity of IGV at diverse concentrations. (Ex. 780 nm, Em. 845 nm).

The interaction of ICG labeled native GVs and PH-GVs with CD44-positive cells was then evaluated using fluorescence imaging. ICG-PH-GVs showed a significantly greater ability to accumulate in the cytoplasm of SCC7 cells than the ICG-GVs after 6 hours incubation (Figure 2.7a) indicating more successful cellular uptake of the PH-GVs. We also tested the GV groups' immune escape abilities *in vitro* by incubating them with the murine macrophage cell line RAW 264.7. Native GVs showed a strong red fluorescence within these immune cells, while PH-GVs showed little-to-no signal

(Figure 2.7b) indicating enhanced immune escape of the PH-GVs. PEGylation of HA-GVs was thus seen to confer greater homotypic targeting and reduced internalization by immune cells with greater potential for effectiveness *in vivo*.

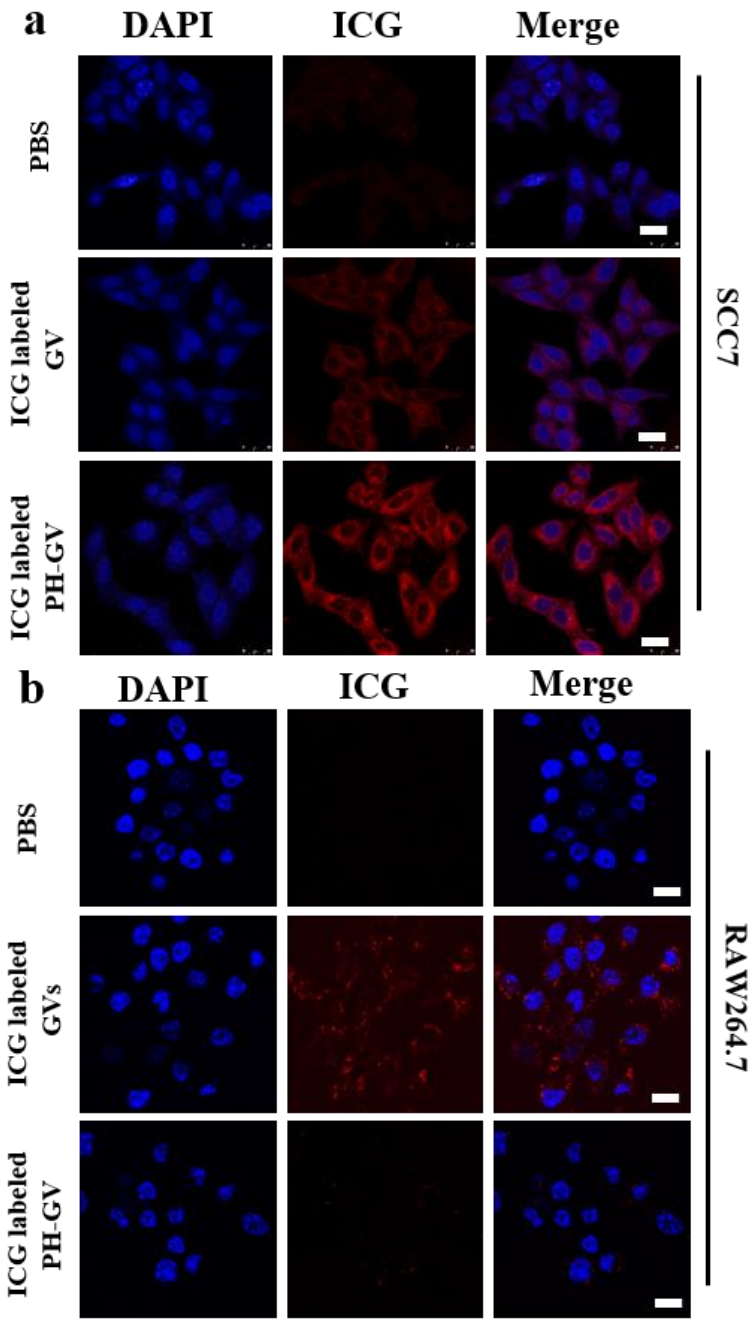

Figure 2.7 Targeting ability and immune escape abilities of PH-GVs. Confocal microscopy images of ICG labeled GVs and ICG labeled PH-GV co-incubated with SCC-7 cells for 6 hours.

Scale bars represent 20 μm. Representative images are shown in (a). Cellular uptake of PH-GVs by murine RAW 264.7 macrophage cells were observed under a fluorescence Microscope. Representative images are shown in (b). Scale bars represent 20 μm.

2.3.4 Biodistribution and tumor accumulation of PH-GVs in vivo.

Next, we determined the *in vivo* biodistribution and tumor-targeting characteristics of PH-GVs. Tumor-bearing mice were monitored for 48 hours by real-time NIRF imaging after systemic administration of free ICG (200μl, 20μg), ICG-labeled GVs (20 nM, containing 20μg ICG), ICG-labeled HA-GVs (20 nM, containing 20μg ICG) and ICG-labeled PH-GVs (20 nM, containing 20μg ICG) respectively. Free ICG and ICG-labelled GVs initially showed significant fluorescence in the vital organs (liver, lungs, spleen, etc.), but decreased over time without showing localization in the tumor site (Figure 2.8a). In ICG-labeled HA-GVs group, strong signals around the whole body of the mice were detected at the early time points. By contrast, ICG-labelled PH-GVs showed consistent but moderate signals in the vital organs of mice at the shortly post-injection but showed the strongest localization to the tumor site from 8 hours onwards. 6 hours post-administration, ICG-labelled PH-GVs showed a Tumor/Muscle ratio above 2 and was maintained for almost all of the remaining duration, which is always higher than that of ICG-labelled HA-GVs group (Figure 2.8b). This ratio did not significantly increase in Free ICG and GVs groups at any point. Closer examination of the large organs and the tumor showed that ICG-labelled PH-GVs group showed high fluorescence in the tumor at 12, 24 and 48 hours but not in the

other vital organs, whereas ICG-labelled GVs localized highly in the liver, but not in the tumor at any observed time point (Figure 2.8c). The fluorescence intensity of tumor in ICG-labelled PH-GVs group remained high over the 48 hours period examined, whereas fluorescence of tumor decreased in ICG-labelled GVs group and ICG-labelled HA-GVs group over time indicating tumor excretion gradually (Figure 2.8d-f). The ability of PH-GVs to primarily label the tumor site after 6 hours and the sustained signal over 48 hours confirmed the PH-modification's improvement to the ability of the PH-GVs to escape immune clearance, their stability, and their tumor-targeting potential.

To further confirm the enhanced retention of ICG-labelled PH-GVs in tumor-bearing mice, we finally investigated the interstitial penetration of ICG-labelled GVs and ICG-labelled PH-GVs inside solid tumors after 12 hours post-injection. The tumors were extracted and tumor slices were stained with DAPI (blue) and anti-CD31 antibody (red) for confocal imaging to label the relative location of cell nuclei and blood vessels. ICG-labeled GVs showed no fluorescence (green) in the tumor sections, whereas strong ICG fluorescence was visible in the tumors of the ICG-labelled PH-GV group (Figure 2.8g). Crucially, the green fluorescence observed was not restricted to colocalization with CD31 (vessels) but could also be seen in the region around the nuclei. This indicates the successful passing of the PH-GVs past the tumor vasculature, through the EPR effect, and successful cellular uptake by tumor cells. Combined with the evidence detailed in previous figures, these results demonstrate that the PH-encapsulation of GV surfaces enabled reduced clearance, enhanced blood circulation time and increased

tumor penetration through blood vessels, enabling their enhanced *in vivo* performance.

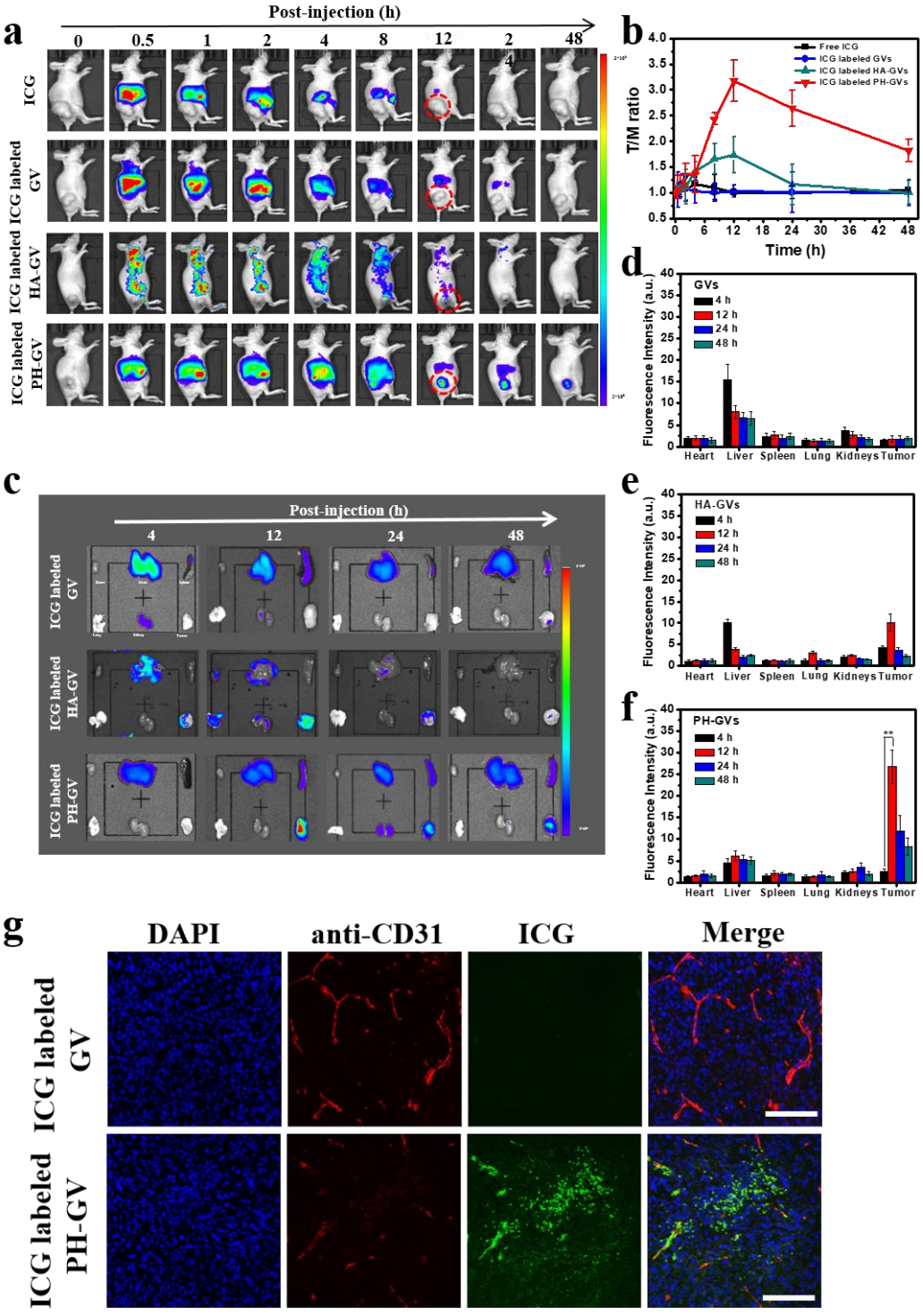

Figure 2.8 *In vivo* biodistribution of PH-GVs. (a) *In vivo* NIR fluorescent imaging of tumor-bearing mice was taken at different times after intravenous injection of free ICG, ICG labeled GVs,

ICG labeled HA-GVs and ICG labeled PH-GVs, respectively. Red circles indicate the tumor's location. (b) Tumor/muscle (T/M) ratio of tumor-bearing mouse model at different times. Data represent the mean ± SD from 5 independent experiments. (c) *Ex vivo* fluorescence imaging of vital organs and tumors taken from tumor-bearing nude mice after 4, 12, 24 and 48 h post-injection of ICG-labeled GVs, ICG labeled HA-GVs and ICG-labeled PH-GVs, respectively. Quantitative analysis for the accumulation in tumor and vital organs of ICG labeled GVs, ICG labeled HA-GVs and ICG labeled PH-GVs are shown in (d), (e) and (f). Data represent the mean ± SD (n = 5). *$p < 0.05$ vs. control. **$p < 0.01$ vs. control. *In vivo* biodistribution of PH-GVs. (g) Confocal images of tumor slices collected from mice 12h post-injection of ICG-labeled GVs and ICG-labeled PH-GVs. The green and red signals were from the fluorescence of ICG and anti-CD31-stained blood vessels, respectively.

2.3.5 In vivo cancer US imaging by PH-GVs.

We next tested the GVs groups' relative abilities to generate US contrast *in vivo* by intravenously injecting GVs, HA-GVs or PH-GVs into SCC7 tumor-bearing mice. 200 μl GVs, HA-GVs and PH-GVs (20 nM) were respectively administered into the tail vein of tumor-bearing nude mice and nonlinear ultrasound images (transmitting at 18 MHz) of the tumor site were acquired using the Vevo 2100 imaging system. Ultrasound images showing tumor sites at 0, 0.5, 1, 2, 4, 8, 12, 24, and 48 hours post-injection showed that PH-GVs showed much greater and well-sustained ultrasound contrast inside the tumor (green signal) compared to native GVs and HA-GVs (Figure 2.9a). Imaging with PH-GVs exceeded the ultrasound intensity generated by GVs and HA-GVs at 6 hours, peaked at 12 hours, gradually diminishing over the remaining period, whereas HA-GVs showed lower ultrasound signals and native GVs showed an

almost flat time profile (Figure 2.9b). To confirm that PH-GVs were the source of the observed contrast, we applied 650 kPa US pulses, which resulted in the disappearance of the contrast (Figure 2.9c). Regions of interest containing GVs exhibited 60 ± 14% stronger backscattered signals than buffer-injected controls ($p = 0.008$), with the difference disappearing after collapse ($p = 0.23$) (Figure 2.9d).

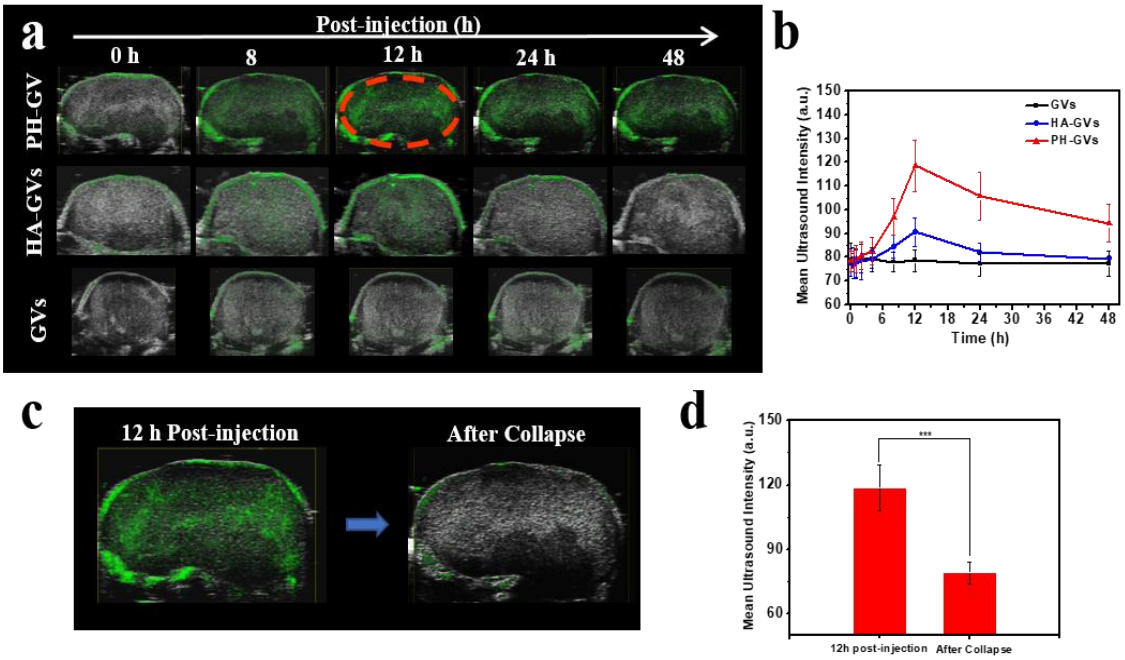

Figure 2.9 Ultrasound imaging of PH-GVs in tumor sites. *In vivo* ultrasound images of tumor after intravenous injection of GVs, HA-GVs and PH-GVs were captured. Representative images are shown in (a) with quantification of intensity shown in (b). The green color represents the intensity-enhanced region due to the GVs.(c) Vesicle collapse with destructive insonation (650 kPa). Representative images are shown in (c) with quantification of intensity shown in (d). Data represent the mean ± SD from on 3 independent experiments. *$p < 0.05$ vs. control. ***$p < 0.001$ vs. control.

2.3.6 In vitro and in vivo toxicity detection

The *in vitro* cytotoxicity of native GVs and PH-GVs on SCC7 cells was investigated by incubating them with diverse concentrations of GVs (0-1 nM) followed by a CCK-8 assay. Incubation with native GVs, broken native GVs (collapsed using US) or PH-GVs for 24 hours did not induce any noticeable reduction in cell viability at any concentration (Figure 2.10a). Incubation with any GV group with incubation time doubled to 48 hours also did not result in decreased cell viability at any concentration (Figure 2.10b). We thus see that no GV group, including our surface-modified ones, showed any significant cytotoxicity to cells, indicating their general level of safety. We then evaluated the *in vivo* toxicity of the GV treatment on the normal, non-tumor organs of the treated mice by H&E staining. The gross morphology of all vital organs observed in either GV group showed no major differences compared to the PBS control (Figure 2.10c). No obvious signs of damage or toxicity were visible in the pathologies of the heart, liver, spleen, lung, and kidneys. The body weights of tumor-bearing mice over the 30-day period of testing were also tracked, and we found that groups of mice injected with GVs or PH-GVs showed no major difference in body weights (Figure 2.10d), confirming our *in vitro* observations of non-cytotoxicity.

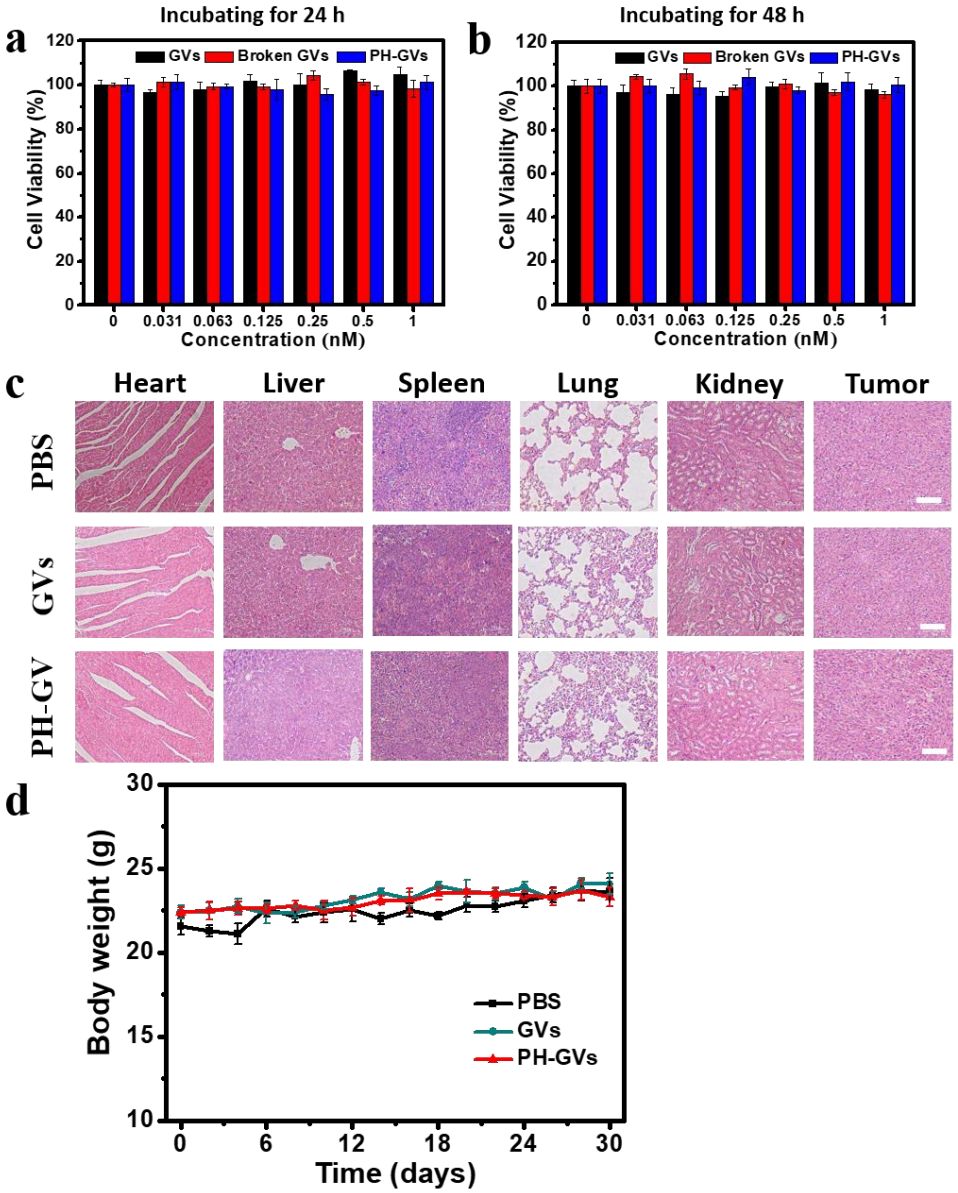

Figure 2.10 Toxicity of PH-GVs both *in vitro* and *in vivo*. Viability assay of SCC-7 cells after treatment with GVs, collapsed GVs and PH-GVs at the concentration of 0.031-1 nM for 24 h (a) and 48 h (b). (c) Representative H&E sections of the vital organs (heart, liver, spleen, lung, and kidney.) and tumors after GVs/PH-GVs treatment for 30 days. Scale bars, 100 μm. (d) Body weights were measured during the 30-day evaluation period in mice under different conditions. Data represent the mean ± SD from 4 independent experiments.

2.4 Conclusion

The search for appropriate contrast agent which is small enough to pass through the vasculature to access the intercellular space of tumors is a critical concern in the field of molecular ultrasound imaging. In the present study, we successfully synthesized PH-GVs by combining GVs with PEG, which reduced RES uptake and increased blood circulation time, as well as a tumor-targeting ligand-HA. We demonstrated that our synthesized PH-GVs showed good biocompatibility and targetability both in *vitro* and in *vivo*. PH-GVs resulted in reduced uptake in the liver, prolonged blood circulation, selective accumulation at the tumor site, as well as improved tumor targeting effects. Crucially, PH-GVs were seen to be good ultrasound contrast agents in CD44-positive tumor imaging. Such improvements could enable GVs to truly fulfill their potential as a high-performance nanoscale molecular reporter for ultrasound imaging as well as a potential carrier for CD44-positive tumor therapy.

CHAPTER 3 Gas-filled Protein Nanostructures as Cavitation Nuclei for Molecule-Specific Sonodynamic Therapy

3.1 Background

In the past several decades, the first-line treatments for most cancers have been surgical resection, chemotherapy, and radiotherapy, and they have provided significant benefits to patients [7, 17, 82, 83]. Simultaneously, significant attention has been paid to the development of new, more efficient therapeutic modalities. Sonodynamic therapy (SDT) has emerged as a promising non-invasive therapeutic modality [18, 36, 39, 84]. SDT combines low-intensity ultrasound and a 'sonosensitizer' to generate cytotoxicity in tumors [37, 41, 85]. It has the advantage of being able to target tumors with high spatial resolution, since ultrasound can be focused on a single point deep within tissues in three dimensions while leaving normal tissue undamaged [36, 38]. Such precise disruption of selected tissues using focused ultrasound provides an advantage in therapeutics for deep-seated tumors [37-39, 86]. However, targeting a specific cellular population within a tissue mass is still a challenge for SDT due to the off-target effects of sonosensitizers and the non-selectivity of ultrasound application.

Ultrasound enables SDT by inducing the occurrence of inertial cavitation, which is the process of nucleation, growth, and implosive collapse of bubbles during which extreme temperatures and pressures are generated [37, 41]. It has been suggested that

inertial cavitation events during SDT can generate light through sonoluminescence and potentially activate sonosensitizers to generate ROS [18, 37, 41]. Concurrently, the localized high temperatures generated by inertial cavitation are also believed to generate free radicals which then directly react with endogenous substances to generate ROS [18, 36, 41]. Thus, being able to accurately modulate and enhance inertial cavitation is critical for precise targeting as well as ROS generation and the subsequent therapeutic efficacy. *In vivo* cavitation nucleation thresholds are usually high (5-7 MPa) due to a lack of naturally occurring nuclei, and targeted contrast agents like microbubbles are usually added to lower the nucleation threshold, making cavitation more specific and easier to sustain and control [40, 87-90]. However, the *in vivo* dwell time of microbubbles is limited due to their inherent instability and their micron size preventing them from extravasating to tumor sites, which compromises their therapeutic capability [40, 42, 44, 46].

Recently reported gas-filled protein nanostructures called gas vesicles (GVs) have demonstrated enhanced ultrasound imaging contrast, comparable to MBs [30, 50, 51, 54, 59, 91]. Unlike microbubbles, GVs are biogenic nanobubbles derived from buoyant cyanobacteria, composed of a hydrophobic interior protein layer and a hydrophilic exterior protein layer [48-50, 68]. This special structure allows GVs to exclude water but allow gas exchange through the protein shell, endowing them with robust physical stability [48, 51]. Our lab has recently shown that functionalized GVs were capable of extravasating into deep tumor regions and target $CD44^+$ tumor cells specifically *in vivo*

[92].

Given the hollow structure of GVs and their MB-like ultrasound contrast enhancement capability, we hypothesized that GVs could serve as ultrasound-responsive cavitation nuclei to facilitate cavitation, making them theranostic nanoparticles to enable targeted disruption of tumors and SDT enhancement. Furthermore, functionalized GVs could improve SDT's potency by allowing the targeting of a specific cell population. In the present study, we show that adding GVs to SDT can significantly enhance the treatment's efficacy. We found that GVs enhanced ROS production when sonicated in solution. The effects of GVs on cell viability and cell apoptosis during SDT were examined, and the presence of GVs was found to significantly increase the production of ROS and cell apoptosis, and to decrease cell viability compared to the sonosensitizer alone. The effects of GVs on tumor growth and tissue damage during SDT was also determined *in vivo*. GV-mediated SDT was found to significantly increase apoptosis and tumor cell damage *in vitro*. Functionalized GVs targeting $CD44^+$ tumor cells which can extravasate tumor vessels [74-78, 92] were found to accumulate in an *in vivo* tumor site for up to 12 hours post-administration *in vivo,* and GV-mediated SDT was found to significantly increase apoptosis and tumor cell damage. Thus we found that the GVs' presence enabled targeted disruption of selected cells within the area of insonation without obvious off-target effects. In all, we provide evidence for GVs being an efficient and simple way to enhance the efficiency of targeted SDT against tumors.

3.2 Materials and methods

3.2.1 Reagents and antibodies

Dulbecco's Modified Eagle Medium (DMEM), Fetal bovine serum (FBS), trypsin-EDTA (0.25%) solution and Penicillin-streptomycin solution were purchased from Life Technologies (Carlsbad, CA, USA). Annexin V-FITC/PI Apoptosis Detection Kit and 2',7'- dichlorodihydrofluorescein-diacetate (H_2DCF-DA) were purchased from Invitrogen (Carlsbad, CA, USA). CCK-8 assay kit was purchased from Sangon Biotech (Shanghai, China).

3.2.2 Ultrasonic setup for SDT

For SDT experiments, 1 MHz planar ultrasonic transducer with a diameter of 5 cm (A303S, Olympus, Tokyo, Japan) was used for sonification in this study. Function generators (Tektronix AFG3251, Agilent Technologies, USA) and 50dB-gain power amplifier (A075; Electronics & Innovation Ltd, USA) were used to generate ultrasonic pulses. Cell culture dishes were placed on top of the transducer, coupled with a layer of ultrasound gel at 25 ℃. Acoustic intensity and field were characterized by hydrophone (HNP-1000, Onda, Sunnyvale, CA, USA; pre-amplifier: AH-2010, Onda, Sunnyvale, CA, USA). The cell culture was sonicated with bursts of duty cycle 50% at pulse repetition frequency (PRF) 1 kHz, under pulses with pulse width 1 s and pulse interval 1.5 s. The spatial peak temporal peak intensity was measured to be 11.7 W/cm^2 and

overall sonication duration was 5 minutes. The temperature increase was controlled within 2.5 °C, as monitored with a thermometer (Checktemp®1 HI98509, Hanna Instruments, Woonsocket, RI, USA). This setup was applied in the solution, *in vitro* as well as *in vivo*.

3.2.3 Cell culture and SDT

Squamous cell carcinoma (SCC-7 cells) were purchased from Cell Bank of Type Culture Collection of the Chinese Academy of Sciences (Shanghai, China). SCC-7 cells were maintained in Dulbecco's modified Eagle's medium (DMEM, Life Technologies, Carlsbad, CA, USA) supplemented with 10% fetal bovine serum (FBS, Life Technologies), 100 units/ml penicillin, and 100 μg/ml streptomycin. Cells were maintained at 37°C in a humidified chamber containing 95% air and 5% CO_2. Cells at a confluence of 80% were digested with 0.25% trypsin for subculture. Functionalized GVs were used for *in vitro* experiments. Cells were divided into eight treatment groups: (1) PBS(US-), (2) GVs(US-), (3) PpIX(US-), (4) PpIX+GVs(US-), (5) PBS(US+), (6) GVs(US+), (7) PpIX(US+), (8) PpIX+GVs(US+). Protoporphyrin IX (PpIX) disodium salt was purchased from Sigma-Aldrich, reconstituted in 100% DMSO (Sigma-Aldrich, St. Louis, MO, USA) to 1 mM and stored at 4°C. For PpIX treatment, cells were incubated with PpIX (1 μM) for a 1-hour drug-loading time in DMEM medium supplemented with 10% FBS. The concentration of GVs used in cell culture was 2 nM. After ultrasound treatment, cells were cultured in fresh medium for 4 hours and then

prepared for different analyses.

3.2.4 ROS detection in solution and in vitro

For singlet oxygen detection in the solution, Singlet Oxygen Sensor Green (SOSG) solution (10 μM) in degassed PBS (pH 7.4) was added into PpIX (1 μM) with or without GVs (2 nM). The solution was exposed to ultrasound in the dark. The fluorescence intensity of SOSG was measured by a microplate reader at an excitation wavelength of 488 nm and at an emission wavelength of 530 nm. This protocol was repeated for the control group (degassed PBS). Intracellular ROS production was measured using DCFH-DA(Sigma-Aldrich). Briefly, 10 μM DCFH-DA diluted with PBS were added to SCC-7 cells at 37°C for 20 min. Cells were then washed with PBS three times. Labeled cells were trypsinized and observed by fluorescent microscopy with X20 (Nikon, Tokyo, Japan).

3.2.5 Cell viability, apoptosis detection

Cell viability was determined using a Cell Counting Kit-8 (Sigma-Aldrich) according to the manufacturer's instructions. Briefly, cells were plated at a density of 5 x 10^3 cells per well in a 96-well plate and incubated in 100 μl culture medium for 24 hours. After SDT treatment, cytotoxicity was determined by adding 10 μl CCK-8 reagent per well for 1 hour at 37°C in 5% CO_2. The absorbance of the treated samples against a blank control was measured at 450 nm by a microplate reader (Bio-Tek Instrument Inc, USA). The relative viability of treated cells was determined by

comparing with control group. Cell apoptosis was tested by Alexa Fluor 488 Annexin V/Dead Cell Apoptosis Kit (Thermo Fisher Scientific) according to the manufacturer's instructions. Briefly, cells were seeded at a density of 5×10^5 cells in 6 cm dishes and treated with SDT. After different kinds of treatment, Cells were collected and incubated with 5 μl annexin V conjugate and 1 μl PI working solution at room temperature for 15 minutes. Cells were then analyzed by FACS Calibur flow cytometer (Becton-Dickinson, USA). The percentage of apoptosis and necrosis were analyzed by BD Accuri C6 Software (Becton-Dickinson, USA).

3.2.6 In vivo SDT

All procedures using laboratory animals were approved by the Department of Health, The Government of the Hong Kong Special Administrative Region, and the Hong Kong Polytechnic University Animal Subjects Ethics Sub-committee. 5-7 weeks female athymic nude mice weighing 16-18 g were supplied by the Animal Resource Centre of The University of Hong Kong. The mice were acclimated to the room for one week after arrival and were maintained on a normal 12-hour light-dark cycle. The mice were housed in conventional cages (6 animals/cage) with free access to standard pellet diet and water in specific pathogen-free conditions with 24±2°C temperature, 60-70% relative humidity. Standard wood chips for mice were used as bedding material. After 1 week's acclimation, 4×10^6 squamous cell carcinoma cell line (SCC-7) in PBS (80 μl) were injected into the rear dorsal flank of nude mice by subcutaneous injection. Tumor

formation occurred approximately two weeks after cell implantation and experiments were begun when tumor volume reached ~ 150 mm^3.

For *in vivo* SDT, PpIX was administrated at the dose of 5mg/kg through pure topical injection around the tumor 1 hour before SDT treatment. Functionalized GVs were used for *in vivo* experiments. The mice were randomly subdivided into five groups, including (1) PBS (US-), (2) PBS (US+), (3) GVs (US+), (4) PpIX (US+), (5) PpIX+GVs (US+). The tumor size and body weight of each mouse were measured every 3 days following the treatment. Subcutaneous tumor volume was estimated by the following formula: Tumor volume $\approx$ largest diameter $\times$ smallest $diameter^2/2$. All mice were sacrificed on day 15 and tumor tissues were collected and fixed in 4% paraformaldehyde for 24 hours, processed through conventional histological techniques, and stained with hematoxylin and eosin (H&E). Images were captured by a Nikon optical microscope (Tokyo, Japan) and analyzed using Nikon NIS-Elements software.

3.2.7 Statistical Analysis

Statistical analysis was performed with GraphPad Prism software. Image J, Photoshop CS, and Illustrator CS software were used for image processing following the general guidelines. All data, expressed as mean ± SD, were analyzed with a two-tailed student's *t*-test or by one-way ANOVA. *P*-values <0.05 were considered statistically significant.

3.3 Results

3.3.1 GVs mediated ROS production in the solution.

To determine whether there was direct ROS production during the interaction of GVs with ultrasound, we used the fluorescent probe SOSG (10 μM) to detect the production of singlet oxygen in a cell-free system. There were minimal fluorescent signals without ultrasound, but large increases in SOSG fluorescence were observed upon sonication in the PpIX group (1 μM), GV group (2 nM), and PpIX+GVs group under sonication, indicating singlet oxygen production (Figure 3.1a). The PpIX+GVs group showed the highest singlet oxygen production under sonication and was significantly higher than that of either GVs or PpIX alone. This indicates a synergistic effect of combining GVs with PpIX, leading to enhanced ROS production upon sonication. We also found that increasing GV concentration in the presence of PpIX resulted in greater ROS production upon insonation (Figure 3.1b).

a.

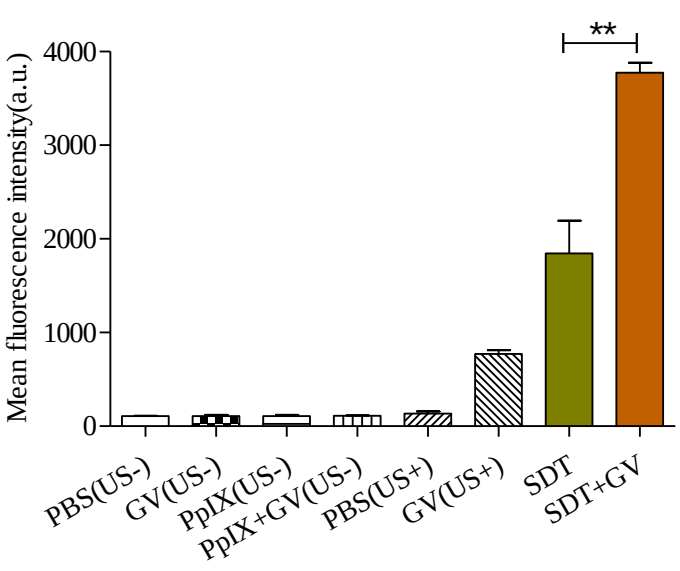

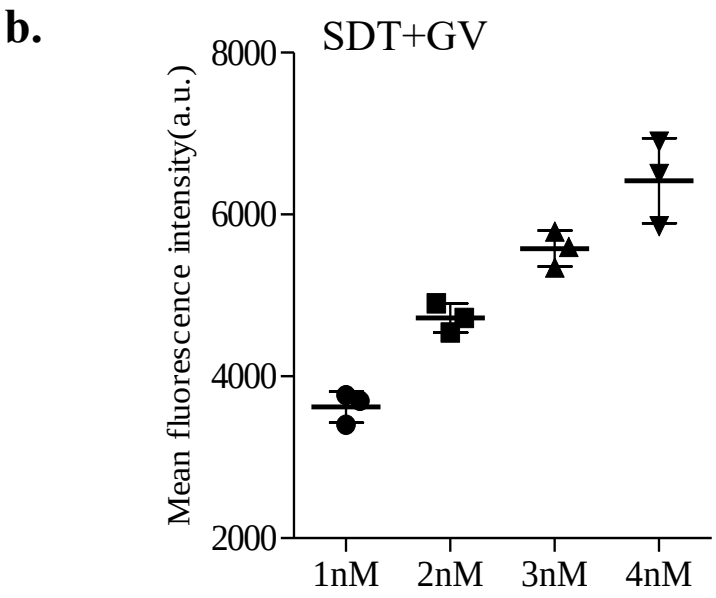

Figure 3.1 GVs mediated ROS production in the solution. PBS, GVs(2nM), PpIX(1μM), and PpIX+GVs group were treated with/without US irradiation for 5min, singlet oxygen production in the solution was then determined in (a) using SOSG under fluorescent microplate reader. Quantitative analysis was from three independent experiments. **p<0.01 vs. control. (b) The change of SOSG fluorescence intensity in PpIX+GVs group as GV concentration increased. Data represented as mean ± SD (n=3).

3.3.2 GVs mediated ROS production in vitro.

We next investigated whether the presence of GVs during SDT could enhance intracellular ROS production *in vitro* by monitoring DCHF-DA fluorescence through flow cytometry and imaging. As expected, while ROS production increased in the GVs and PpIX groups compared to PBS when sonicated, PpIX+GVs consistently showed the highest ROS production, being significantly higher than the PpIX-only group (Figures 3.2a-b). Little signal was observed among those groups without ultrasound irradiation. These data show that adding GVs could significantly enhance intracellular ROS production for $CD44^+$ tumor cells during SDT *in vitro*.

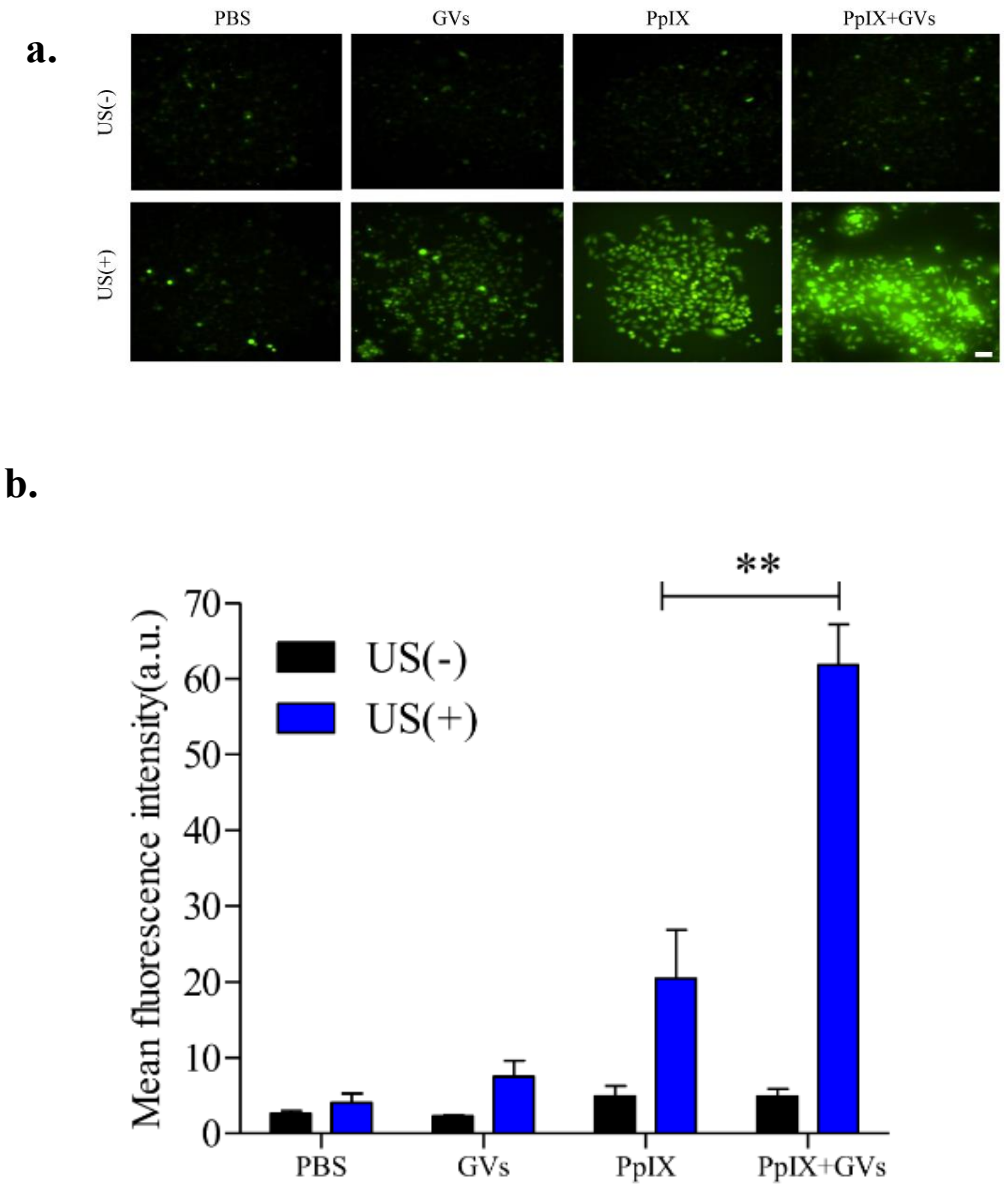

Figure 3.2 Functionalized GVs mediated ROS production in vitro. (a) Cells were treated with PBS, GVs(2nM), PpIX(1μM), or PpIX+GVs for 1 hours followed by US irradiation(with/without) for 5min. Intracellular ROS production was then determined 4h after US treatment. ROS generation as indicated by DCF fluorescence was measured by fluorescent microscope. Representative images were shown in (a) with quantification data in (b). Quantitative analysis was from three independent experiments. **p<0.01 vs. control. Scale bar represents 50μm.

3.3.3 GVs mediated cell viability and apoptosis detection.

Next, the efficacy of GVs on the cytotoxicity of *in vitro* SDT on SCC-7 cells was explored. Cells were incubated with PBS,1 μM PpIX or/and 2 nM GVs for 1 hours, followed by US irradiation. The cell viability of SCC-7 cells was determined using a CCK-8 assay. The PpIX and GVs groups each showed some decline in cell viability, but the PpIX+GVs group showed the lowest cell viability, significantly lower than that of the PpIX-alone group (Figure 3.3a). No decline in cell viability was evident among those groups without sonication. The enhancement of cytotoxicity of *in vitro* SDT by GVs was further confirmed by evaluating apoptosis 4 hours following SDT treatment. Over 90% of cells were found to be normal in all the unsonicated groups as well as the PBS+US and GVs+US groups; while this number decreased to ~ 75% in the PpIX group, it was significantly lower in the PpIX+GVs (65.4%) group under ultrasound treatment (Figure 3.3b). The levels of late apoptosis and necrosis observed in this group were also found to be much higher than in all other groups. Thus, we found that the existence of functionalized GVs could induce significantly higher cell death and apoptosis than SDT-alone, leading to higher therapeutic efficacy for $CD44^+$ tumor cells.

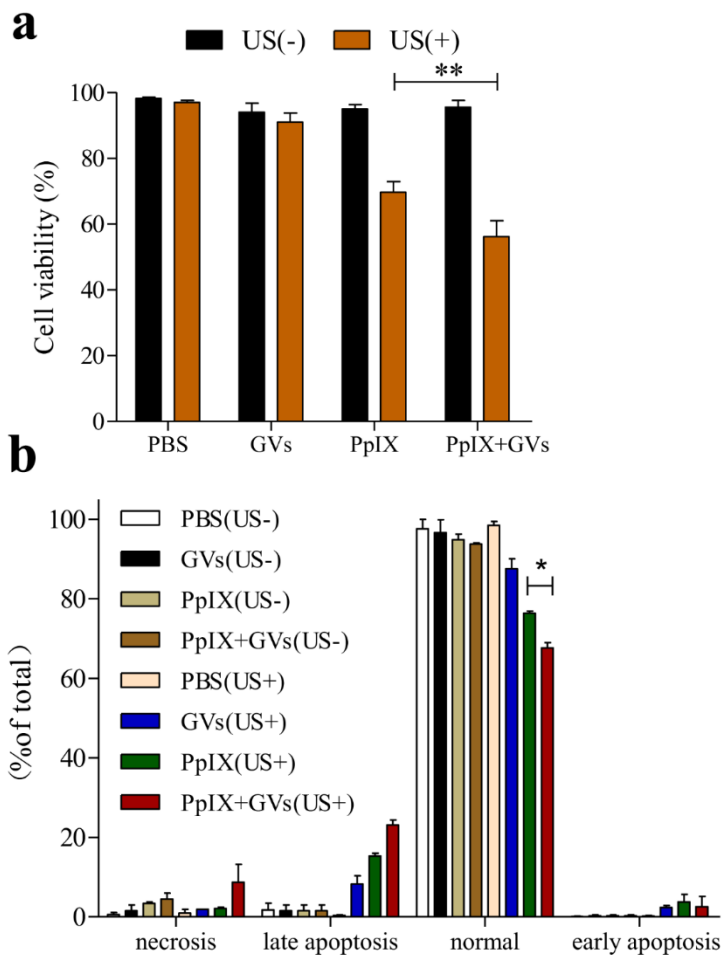

Figure 3.3 In vitro cell viability and apoptosis assay of functionalized GVs mediated SDT. Cells were treated with PBS, GVs(2nM), PpIX(1μM), or PpIX+GVs for 1 hours followed by US irradiation(with/without) for 5min. Cell viability and apoptosis were then determined 4h after US treatment. (a) The relative cell viability of SCC-7 cells after different treatments was determined by CCK-8 assay. Data represent the mean ± SD based on 3 independent experiments. **$p < 0.01$ vs. control. (b) Evaluation of cell apoptosis following different treatments was done by flow cytometry through Annexin-V and propidium iodide (PI) double staining. Data represent the mean ± SD based on 3 independent experiments. *$p < 0.05$ vs. control.

3.3.4 In vivo SDT assay

We finally evaluated the effect of functionalized GVs on PpIX-mediated SDT in

vivo. SCC-7 cells were used injected in athymic nude mice to induce tumor formation, and treatments began when subcutaneous tumor volume reached 150 mm^3. For SDT treatment, functionalized GVs (200 μl, 20 nM) were injected 12 hours before ultrasound irradiation by tail injection and PpIX injected intravenously into the tumor 1 hours before ultrasound irradiation. Tumor volumes and body weight were measured every three days after various treatments. Rapid and continuous growth of tumors was observed in PBS (US-), PBS (US+), and GVs (US+) group for the following 15 days, with tumor volume reaching nearly 1000 mm^3 (Figure 3.4a). For SDT treatment groups, both PpIX (US+) and PpIX+GVs (US+) exhibited effective growth inhibition efficacy, as tumors were found to shrink significantly in the three days following SDT treatment and to regrow slowly at a slower rate. Crucially, the PpIX+GVs (US+) group showed significantly smaller tumors and slower growth rate than the PpIX (US+) group. No major changes in the body weights of mice in different groups were observed throughout the experimental period (Figure 3.4b), indicating low systematic toxicity. The tumors were then excised and stained with H&E or a TUNEL assay to directly observe the effects of the SDT treatment. Compared to control group, which showed normal morphology, H&E staining in both PpIX (US+) and PpIX+GVs (US+) groups revealed severe damage, with the latter showing the most significant toxicity effects (Figure 3.4c). Similarly, a TUNEL assay revealed much higher levels of apoptosis in PpIX+GVs(US+) than in the PpIX(US+) group, with almost no apoptosis in PBS(US-), PBS(US+), and GVs(US+) groups (Figure 3.4d). Taken together, these results

demonstrated the potential of functionalized GVs to enhance SDT outcomes *in vivo*, in particular their capability to target the tumor site specially and induce tumor toxicity.

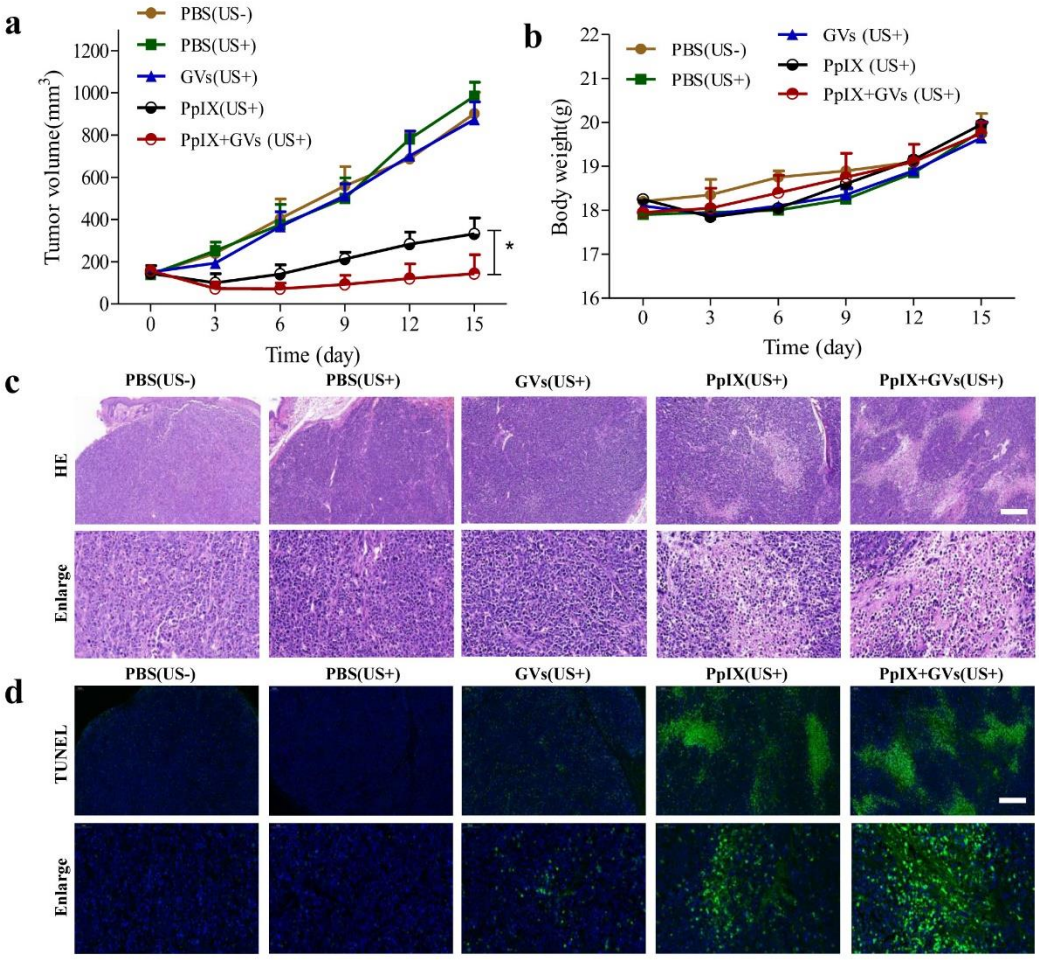

Figure 3.4 Functionalized GVs mediated SDT *in vivo*. (a) The effects of GVs on *in vivo* SDT were determined. Tumor growth curves of SCC7 tumor-bearing mice with different treatment groups. n = 5 mice per group, *p < 0.05 significance level. (b) Bodyweight of SCC7 tumor-bearing mice after various treatments. (c) Representative histological images of H&E stained tumor slices collected from different groups. Scale bar represents 200 μm. (d) Representative images of TUNEL assay of tumor slices collected from different groups. Scale bar represents 200 μm.

3.4 Conclusion

In the present study, we lay out a role for a GV-based nanoplatform for enhanced targeted sonodynamic therapy of cancer cells. We consistently found that a larger quantity of ROS was generated both in solution and in *vitro* with the addition of GVs during SDT. Obvious increases in cell death and apoptosis were observed with the addition of GVs compared to SDT alone. *In vivo*, GVs were observed to enhance the damage induced by SDT to tumors, as well as inhibit tumor regrowth. We also augmented the treatment by using functionalized GVs with ultrasound to enable more selective SDT treatment. This allowed targeted disruption of selected ($CD44^+$) cells in the area insonated. In addition, no ROS production, cellular apoptosis or cell death were observed with GVs alone, nor were other major indications of treatment-induced systemic toxicity observed. These results show GVs to be well-tolerated compared to other organic or inorganic materials, consistent with our previous studies [30, 92]. Thus, GVs consistently increased the efficacy of SDT *in vitro* and *in vivo* by significantly increasing the ROS production and are a promising nanoplatform for more targeted therapeutic efficacy under ultrasound irradiation. The ability of GVs to serve as therapeutic enhancers in addition to their well-established role as ultrasound contrast agents also makes possible their application as theranostic particles for even further-improved treatments such as ultrasound imaging-guided targeted cancer therapy.

While our results are encouraging, further study is needed to achieve greater spatial and molecular specificity. In particular, research is required to study the influence of functionalized GVs' physical and chemical properties on therapeutic

efficiency and their ability to target desired cells during SDT. Ultrasonic parameters such as intensity, mechanical index, and duty cycle may all have effects on GVs' effects and could be tuned to increase or even optimize treatment efficacy. Additional engineering of GVs may also be needed to achieve better cellular targeting, such as using more tumor-specific cell surface markers, or a combination of cell-surface molecules to better tailor the enhanced SDT treatment. Such modifications in the treatment scheme would require deep systematic study, but could enable SDT treatments that are more targeted and more effective in future.

CHAPTER 4 Biogenic nanobubbles for effective oxygen delivery and enhanced photodynamic therapy of cancer

4.1 Introduction

The existence of hypoxia is a common characteristic of most solid tumors, caused by low vascular density, irregular vascular geometry and an imbalance between oxygen consumption and supply at the tumor site. This often compromises any cancer therapies that may be applied. Hypoxic cells are more resistant to radiotherapy, chemotherapy and other oxygen-consuming therapies such as photodynamic therapy (PDT)[19, 93]. This is exacerbated by the fact that hypoxia is closely associated with a high risk of metastasis, further worsening therapeutic outcomes. Given hypoxia's obstructive role, tumor oxygenation is considered an important auxiliary method for anticancer therapy[94, 95]. Tumor oxygenation has been tried in two primary ways: increasing blood oxygenation in general or increasing oxygen delivery at the tumor site. Hyperbaric oxygen (HBO) and hyperbaric carbogen are common ways to reduce tumor hypoxia by increasing the amount of dissolved oxygen in blood throughout the body[96-98]. However, not only are these methods prohibitively expensive, their generic, untargeted nature could lead to severe deleterious off-target side-effects. An alternative approach is to use molecular oxygen carriers, that can bind oxygen with high affinity and enable rapid and targeted tissue delivery. Perfluorocarbon (PFC) emulsions

and acellular hemoglobin-based oxygen carriers (HBOCs) were initial attempts at oxygen delivery to tumors. Unfortunately, such carriers failed due to their merely marginal benefits and severe side effects in clinical trial[99-101].

More recently, efforts have been made to develop synthetic microparticles and nanoparticles such as oxygen-filled microbubbles and nanoparticle-based HBOCs. Notably, oxygen-filled lipid microbubbles have shown good capability as oxygen carriers[102-104]. These microbubbles, usually coated with a layer of lipid, can hold large amounts of oxygen in their gas core. Microbubbles have also been demonstrated to change the hypoxic microenvironment *in vivo* and enhance outcomes for chemotherapy and radiotherapy[103, 105-108]. Thus, oxygen-filled microbubbles constitute a promising new way to deliver oxygen to hypoxic tumor sites for therapeutic purposes. However, despite their effectiveness in delivering oxygen to tissues, various studies also revealed critical limitations in their anticancer abilities. Microbubbles have limited intravascular dwell time due to their relatively large sizes (> 1μm). Thus, repetitive administration is required for continuous oxygen delivery, which increases the viscosity of serum and causes long-term toxicity in blood and tissues[109, 110]. Lipid microbubbles may also suffer from stability issues such as dissolution and coalescence when entering the circulation, correlated with greater product loss, possibly leading to excessive production of reactive oxygen species (ROS) and adverse oxidative stress[106, 111, 112]. Such lipid microbubbles are, thus, not ideal candidates for oxygenation of tumor tissues in the body. Stable oxygen-filled nanobubbles which do

not undergo dissolution and coalescence may provide an alternative that could overcome the aforementioned limitations of microbubbles. Nanobubbles are established as having long intravascular dwell times, and their smaller size could exploit enhanced permeability and retention (EPR) effects to pass through the leaky vasculature of tumors to deeper sites[46, 106]. These properties enable nanobubbles to stay longer and go deeper into the tumor site, paving the way for potential improvement of clinical outcome[113, 114]. Nanobubbles such as dextran nanobubbles, polymer, and lipid nanobubbles have also been developed for oxygen delivery in initial studies[115-119]. Nevertheless, limitations such as instability and relatively lower half-life also exist for those synthetic nanobubbles.

Gas vesicles (GVs), a nanoscale hollow structure, have recently been reported as the first biomolecular acoustic reporters with gene editability and inherent stability.[50, 51, 54, 92, 120] In contrast to synthetic nanobubbles, GVs naturally occur gas-filled cavities formed by cyanobacteria or archaea as a means to control buoyancy for optimal access to light and nutrients in the water. They are hollow protein shells with sizes different from 200-400 nm[49]. The mechanism to load GVs with gases is significantly different from that of regular microbubbles/nanobubbles. Typically, microbubbles/nanobubbles depend on the lipid shell to encapsulate gases, creating a gradient between internal and external pressure, and the addition of surfactant stabilizers is needed to stabilize them[109, 110]. However, the walls of GVs exclude water but allow gas to permeate in and out the shells freely. Hence, only a minimal

pressure gradient is created, allowing GVs significantly greater stability than nanoscale bubbles[49, 51]. Additionally, the protein surface of GVs is amenable to modification, and this could be used to endow GVs with additional physical or chemical properties that may help them to be better oxygen carriers[67].

To attain better oxygen delivery efficacy, we fabricated lipid coated GVs and investigated their ability as a new platform to elevate oxygen concentration in hypoxic tumor sites. We found the GVs to be nanosized and stable in solution over 6 months. We evaluated whether lipid-GVs(O_2) administration treatment could alleviate hypoxia both in cultured cells and in a hypoxic tumor model and found that they significantly improved oxygen delivery compared to native GVs(O_2). Furthermore, we verified the effects of lipid-GVs(O_2) using photodynamic therapy (PDT). PDT is an oxygen-consuming therapy and the efficacy of PDT is dependent on oxygen related generation of ROS[16, 28, 121-124]. The presence of lipid-GVs(O_2) significantly improved ROS production and reduced cell viability in combination with PDT compared to PDT alone, while causing no notable toxicity by themselves. This combination PDT treatment also significantly reduced tumor size *in vivo* and increased the number of apoptotic cells, with obvious damage visible in excised tumors. Thus, this study lays the groundwork for lipid-coated GVs as an oxygen-delivery vehicle to safely enhance the efficacy of PDT.

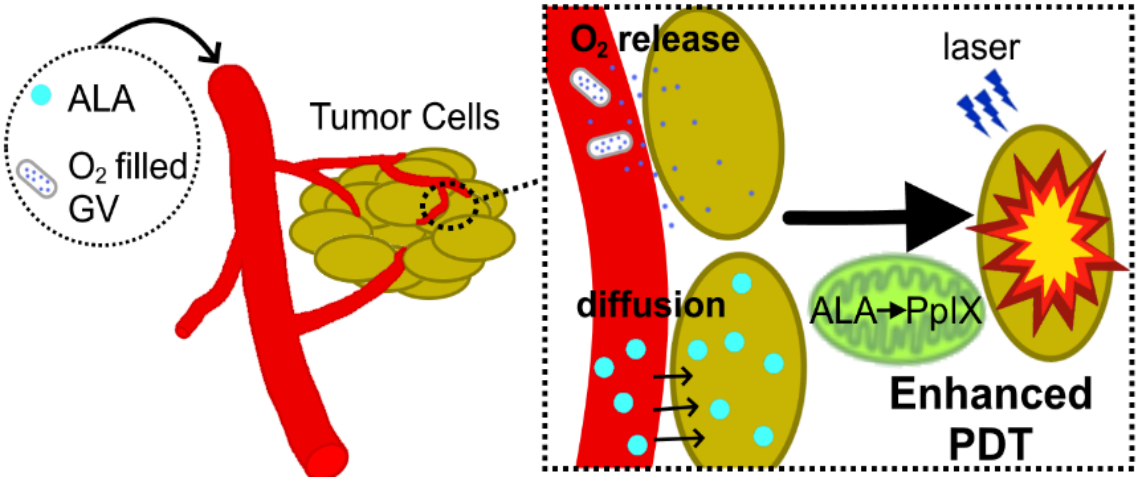

Figure 4.1 Schematic illustration of lipid-GVs(O2) on the efficacy of PDT.

4.2 Methods

4.2.1 Preparation，surface modification and characterization of lipid-GVs

Anabaena flos-aquae (FACHB-I255, Freshwater Algae Culture Collection at the Institute of Hydrobiology, China) were cultured in sterile BG-11 Medium (Sigma, St. Louis, MO, USA) at 25°C under fluorescent lighting with I4hr/10hr light/dark duty cycle. Algae were hypertonic lysed with a 25% concentration of sucrose solution when they became mature, and GVs were then released from the algae. GVs were then isolated by centrifugation at 600g for 3 h and isolated GVs could form a white layer on the top of the solution after centrifugation. GVs was purified three times with phosphate-buffered saline (PBS) and stored in PBS at 4°C. The concentration of GVs was measured by optical density method characterized by 500 nm wavelength light (OD500) by UV-Visible spectrophotometer (2100 pro, GE Healthcare Ltd, Piscataway, NJ, USA) and calculated to mole concentration with the ratio of 450 pM/OD500[51].

To modify the GVs surfaces, 6 μl of 18 mg/ml dioleoyl phosphatidylcholine (DOPC) (Thermo Fisher Scientific, MA, USA) was dissolved in 2 ml chloroform (Thermo Fisher Scientific, MA, USA) in a 25 ml round-bottom flask. The solvent was then evaporated and the samples were dried in a vacuum rotary evaporator. 1 ml of 20 mM HEPES buffer (pH = 7.2, Thermo Fisher Scientific, MA, USA) was then added to the dried lipid layer, forming a cloudy solution after vigorous agitation. The mixture was then probe-sonicated (20 W, 15 s pulses for 20 min) for 3–5 min until the solution

became clear. The resulting liposome solution was stored at 4°C for further use. 1 ml prepared liposome solution was added to 1 ml of 1 nM GV solution and incubated overnight on a rocker platform. GVs were then washed three times by centrifugation (24,000 rpm, 10 min) and resuspended in PBS. Finally, lipid-GVs were resuspended in PBS for use in experiments [125-127].

In order to understand the biodistribution of lipid-GVs *in vivo,* indocyanine green (ICG) (Sigma-Aldrich, St.Louis, MO) was used to label lipid-GVs. ICG was added during liposome preparation at a ratio of 20μg ICG:5nM lipid-GVs. To completely incorporate ICG into the lipid membrane, ICG dissolved in 100% CH_3OH was added to the lipid mixture prior to it being dried into a thin film [128]. Light exposure was avoided during fabrication of ICG labeled lipid-GVs.

For characterization of GVs, size distribution and zeta potentials were determined by laser light scattering using a 90 Plus instrument (Brookhaven, Holtsville, NY, USA) at a fixed angle of 90° and a temperature of 25 °C. UV-Vis absorbance spectra of ICG and ICG-lipid-GVs were determined by a Multiskan Go microplate reader (Thermo Fisher Scientific, Massachusetts, USA). The size and morphology were determined by Transmission Electron Microscopy (TEM) with the operating voltage of 200 kV. Samples of GVs (OD 0.1) were deposited on a carbon-coated formvar grid. To measure the stability of GVs, single particle size and concentration of the formulation were determined in the first month and the sixth month respectively.

4.2.2 Determination of oxygen release kinetics of lipid-GVs in solution

The oxygen concentration in the solution was monitored using an oxymeter (Portamess 913 OXY, Knick, Germany) and the data were recorded as mg/l. Before each experiment, the oxymeter was calibrated in air, after waiting for stable temperature and humidity conditions to be re-established. Oxygen filled PBS (PBS(O_2)), oxygen filled GVs (GVs(O_2)), and oxygen filled lipid-GVs(lipid-GVs(O_2)) were prepared by a continuous oxygen purge for 20 min. To determine oxygen release kinetics of GVs, 1ml PBS(O_2), GVs(O_2) or lipid-GVs(O_2) (filled with oxygen, sealed into vials) were injected into the 5ml hypoxic solution and the oxygen concentration of the solution was monitored over time. The hypoxic solution was obtained by a continuous N_2 purge until the oxygen concentration in PBS was finally reduced to 0.8 mg/l (severe hypoxia). All the experiments were performed in triplicate.

4.2.3 In vitro O_2 delivery test of lipid-GVs(O_2)

Human hepatoma cell line (HepG2) were obtained from the cell bank of the Chinese Academy of Science, Shanghai, China. HepG2 were cultured in high-glucose (4.5 g/l) Dulbecco's modified Eagle's medium with L-glutamine (Thermo Fisher Scientific, MA, USA) following standard cell culture instructions. All media were supplemented with 10% (vol/vol) fetal bovine serum, penicillin (100 U/mL) and streptomycin (100μg/ml) (Thermo Fisher Scientific, MA, USA). Cells were grown at 37°C in a 5% CO_2 and 95% air atmosphere until 70%-80% confluence before

trypsinization and harvesting for *in vitro* studies. For hypoxia detection, cells were cultured in a hypoxic chamber (1% oxygen, 5% CO_2) overnight before the experiment. Hypoxic conditions in the media were monitored using Image-iT™ Red Hypoxia Reagent (5μM) bought from Thermo Fisher. This hypoxia reagent could measure hypoxia in live cells and it is non-fluorescent when live cells are in an environment with normal oxygen concentration and show fluorescent when oxygen levels decrease. Besides, it is a real-time oxygen detector with a fluorogenic response changes according to the surrounding oxygen levels. The reagent was added into the medium and co-cultured with cells at the beginning of the experiment and the fluorescence of the reagent was monitored before/after the addition of lipid-GVs(O_2). lipid-GVs(O_2) (1nM) were co-cultured with cells for an hour during the experiments. Cells were then visualized under laser-scanning confocal microscopy with X63 objective (Nikon, Tokyo, Japan) and the intensity of fluorescence was quantified by Image J.

4.2.4 In vitro photodynamic therapy.

5-aminolevulinic acid (ALA) which was obtained from Sigma (St Louis, MO, USA) was used in this experiment as the photosensitizer. It was dissolved in PBS to a stock concentration of 1M and was stored in the dark at -20°C. For the ALA treatment, cells were incubated with 1mM ALA for a 4 h drug-loading time in DMEM medium supplemented with 10% FBS. The optical setup for PDT treatment is shown in Figure 5A. Cells under PDT treatment were exposed to laser with a power of 100 mW/cm^2

for 5min. The light source was generated with a wavelength of 405 nm by an optical fiber was collimated to an aperture and irradiated to the 35mm cell culture dish. The position of the cell culture plate was manually controlled by a two-axis motorized linear stage. After the treatment, the cells were cultured in fresh medium for different times and then prepared for different analyses.

4.2.5 Cell viability, apoptosis, and intracellular ROS production assay.

Cell viability at 4h following PDT was determined using a Cell Counting Kit-8 (Sigma-Aldrich) according to the manufacturer's instructions. Briefly, cells were plated at a density of 5000 cells per well in a 96-well plate and incubated in 100μl culture medium for 24h. Cytotoxicity was determined by adding 10μl CCK-8 reagent per well for 1 h at 37°C in 5% CO_2. The absorbance of the treated samples against a blank control was measured at 450 nm as the detection wavelength. The viability of treated cells was determined by comparing to the untreated ones in the control group. Alexa Fluor 488 Annexin V/Dead Cell Apoptosis Kit (Thermo Fisher Scientific) was used to measure cell apoptosis 4h following PDT according to the manufacturer's instructions. Cells were seeded at a density of 5×10^5 cells in 6-cm dishes and incubated for 24h. Cells were collected and incubated with 5μl of the annexin V conjugate and 1μl of the PI working solution at room temperature for 15 minutes. Intracellular ROS production was measured 1h following PDT treatment using DCFH-DA (Sigma-Aldrich). Briefly, 10 μM DCFH-DA diluted with PBS were added to cells at 37°C for 20 min. Cells were

then washed with PBS three times. Labeled cells were trypsinized and analyzed by flow cytometry. The cells were analyzed on the BD FACS Calibur flow cytometer and BD Accuri C6 Software (Becton-Dickinson, USA).

4.2.6 Assay of lipid-GVs' biodistribution in vivo

All procedures using laboratory animals were approved by the Department of Health, The Government of the Hong Kong Special Administrative Region and the Hong Kong Polytechnic University Animal Subjects Ethics Sub-committee. Female athymic nude mice weighing 16-18 g were supplied by the Animal Resource Centre of The University of Hong Kong. The mice were acclimated to the room for one week after arrival and were maintained on a normal 12 h light-dark cycle. The mice were housed in conventional cages (6 animal/cage) with free access to standard pellet diet and water in specific pathogen-free condition with 24±2°C temperature, 60-70% relative humidity. Standard wood chips for mice were used as bedding material. After 1 week's acclamation, 4×10^6 squamous cell carcinoma cell line (SCC7) in PBS (80µl) were injected into the rear dorsal of nude mice by subcutaneous injection. Tumor formation occurred approximately two weeks after cell implantation and we began imaging and therapy when tumor volume reached around 300 mm^3.

Mice were randomized into three groups: (a) PBS, (b) Free ICG solution, (c) ICG-labeled lipid-GVs. The respective solutions were injected into the tail veins of mice. Fluorescence images were acquired at 0, 5 min, 30 min, 1 h, 2 h after injection using

IVIS Lumina II (Caliper Life Sciences, USA; Excitation Filter: 780 nm, Emission Filter: 800 nm). Tumors and normal organs (heart, liver, spleen, lung, and kidney) were collected at different timepoints after injection, and the fluorescent signal intensities of these organs were determined.

4.2.7 In vivo oxygen delivery and PDT assay.

For tumor oxygenation detection, the oxy- and deoxy-Hb levels in subcutaneous tumors were monitored through photoacoustic imaging using Vevo LAZR photoacoustic imager (Fujifilm Visual sonics, Amsterdam, the Netherlands) featuring a hybrid US transducer (central f = 21 MHz; spatial resolution = 75μm). For experimental group, 200μl 5nM lipid-GVs(O_2) were injected through tail vein, while mice with the injection of 200μl PBS(O_2) were used as control groups. Oxygen saturation of the tumors was measured before, during and after GVs treatment for 25min. sO_2 levels were recorded and stored for later comparison between groups.

The effect of lipid-GVs(O_2) on PDT efficiency was evaluated on tumor-bearing mice models. ALA was administrated at the dose of 60mg/kg through pure topical injection around the tumor 4h before PDT treatment. The mice were randomly subdivided into five groups, including (1) control, (2) lipid-GVs(O_2) alone, (2) PDT, (3) PDT+ PBS(O_2), (4) PDT+ lipid-GVs(O_2). For the laser irradiation group, tumors were exposed to laser with a wavelength of 630nm (deeper penetration than 405nm) with the power of 100 mW/cm^2 for 20 min. The tumor size and bodyweight of each mouse were

measured every 3 days following the treatment. The subcutaneous tumor volume was estimated by the following formula: Tumor volume ≈ largest diameter × smallest diameter^2/2. All mice were sacrificed on day 15 and tumor tissues were collected and fixed in 4% paraformaldehyde for 24h, processed through conventional histological techniques and stained with hematoxylin and eosin (H&E). Images were captured by a Nikon optical microscope (Tokyo, Japan) and analysed using Nikon NIS-Elements software. For assessment of apoptosis in tumor sections, terminal deoxynucleotidyltransferase-mediated dUTP nick end labeling (TUNEL) was also carried out with an in situ Cell Death Detection Kit (Roche) following the manufacturer's protocol. Images were captured using a Nikon fluorescence microscope (Tokyo, Japan) and analyzed with Nikon NIS-Elements software.

4.2.8 In vitro and in vivo toxicity determination.

For *in vitro* toxicity determination, two kinds of GVs (with final concentration 1nM) were added into the cell culture media for different time point: 24h, 48h, and 72h. After that, LDH assay was determined using the Pierce LDH Cytotoxicity Assay Kit (Thermo Fisher Scientific, MA, USA) according to the manufacturer's instructions. Cell viability and Cell Apoptosis was were also determined by MTT assay (Thermo Fisher Scientific, MA, USA) and Alexa Fluor 488 Annexin V/Dead Cell Apoptosis Kit (Thermo Fisher Scientific) respectively according to the manufacturer's instructions. For *in vivo* toxicity determination, the body weight, food intake, and daily activity were

observed before and after the experiments according to the handbook of health evaluation of experimental laboratory mice[51, 129]. Post-mortem exams were also performed in mice and tissue samples (liver, lungs, and kidneys) were collected for histology. The liver, lung, and kidney samples collected from the mouse were also fixed in 4% Paraformaldehyde solution, processed with H&E staining as mentioned before.

4.2.9 Statistical analyses.

Statistical analysis was performed with GraphPad Prism software. ImageJ, Photoshop CS and Illustrator CS software were used for image processing according to the general guidelines. Triplicate data were analyzed. Comparisons between two groups were made by Student's two-tailed t-test, and comparisons between more than two groups were made by one-way ANOVA followed by Bonferroni test. All data expressed as means ± SD. P-values <0.05 were considered statistically significant. Asterisks are used to indicate the significant differences.

4.3 Results and discussion

4.3.1 Fabrication and Characterization of lipid-GVs

GVs for our study were produced by culturing the algae *Anabaena flos-aquae*, and isolating GVs through centrifugation. Since the shells of GVs are permeable to gas molecules, their oxygen delivery efficiency could be affected. Hence, we prepared GVs with surface modification using lipids (lipid-GVs) to reduce gas exchange[130, 131] (Fig.4.2). Native and lipid-GVs showed no major visible differences when in solution (Fig.4.3A) or in the morphology of individual vesicles as observed by TEM (Fig. 4.3B). The lipid-GVs were next characterized for particle size distribution and zeta potential. These nanobubble formulations were found to have a mean diameter of approximately 300-330 nm and a uniform distribution (Figs. 4.3C-D). The average diameters of lipid-GVs were ~10 nm larger than native GVs, with a lower negative charge (Fig. 4.3E). The zeta potential of nanoparticles is closely associated with the stability of colloidal dispersions. Colloids with higher zeta potential (negative or positive, higher than 30) are electrically stabilized while colloids with lower zeta potential tend to coagulate easily[81]. The zeta potential of both GVs and lipid-GVs was found to be high enough to resist aggregation. We also evaluated the stability of the GVs in cold storage (4°C). The concentration (determined by OD_{500}) and size of the two groups were observed from zero to six months and no significant changes were found in either group (Figs. 4.3F-G). We finally determined GV groups' stability in acidic PBS (pH 6) and FBS

respectively. GVs/lipid-GVs (final concentration =1 nM) were added to acidic PBS or FBS and incubated for 3 and 7 days respectively. Over this period the concentration of all GV groups was found to decrease slightly but their concentrations always remained above 80% of the original (Fig. 4.3H). Thus, we were able to produce nanoscale, negatively charged GVs that were stable in solution through long-term storage.

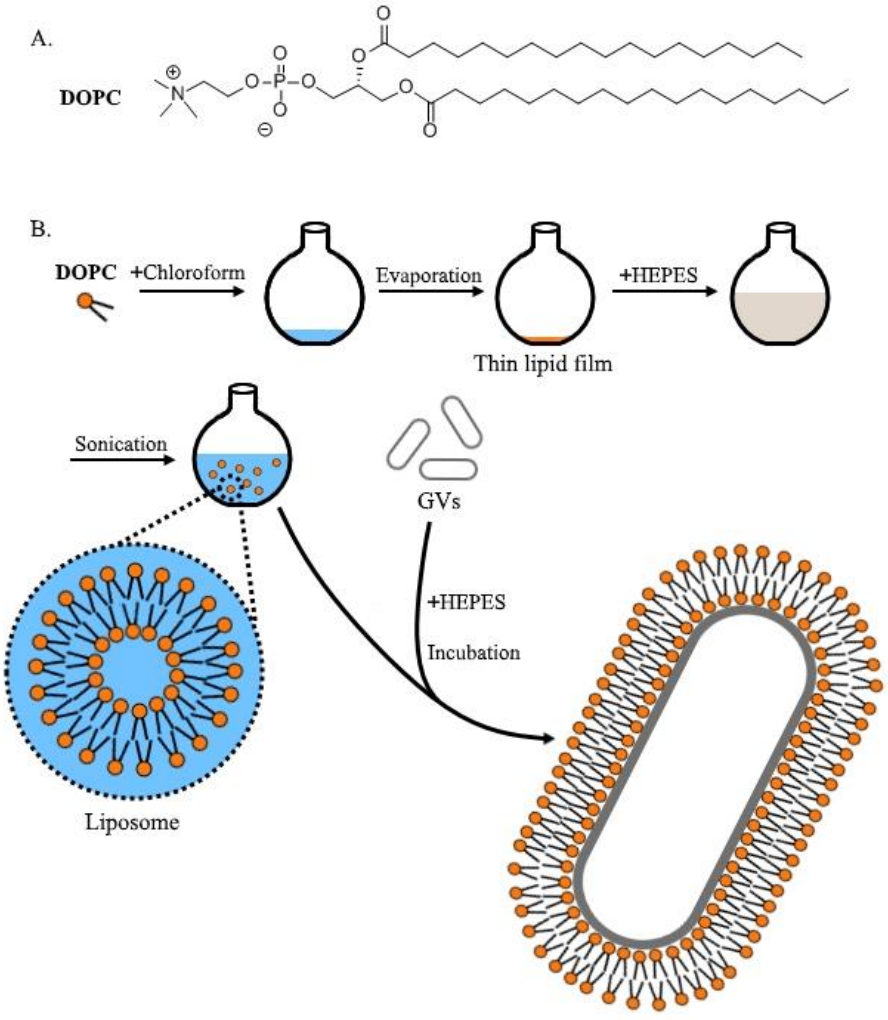

Figure 4.2 (A) Molecular structure of DOPC. (B) Schematic overview of the preparation of lipid-GVs.

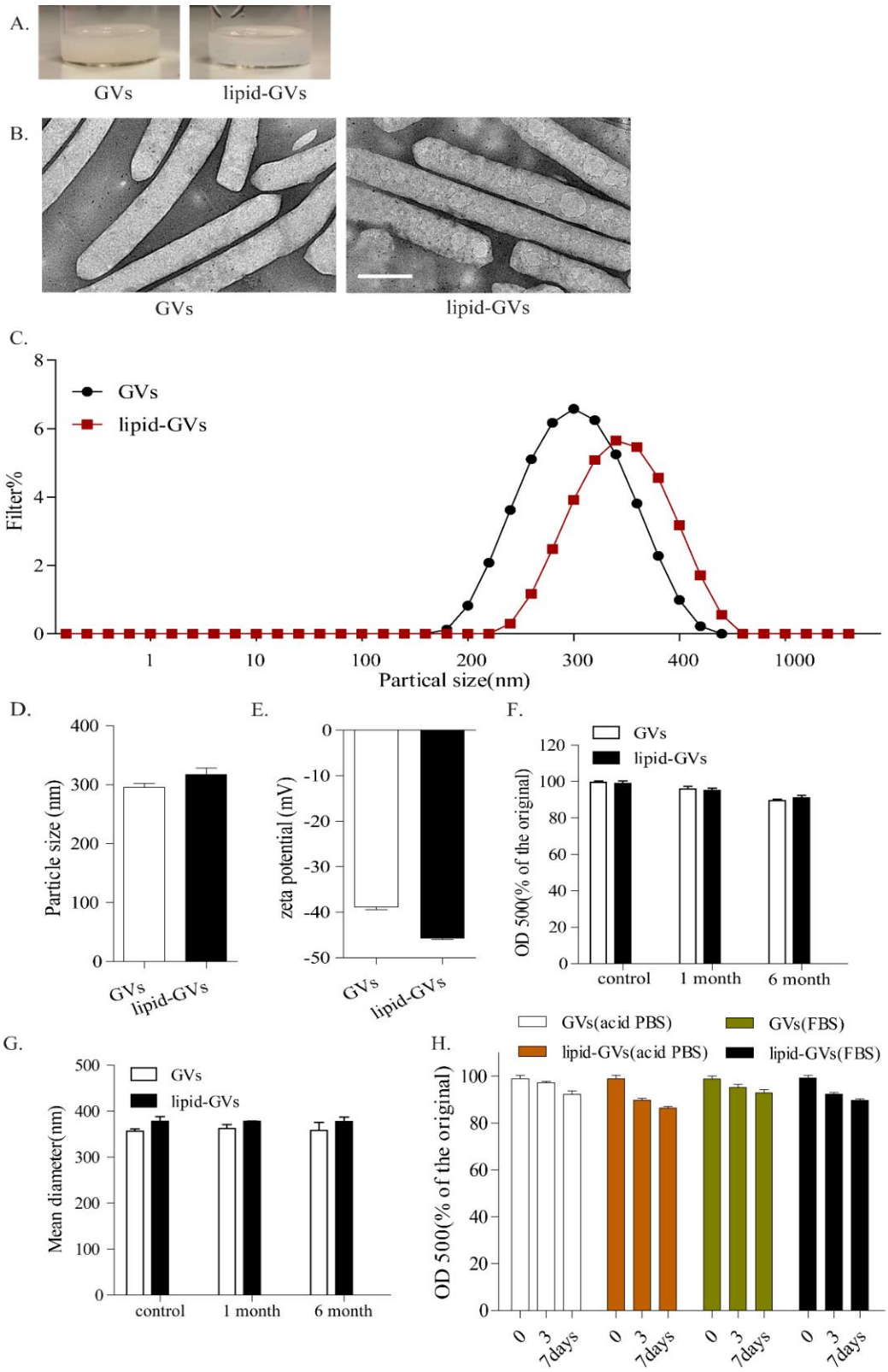

Figure 4.3 Morphology, size distribution, and zeta potential of native GVs and lipid-GVs. (A) Photographic images of 1nM GVs and lipid-GVs in solution. (B) The TEM image of GVs, showing their morphology (images are representative). Scale bar represents 100nm. (C) Histogram showing

the relative size distributions of the two GV groups with the statistics shown in (D). (E) Zeta potential statistics of two GV groups. (F) GV groups' stability over 6 months observed by measuring their concentration. (G) GV groups' stability over 6 months observed by measuring their size. Data in (D) - (G) represent the mean ± SD from 3 independent experiments. (H) GV groups' stability in acidic PBS (pH 6) and neutral FBS was determined by measuring their concentration. Data represent the mean ± SD from 3 independent experiments.

4.3.2 Determination of oxygen release kinetics of lipid-GVs

We next tested the oxygen release kinetics of the groups by their abilities to raise oxygen concentrations in hypoxic solutions. We found that lipid-GVs(O_2) could increase the oxygen concentration of severely hypoxic solutions significantly compared to oxygen-filled PBS (Figure 4.4). Compared to native GVs(O_2), lipid-GVs(O_2) showed a significantly greater ability to elevate the solution's oxygen concentration. The release of oxygen by lipid-GVs(O_2) into solution was also slower than native GVs(O_2). We attribute this to the surface modification of GVs leading to slower oxygen release kinetics. Moreover, the ability of GVs to release oxygen was found to be concentration-dependent, with a higher concentration displaying greater ability to raise oxygen concentration of hypoxic solutions. Thus, compared to native GVs, lipid-GVs showed slower release patterns and were able to increase the oxygen concentration to a greater degree.

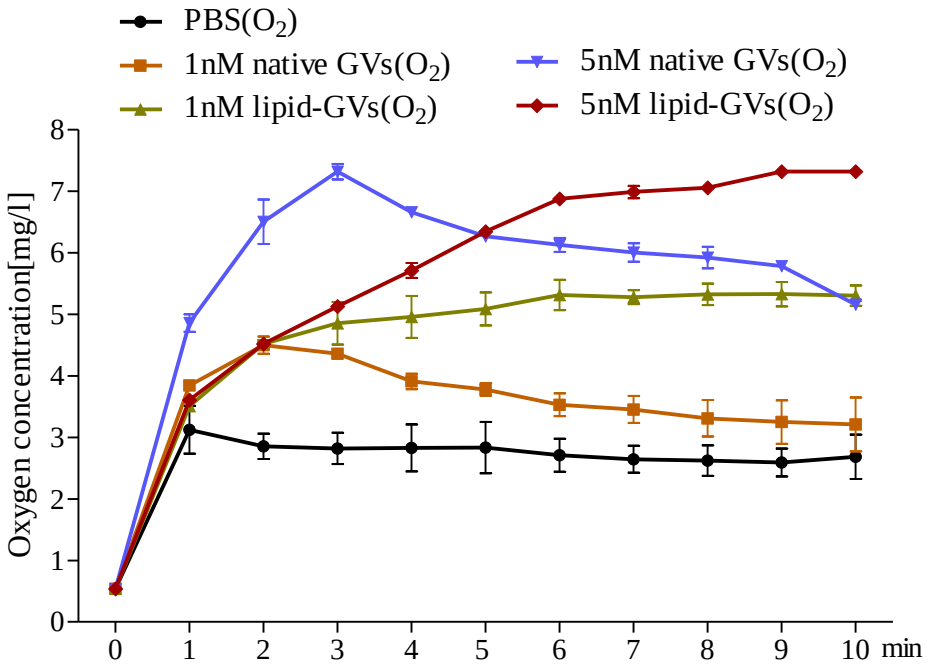

Figure 4.4 Determination of oxygen release kinetics of GVs. The oxygen concentration in 5ml severe hypoxic solution after injection of 1ml of GVs(+O2)/ lipid-GVs(+O2). Data represent the mean ± SD based on 3 independent experiments. *p < 0.05 vs. control. **p < 0.01 vs. control.

4.3.3 In vitro oxygen delivery detection and PDT assay

We next evaluated lipid-GVs' abilities to modify the hypoxic conditions of cells *in vitro*. Human hepatoma cells (HepG2 cell line) were grown in hypoxic conditions overnight and levels of hypoxia were monitored using Image-iT Red Hypoxia Reagent. Compared to the untreated control and PBS(O_2), the addition of lipid-GVs(O_2) significantly reduced the observed levels of hypoxia (Figs. 4.5A-B). We next tested whether lipid-GVs(O_2) could increase the efficacy of PDT under hypoxic conditions. A schematic illustration of our PDT setup is shown in Figure 4.5C. The impact of adding lipid-GVs(O_2) on the cytotoxicity of ALA-PDT, in hypoxic HepG2 cells was

determined using a CCK-8 assay, 4 hours after PDT treatment. PDT alone decreased cell viability of HepG2 cells to 85%, while the addition of lipid-GVs(O_2) significantly decreased cell viability following PDT to 50% (Fig. 4.5D). We also investigated the effects of lipid-GVs(O_2) on PDT induced cell apoptosis by flow cytometry for PI/Annexin V. Consistent with the aforementioned results, the addition of lipid-GVs(O_2) increased the rate of necrosis and apoptosis among cells by nearly 20% following PDT compared to the PBS(O_2) group (Fig. 4.5E). Crucially, lipid-GVs(O_2) alone had no effect on cell viability and apoptosis. These data demonstrate that the addition of lipid-GVs(O_2) could lead to significantly higher cell death and apoptosis levels of cancer cells following PDT. Excessive production of ROS is believed to be the mechanism responsible for the cytotoxicity of tumor cells during PDT. Hence, we further investigated whether the addition of lipid-GVs(O_2) increased the production of intracellular ROS following PDT. As expected, excessive ROS production was detected 1 hour following PDT in all three PDT treatment groups, but total intracellular ROS was most significantly increased with the addition of lipid-GVs(O_2) (Figs. 4.5F-G).

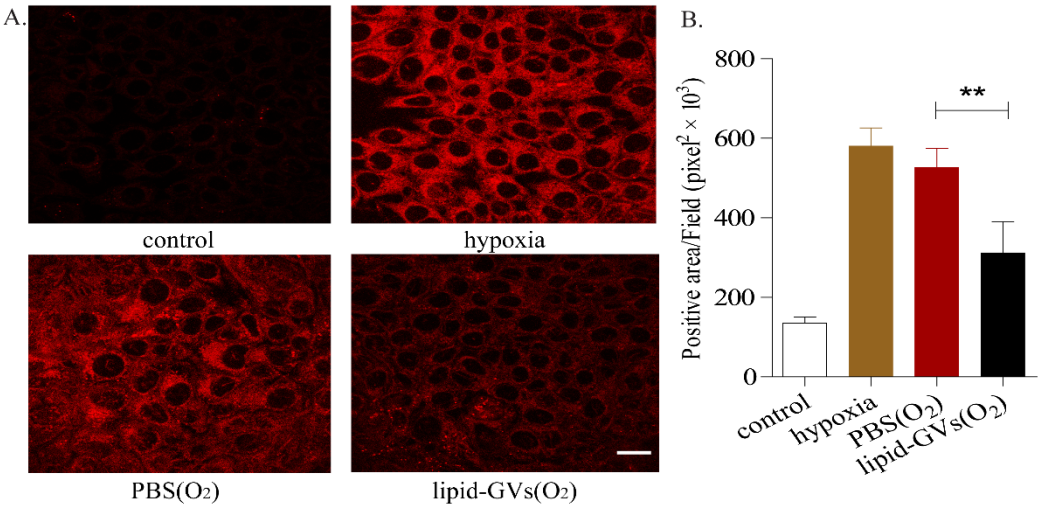
A.
control
hypoxia
PBS(O2)
lipid-GVs(O2)
B.
Positive area/Field (pixel2 × 10³)
800
600
400
200
0
**
control
hypoxia
PBS(O2)
lipid-GVs(O2)

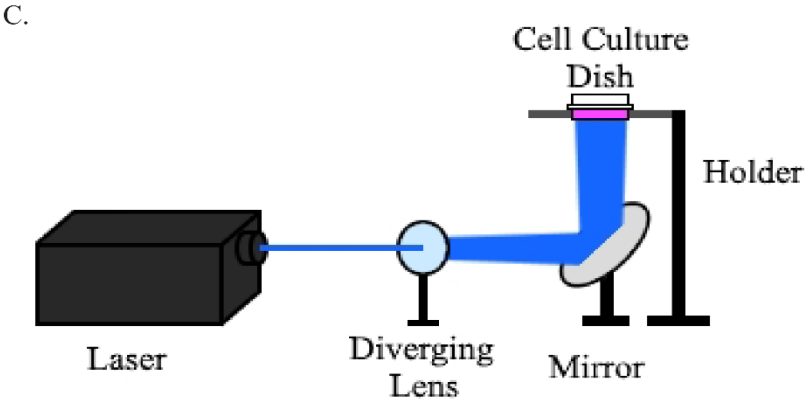
C.
Cell Culture Dish
Holder
Laser
Diverging Lens
Mirror

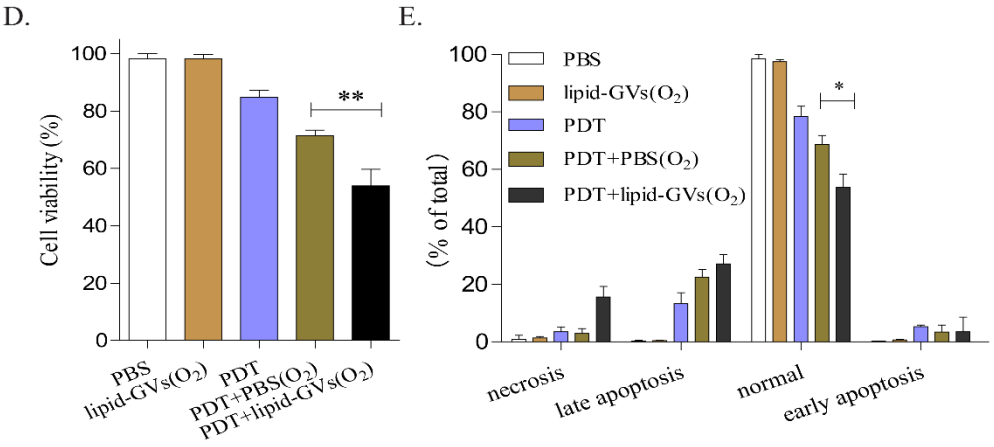
D.
Cell viability (%)
100
80
60
40
20
0
**
PBS
lipid-GVs(O2)
PDT
PDT+PBS(O2)
PDT+lipid-GVs(O2)
E.
(% of total)
PBS
lipid-GVs(O2)
PDT
PDT+PBS(O2)
PDT+lipid-GVs(O2)
*
necrosis
late apoptosis
normal
early apoptosis

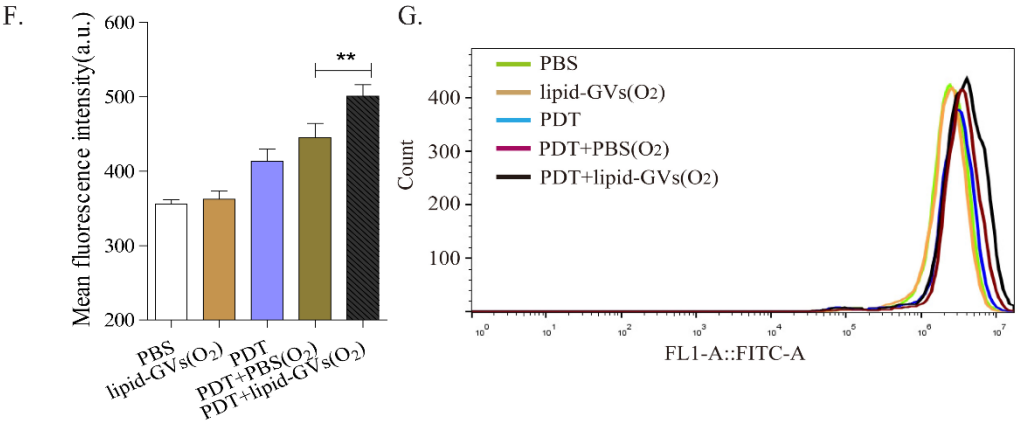
F.
Mean fluorescence intensity(a.u.)
600
500
400
300
200
**
PBS
lipid-GVs(O2)
PDT
PDT+PBS(O2)
PDT+lipid-GVs(O2)
G.
Count
400
300
200
100
PBS
lipid-GVs(O2)
PDT
PDT+PBS(O2)
PDT+lipid-GVs(O2)
FL1-A::FITC-A

Figure 4.5 Lipid-GVs(O_2) mediated oxygen delivery and PDT under hypoxia *in vitro*. (A) 200μl PBS(O_2) or lipid-GVs(O_2) (with final concentration 1nM) was added into medium and cultured with cells in hypoxic condition for 1 hour. Image-iT Red Hypoxia Reagent was used to detect hypoxia in cultured cells, indicated by red fluorescence. Representative images are shown in (A) with quantification of hypoxic staining shown in (B). Data represent the mean ± SD from on 3 independent experiments. **$p < 0.01$ vs. control. Scale bar represents 25μm. (C) Schematic diagram of PDT setup. (D) Relative cell viability of HepG2 cells after different treatments by CCK-8 assay. Data represent mean ± SD of 3 independent experiments. **$p < 0.01$ vs. PBS. (E) Evaluation of cell apoptosis following different treatments by flow cytometry through Annexin-V and propidium iodide (PI) double staining. Data represent the mean ± SD based on 3 independent experiments. *$p < 0.05$ vs. PBS. (F) Intracellular ROS generation stained with DCFHDA and analyzed by flow cytometry following different treatments. The values are the mean ± SD of three independent experiments. **$p < 0.01$ vs. pbs. Overlapping image of five groups is shown in (G).

4.3.4 In vivo biodistribution and tumor accumulation of lipid-GVs.

To monitor the biodistribution of the lipid-GVs *in vivo*, we labeled lipid-GVs with indocyanine green (ICG), a near infra-red (NIR) fluorophore. ICG-labeled lipid-GVs showed an absorption peak around 800nm, indicating the successful incorporation of ICG into lipid-GVs (Figure 4.6A). Fluorescent imaging of both ICG and ICG-labeled lipid-GVs showed strong fluorescence, indicating the incorporation of ICG into lipid-GVs had minimal effects on ICG's fluorescent properties (Figure 4.6B). For *in vivo* real-time NIRF imaging, tumor-bearing nude mice were monitored for 2 hours after systemic administration of 200 μl PBS, free ICG (20 μg) and 5 nM ICG-labeled lipid-GVs (containing 20 μg ICG) respectively. Both free ICG and ICG-labelled lipid-GVs

showed significant fluorescence in the vital organs (liver, lungs, spleen, etc.) within one hour and decreased over time (Figure 4.6C). The ICG signal in the tumor peaked at half an hour after injection, indicating rapid tumor clearance, whereas the tumor fluorescence in the ICG-labelled lipid-GVs group was detectable from 5 min to 2 h after injection (Figures 4.6D and F). Closer examination of the fluorescence signals from major organs of both groups showed high fluorescence intensity occurred mainly in the liver and kidney within two hours and decreased over time (Figures 4.6E, G and H).Thus, lipid-GVs were able to be retained in tumors for at least 2 hours post-injection, which would be a long enough period for oxygen delivery.

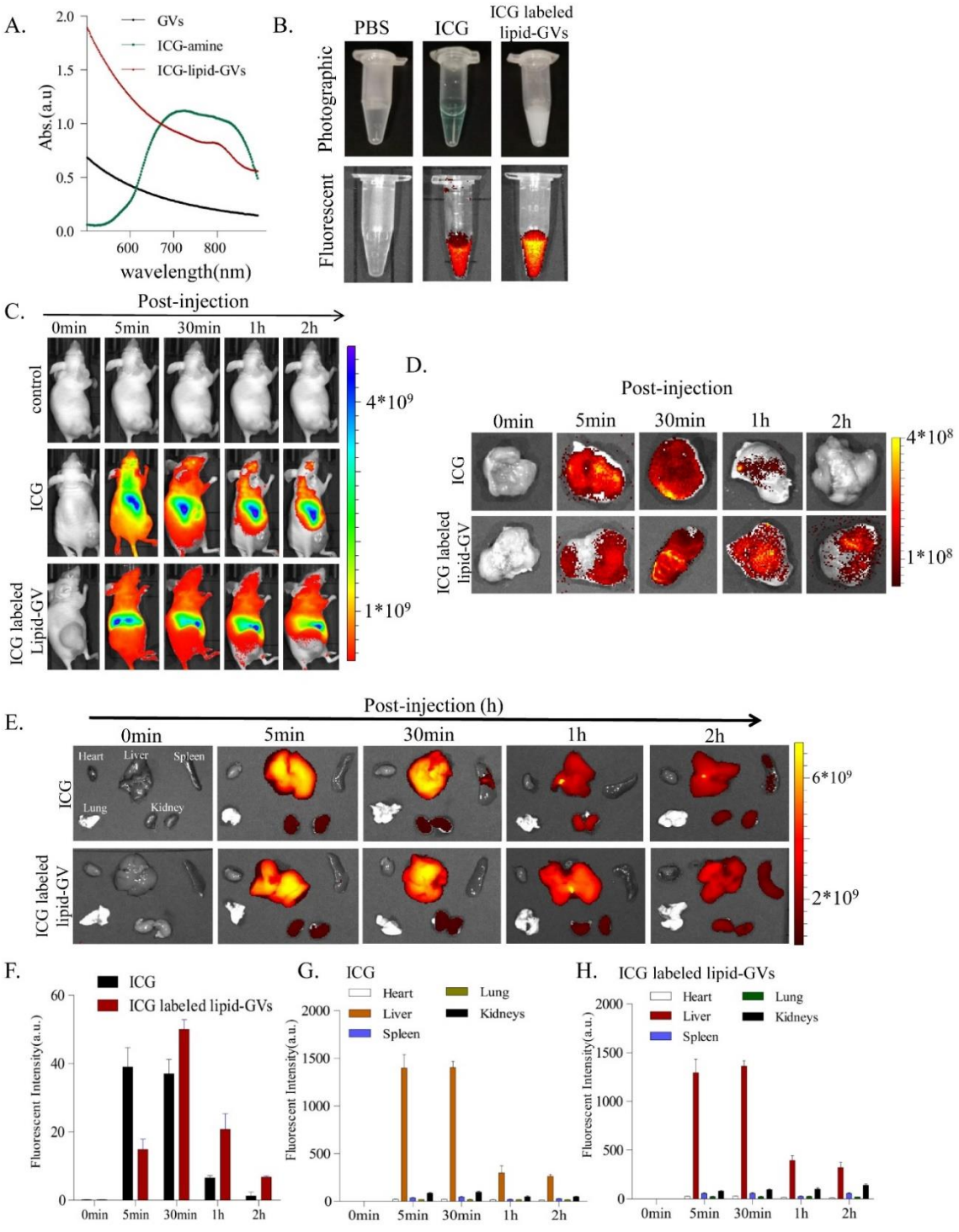

Figure 4.6 *In vivo* biodistribution of ICG labeled lipid-GVs. (A) Absorbance spectra of native GVs, ICG, ICG labeled lipid-GVs in phosphate buffered saline (PBS). (B) Photographic and fluorescent images of ICG and ICG labeled lipid-GVs (Ex. 780 nm, Em. 845 nm). (C) *In vivo* NIR

fluorescent imaging of tumor-bearing nude mice at different time after intravenous injection of free ICG and ICG labeled lipid-GVs respectively. *Ex vivo* fluorescence imaging of tumors and vital organs from tumor-bearing nude mice after different timepoints post-injection of ICG and ICG-labeled lipid-GVs respectively. Representative images were shown in (D) and (E) respectively. Quantitative analysis is shown in (F), (G) and (H) respectively. Data represent the mean ± SD (n = 4).

4.3.5 In vivo oxygen delivery detection and PDT assay of lipid-GVs.

Lipid-GVs' abilities to modify the hypoxic conditions of tumor masses *in vivo* were evaluated. An *in vivo* proof-of-concept experiment was also performed to determine the ability of lipid-GVs(O_2) to elevate hypoxic subcutaneous tumor oxygenation levels in nude mice. Tumor oxygenation was monitored by visualizing the levels of oxy-Hemoglobin (oxy-Hb) and deoxy-Hemoglobin (deoxy-Hb) through photoacoustic imaging before and after the treatment (0, 5, 15, and 25 minutes). Tail-vein injection of lipid-GVs(O_2) resulted in elevated sO_2 in the tumors and sO_2 peaked 15 minutes following injection and then decreased gradually, but not with the PBS(O_2) controls (Fig. 4.7A-B). Thus, we found that the lipid-GVs filled with O_2 were successfully able to raise oxygen levels in subcutaneous tumors.

The effects of lipid-GVs(O_2) on ALA-mediated PDT *in vivo* was then evaluated. Treatments were begun when subcutaneous tumor volume reached 300mm^3. 200μl lipid-GVs(O_2) were intravenous injected into mice 15 minutes before laser irradiation. Tumor volumes and body weight were measured every three days after various

treatments. Rapid and continuous growth of tumor was observed in both control group and lipid-GVs(O_2) alone group for the following 15 days with the volume of tumors reaching nearly 1500mm^3 at the end of the experiments on the 15th day (Fig. 4.7C). For PDT treatment groups, all three groups exhibited effective tumor growth inhibition efficacy compared to control group and lipid-GVs(O_2) alone group. Tumors were found to shrink significantly in the early three days following PDT treatment and to regrow slowly by the end of test period. However, even compared to all the groups with PDT, lipid-GVs(O_2) showed significantly greater tumor growth inhibition, being the lowest of all five tested groups. Crucially, PDT plus PBS(O_2) treatment showed negligible effects compared to PDT alone, again indicating the important ability of lipid-GVs to successfully carry *and* to deliver O_2 to the tumor site. The body weights of mice were also recorded during the experiments to assess the systematic toxicity of the treatment, and no significant change was detected among the five groups (Figure 4.7D). However, a gradual increase in body weight was seen in the control group and lipid-GVs(O_2) alone group, which may have been caused by rapid tumor growth. To further confirm the role of lipid-GVs(O_2) in improving the therapeutic efficacy of PDT, H&E staining and TUNEL assay of tumor slices were obtained. Compared to control group and lipid-GVs(O_2) alone group, which showed normal morphology, H&E staining in PDT, PDT +PBS(O_2) and PDT+lipid-GVs(O_2) groups revealed severe damage, with PDT+lipid-GVs(O_2) group showing the most significant toxicity effects (Figure 4.7E). Similarly, a TUNEL assay revealed much higher levels of apoptosis in PDT+lipid-GVs(O_2) than

in the PDT and PDT+PBS(O_2) groups, with almost no apoptosis in control and lipid-GVs(O_2) alone groups (Figure 4.7F). Taken together, these results demonstrate the efficacy of lipid-GVs(O_2) to enhance PDT outcomes. These data also highlight that while PDT+PBS(O_2) showed some effects *in vitro*, it much less effective than PDT+lipid-GVs(O_2) *in vivo*, emphasizing lipid-GVs' capability to successfully deliver O_2 to the tumor site after systemic injection.

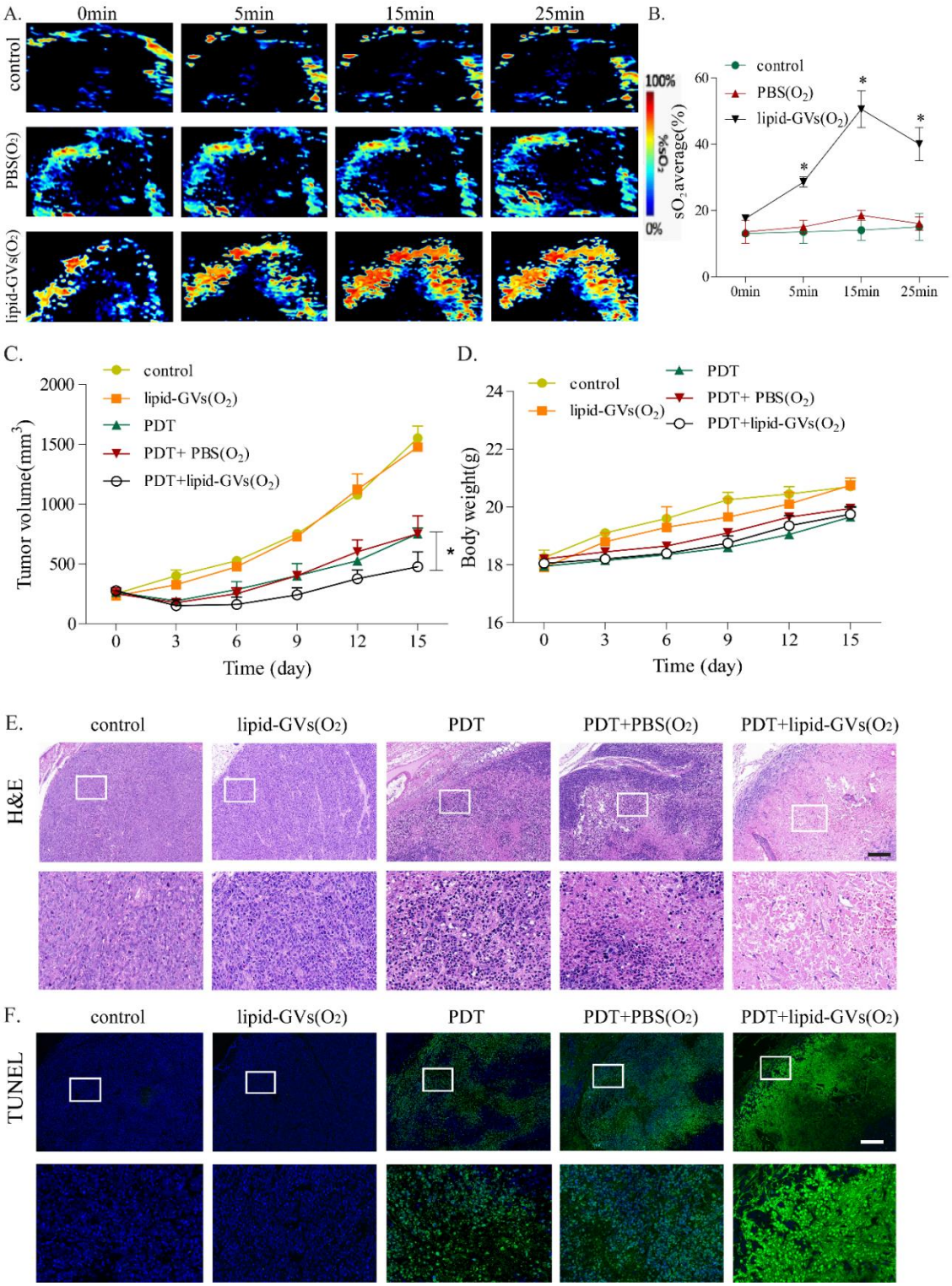

Figure 4.7 Lipid-GVs(O_2) mediated oxygen delivery and PDT in vivo. (A) Representative photoacoustic images of tumor oxygen levels (Oxy-Hb and deoxy-Hb levels) from in vivo tumor-bearing mice at different time points by tail vein injection of 200μl of saline, PBS(O_2), and 5nM lipid-GVs(O_2). Red pixels: oxy-Hb; blue pixels: deoxy-Hb. (B) Quantification of tumor oxygen

levels. Data represent the mean ± SD based on 4 independent experiments. *p < 0.05 vs. control. (C) Effects of lipid-GVs(O_2) on *in vivo* PDT were determined. Tumor growth curves of SCC7 tumor-bearing mice with different treatment groups. n = 5 mice per group, *p < 0.05 significance level. (D) Body weight of SCC7 tumor-bearing mice after various treatments. (E) Representative histological images of H&E stained tumor slices collected from different groups. Scale bar represents 200 μm. (F) Representative images of TUNEL assay of tumor slices collected from different groups. Scale bar represents 200 μm.

4.3.6 In vitro and in vivo toxicity detection.

Finally, we tested the toxicity and biosafety of both GVs and lipid-GVs. We used the LDH, MTT and apoptosis assays *in vitro* for this purpose and found that both GVs and lipid-GVs triggered no cytotoxicity on cells. GVs/lipid-GVs (final concentration=1 nM) were added to the culture medium and incubate for 24, 48 or 72 hours. No significant elevation in LDH, formazan levels, Annexin V or PI signal was observed at any time point, compared to the control (Figs. 4.8A-C). We next tested the biosafety of GVs/lipid-GVs *in vivo* by observing three basic measures of mouse health (activity, weight and food intake) before the administration of GVs/lipid-GVs, and 24, 48 and 72 hours after administration of GVs/Lipid-GVs. Scoring the mice on a 30-point scale, we observed no decrease in these indicators over the time period (Fig. 4.8D). We also assayed the mice's major organs (heart, liver, spleen, lungs, and kidneys) one week after GVs/lipid-GVs' administration using hematoxylin and eosin (H&E) staining (Fig. 4.8E). Tissue slices from both GVs' and lipid-GVs' groups presented no significant pathological abnormalities or lesions compared to the control group. We thus

determined that both GVs and lipid-GVs alone were not cytotoxic to cells and did not cause any significant damage to the mice in which they were tested.

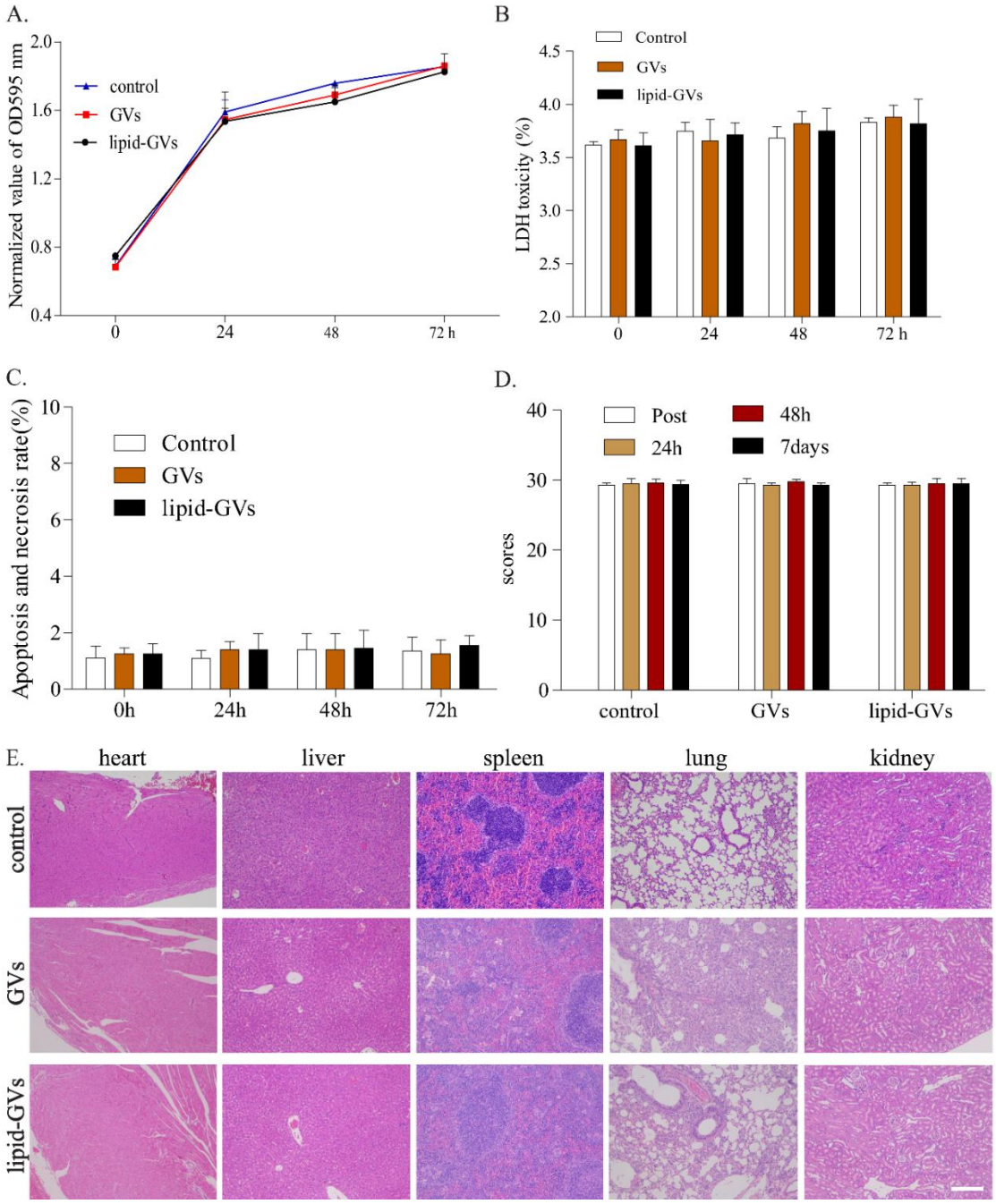

Figure 4.8. Toxicity of GVs/ lipid-GVs both *in vitro* and *in vivo*. (A-B) 200 µl GVs/ lipid-GVs (final concentration 1 nM) were added into media the media incubated with HepG2 cells for multiple days. Cell proliferation and LDH toxicity of HepG2 cells were measured by MTT and LDH

assay at the time points indicated. Data represent the mean ± SD based on 3 independent experiments. (C) Apoptosis in HepG2 cells were measured by Annexin V and PI assay at the various time points indicated. Data represent the mean ± SD based on 3 independent experiments. (D) The overall scores of mice indicating their observed health condition. Mice were scored on a 30-point scale comprising 10 points each for activity, weight, food intake. The assessment was performed before, immediately after, 24 hours, 48 hours and one week after injection (N =5, ±SD). (E) Histological images of major organs with H&E staining collected from mice treated with GVs/ lipid-GVs on day 7. Scale bar represents 100μm.

4.4 Conclusion

In the present study, we present a novel use of gas vesicles as promising oxygen nanocarrier to alleviate tumor hypoxia. As a type of physically stable nanostructure, GVs kept very well in long-term storage in cooling conditions. Preliminary in *vitro* results showed lipid-GVs(O_2) could change the hypoxic condition of cell culture when added to the medium. This indicates that lipid-GVs can carry enough oxygen to significantly affect cell culture. Biodistribution of GVs after tail injection of immunodeficient (SCID) nude mice determined by *Shapiro et al* showed that native GVs begin to accumulate in the liver after approximately 50 seconds and will be degraded by the liver like other protein nanostructures within 60min[51]. Our preliminary in *vivo* results also showed the ability of lipid-GVs(O_2) to elevate oxygenation levels in hypoxic tumors *in vivo* 5min after tail injection, indicating that the GVs were both stable enough to survive the circulation to the tumor site and that they were able to deliver a significant amount of oxygen. This demonstrated that such surface engineering could be a good way to elevate the *in vivo* efficiency of this method by improving and optimizing the rate of oxygen release by lipid-GVs. The results of PDT assay both in *vitro* and in *vivo* showed that the addition of lipid-GVs(O_2) could enhance the photodynamic effect in hypoxic environments. Toxicity studies both in *vitro* and in *vivo* showed GVs to be well tolerated. Compared to other organic or inorganic materials that could lead to certain levels of adverse effects, the initial

biocompatibility of GVs was seen to be good and safe for mice. The observed long-term storage in cooling conditions, good oxygen-loading and release capabilities, and no acute toxicities makes GVs unique among other oxygen carriers. Thus, our approach provided a new choice for oxygen delivery to tumor sites for PDT as well as other oxygen-consuming tumor therapies.

CHAPTER 5 Conclusions and future work

In the above studies, we have focused on the interface between GVs and focused ultrasound and described the application of GVs on ultrasound molecular imaging and tumor therapy. As a nanosized contrast agent, GVs are very special compared with other synthesized nanobubbles. Not only due to their innate stability which makes them long-time stable gas bubbles but also because of their gene editability. GVs are biogenic structures that are encoded by 8-14 genes which include the structural protein GvpA, the external protein GvpC and several secondary proteins. For one side, genetic encodability makes it possible to change GVs at gene level as well as protein level. On the other side, gas vesicle gene clusters could be expressed in mammalian cells which pave the way for broader application of GVs such as serving as ultrasound reporter genes. All these properties confer GVs a unique role in the further application for cancer therapy.

As a kind of gas bubble, GVs are good contrast agents for ultrasound imaging. However, their application was limited when they were intravenously injected in mice for that they would be quickly cleared by the reticuloendothelial system *in vivo*. Thus, in our study, in order to explore GVs' application in ultrasound imaging and tumor therapy, our first aim is to confer GVs the ability to escape the clearance from RES and to target and accumulate smoothly in the tumor site. Our study confirmed that our GVs showed good biocompatibility and ability to escape RES uptake in *vivo* after surface

modification. Besides, PH-GVs have prolonged blood circulation and could selectively accumulate at the tumor site which showed the improved tumor targeting effects of PH-GVs. More importantly, PH-GVs showed good ultrasound imaging properties in the tumor site. All these improvements make GVs to truly fulfill their potential as a high-performance nanoscale molecular reporter for ultrasound imaging for CD44-positive tumor therapy.

Since GVs could accumulate in the tumor site, we further explored their application in tumor therapy. we detected the role of GVs based nanoplatform for enhanced sonodynamic therapy of cancer cells. The results showed GVs could facilitate the nucleation of cavitation as well as enhance the production of ROS during SDT. The effects of GVs to increase the inhibition effects of SDT on tumor growth were also demonstrated. Thus, GVs could function as both imaging and therapeutic agents for imaging-guided targeted cancer therapy.

Efforts were also made to develop gas vesicles as oxygen nanocarrier to alleviate tumor hypoxia. Lipid-GVs were made and the ability of lipid-GVs(O_2) to elevate oxygenation levels in tumors *in vivo* was demonstrated. The amount of oxygen that lipid-GVs(O_2) carried were large enough to enhance the toxicity of PDT assay both in *vitro* and in *vivo.* Thus, the ability of GVs to serve as imaging as well as therapeutic agents makes GVs huge potential in theranostics in which ultrasound could be used to guide and control the therapy activity.

Toxicity studies both in *vitro* and in *vivo* also showed GVs to be well tolerated.

Compared to other organic or inorganic materials that could lead to certain levels of adverse effects, the initial biocompatibility of GVs was seen to be good and safe for mice. However, further work is still needed to confirm whether they could induce allergic or immunologic reactions during repeat transfusions or whether they could induce potential long term immunotoxicity. Crucially, even where any of these to emerge as issues in further testing, the possibility of alleviating or eliminating these effects through surface modification would give GVs an even greater chance of being successful.

Further study will focus on the combination of GVs' imaging and therapy. Besides being mere oxygen carriers, the shells of GVs are readily linkable with various anti-tumor drugs, GVs have the potential to be an effective carrier for both oxygen and drug delivery into tumor sites with potentially long circulation time and high efficacy. Furthermore, development of GVs with higher resolution for molecular ultrasound imaging is also an important target. Thus, GVs is a versatile entity that could be used to combine multiple aspects of cancer therapy, potentially achieving the aim of ultrasound-guided oxygen delivery and therapy. Such approaches could help to pave the way for the era of better-targeted cancer therapies with reduced side-effects and greater efficacies.

FIGURE REFERENCES

References

[1] S. McGuire, World cancer report 2014. Geneva, Switzerland: World Health Organization, international agency for research on cancer, WHO Press, 2015, Oxford University Press, 2016.

[2] R.L. Siegel, K.D. Miller, A. Jemal, Cancer statistics, 2019, CA Cancer J Clin 69(1) (2019) 7-34.

[3] R.L. Siegel, K.D. Miller, A. Jemal, Cancer Statistics, 2017, CA Cancer J Clin 67(1) (2017) 7-30.

[4] R.L. Siegel, K.D. Miller, A. Jemal, Cancer statistics, 2018, CA Cancer J Clin 68(1) (2018) 7-30.

[5] P. Gotwals, S. Cameron, D. Cipolletta, V. Cremasco, A. Crystal, B. Hewes, B. Mueller, S. Quaratino, C. Sabatos-Peyton, L. Petruzzelli, J.A. Engelman, G. Dranoff, Prospects for combining targeted and conventional cancer therapy with immunotherapy, Nat Rev Cancer 17(5) (2017) 286-301.

[6] K. Graham, E. Unger, Overcoming tumor hypoxia as a barrier to radiotherapy, chemotherapy and immunotherapy in cancer treatment, Int J Nanomedicine 13 (2018) 6049-6058.

[7] M.J. Lind, Principles of systemic anticancer therapy, Medicine 48(2) (2020) 90-96.

[8] D. Hanahan, R.A. Weinberg, Hallmarks of cancer: the next generation, Cell 144(5) (2011) 646-74.

[9] P. Vaupel, Tumor microenvironmental physiology and its implications for radiation oncology, Semin Radiat Oncol 14(3) (2004) 198-206.

[10] P. Vaupel, Hypoxia and aggressive tumor phenotype: implications for therapy and prognosis, Oncologist 13 Suppl 3 (2008) 21-6.

[11] D.F. Quail, J.A. Joyce, Microenvironmental regulation of tumor progression and metastasis, Nat Med 19(11) (2013) 1423-37.

[12] S.S. McAllister, R.A. Weinberg, The tumour-induced systemic environment as a critical regulator of cancer progression and metastasis, Nat Cell Biol 16(8) (2014) 717-27.

[13] S.R. Nielsen, M.C. Schmid, Macrophages as Key Drivers of Cancer Progression and Metastasis, Mediators Inflamm 2017 (2017) 9624760.

[14] H.A. Smith, Y. Kang, The metastasis-promoting roles of tumor-associated immune cells, J Mol Med (Berl) 91(4) (2013) 411-29.

[15] S. Guo, C.X. Deng, Effect of Stromal Cells in Tumor Microenvironment on Metastasis Initiation, Int J Biol Sci 14(14) (2018) 2083-2093.

[16] P. Agostinis, K. Berg, K.A. Cengel, T.H. Foster, A.W. Girotti, S.O. Gollnick, S.M. Hahn, M.R. Hamblin, A. Juzeniene, D. Kessel, M. Korbelik, J. Moan, P. Mroz, D. Nowis, J. Piette, B.C. Wilson, J. Golab, Photodynamic therapy of cancer: an update, CA Cancer J Clin 61(4) (2011) 250-81.

[17] R. Baskar, K.A. Lee, R. Yeo, K.W. Yeoh, Cancer and radiation therapy: current advances and future directions, Int J Med Sci 9(3) (2012) 193-9.

[18] D. Costley, C. Mc Ewan, C. Fowley, A.P. McHale, J. Atchison, N. Nomikou, J.F. Callan, Treating cancer with sonodynamic therapy: a review, Int J Hyperthermia 31(2) (2015) 107-17.

[19] S.V. Karakashev, M.J. Reginato, Progress toward overcoming hypoxia-induced resistance to solid tumor therapy, Cancer Manag Res 7 (2015) 253-64.

[20] K. Bruheim, M.G. Guren, E. Skovlund, M.J. Hjermstad, O. Dahl, G. Frykholm, E. Carlsen, K.M. Tveit, Late side effects and quality of life after radiotherapy for rectal cancer, International Journal of Radiation Oncology* Biology* Physics 76(4) (2010) 1005-1011.

[21] R.R. Love, H. Leventhal, D.V. Easterling, D.R. Nerenz, Side effects and emotional distress during cancer chemotherapy, Cancer 63(3) (1989) 604-612.

[22] T.G. Burish, J.N. Lyles, Effectiveness of relaxation training in reducing the aversiveness of chemotherapy in the treatment of cancer, Journal of Behavior Therapy and Experimental Psychiatry 10(4) (1979) 357-361.

[23] S. Golden, Cancer Chemotherapy and Management of patient problems, Nursing Forum 14(3) (1975) 279-304.

[24] Y. Cui, G. Guo, Immunomodulatory Function of the Tumor Suppressor p53 in Host Immune Response and the Tumor Microenvironment, Int J Mol Sci 17(11) (2016).

[25] A.G. Hugo, Photodynamic Therapy : Fundamentals, Applications and Health Outcomes, Nova Science Publishers, Incorporated, New York, UNITED STATES, 2015.

[26] P. Agostinis, K. Berg, K.A. Cengel, T.H. Foster, A.W. Girotti, S.O. Gollnick, S.M. Hahn, M.R. Hamblin, A. Juzeniene, D. Kessel, M. Korbelik, J. Moan, P. Mroz, D. Nowis, J. Piette, B.C. Wilson, J. Golab, Photodynamic therapy of cancer: An update, CA: A Cancer Journal for Clinicians 61(4) (2011) 250-281.

[27] D.E. Dolmans, A. Kadambi, J.S. Hill, C.A. Waters, B.C. Robinson, J.P. Walker, D. Fukumura, R.K. Jain, Vascular accumulation of a novel photosensitizer, MV6401, causes selective thrombosis in tumor vessels after photodynamic therapy, Cancer research 62(7) (2002) 2151-2156.

[28] C. Zhang, X. Cheng, M. Chen, J. Sheng, J. Ren, Z. Jiang, J. Cai, Y. Hu, Fluorescence guided photothermal/photodynamic ablation of tumours using pH-responsive chlorin e6-conjugated gold nanorods, Colloids Surf B Biointerfaces 160 (2017) 345-354.

[29] G.M. Calixto, J. Bernegossi, L.M. de Freitas, C.R. Fontana, M. Chorilli, Nanotechnology-Based Drug Delivery Systems for Photodynamic Therapy of Cancer: A Review, Molecules 21(3) (2016) 342.

[30] L. Song, G. Wang, X. Hou, S. Kala, Z. Qiu, K.F. Wong, F. Cao, L. Sun, Biogenic nanobubbles for effective oxygen delivery and enhanced photodynamic therapy of cancer, Acta Biomater (2020).

[31] D. Nowis, M. Makowski, T. Stokłosa, M. Legat, T. Issat, J. Gołąb, Direct tumor damage mechanisms of photodynamic therapy, Acta Biochimica Polonica 52(2) (2005) 339-352.

[32] B.C. Wilson, Photodynamic therapy for cancer: principles, Canadian Journal of Gastroenterology and Hepatology 16(6) (2002) 393-396.

[33] E. Christensen, T. Warloe, S. Kroon, J. Funk, P. Helsing, A.M. Soler, H.J. Stang, Ø. Vatne, C. Mørk, Guidelines for practical use of MAL-PDT in non-melanoma skin cancer, Journal of the European Academy of Dermatology and Venereology 24(5) (2010) 505-512.

[34] R. Szeimies, C.A. Morton, A. Sidoroff, L.R. Braathen, Photodynamic therapy for non-melanoma skin cancer, ACTA DERMATOVENEREOLOGICA-STOCKHOLM- 85(6) (2005) 483.

[35] L. Wyld, R.A. Audisio, G.J. Poston, The evolution of cancer surgery and future

perspectives, Nat Rev Clin Oncol 12(2) (2015) 115-24.

[36] M. Lafond, S. Yoshizawa, S.I. Umemura, Sonodynamic Therapy: Advances and Challenges in Clinical Translation, J Ultrasound Med 38(3) (2019) 567-580.

[37] X. Pan, H. Wang, S. Wang, X. Sun, L. Wang, W. Wang, H. Shen, H. Liu, Sonodynamic therapy (SDT): a novel strategy for cancer nanotheranostics, Sci China Life Sci 61(4) (2018) 415-426.

[38] L. Rengeng, Z. Qianyu, L. Yuehong, P. Zhongzhong, L. Libo, Sonodynamic therapy, a treatment developing from photodynamic therapy, Photodiagnosis Photodyn Ther 19 (2017) 159-166.

[39] G.Y. Wan, Y. Liu, B.W. Chen, Y.Y. Liu, Y.S. Wang, N. Zhang, Recent advances of sonodynamic therapy in cancer treatment, Cancer Biol Med 13(3) (2016) 325-338.

[40] H. Wang, P. Wang, L. Li, K. Zhang, X. Wang, Q. Liu, Microbubbles Enhance the Antitumor Effects of Sinoporphyrin Sodium Mediated Sonodynamic Therapy both In Vitro and In Vivo, Int J Biol Sci 11(12) (2015) 1401-9.

[41] A.K. Wood, C.M. Sehgal, A review of low-intensity ultrasound for cancer therapy, Ultrasound Med Biol 41(4) (2015) 905-28.

[42] Y. Wang, X. Li, Y. Zhou, P. Huang, Y. Xu, Preparation of nanobubbles for ultrasound imaging and intracelluar drug delivery, Int J Pharm 384(1-2) (2010) 148-53.

[43] Z. Xing, J. Wang, H. Ke, B. Zhao, X. Yue, Z. Dai, J. Liu, The fabrication of novel nanobubble ultrasound contrast agent for potential tumor imaging, Nanotechnology 21(14) (2010) 145607.

[44] T. Yin, P. Wang, R. Zheng, B. Zheng, D. Cheng, X. Zhang, X. Shuai, Nanobubbles for enhanced ultrasound imaging of tumors, Int J Nanomedicine 7 (2012) 895-904.

[45] T. van Rooij, V. Daeichin, I. Skachkov, N. de Jong, K. Kooiman, Targeted ultrasound contrast agents for ultrasound molecular imaging and therapy, Int J Hyperthermia 31(2) (2015) 90-106.

[46] S. Zullino, M. Argenziano, I. Stura, C. Guiot, R. Cavalli, From Micro- to Nano-Multifunctional Theranostic Platform: Effective Ultrasound Imaging Is Not Just a Matter of Scale,

Mol Imaging 17 (2018) 1536012118778216.

[47] A. Oren, The function of gas vesicles in halophilic archaea and bacteria: theories and experimental evidence, Life (Basel) 3(1) (2012) 1-20.

[48] F. Pfeifer, Distribution, formation and regulation of gas vesicles, Nat Rev Microbiol 10(10) (2012) 705-15.

[49] F. Pfeifer, Haloarchaea and the formation of gas vesicles, Life (Basel) 5(1) (2015) 385-402.

[50] D.I. Piraner, A. Farhadi, H.C. Davis, D. Wu, D. Maresca, J.O. Szablowski, M.G. Shapiro, Going Deeper: Biomolecular Tools for Acoustic and Magnetic Imaging and Control of Cellular Function, Biochemistry 56(39) (2017) 5202-5209.

[51] M.G. Shapiro, P.W. Goodwill, A. Neogy, M. Yin, F.S. Foster, D.V. Schaffer, S.M. Conolly, Biogenic gas nanostructures as ultrasonic molecular reporters, Nat Nanotechnol 9(4) (2014) 311-6.

[52] T. Hussain, Q.T. Nguyen, Molecular imaging for cancer diagnosis and surgery, Adv Drug Deliv Rev 66 (2014) 90-100.

[53] H. Chen, Z. Zhen, T. Todd, P.K. Chu, J. Xie, Nanoparticles for Improving Cancer Diagnosis, Mater Sci Eng R Rep 74(3) (2013) 35-69.

[54] Y. Yang, Z. Qiu, X. Hou, L. Sun, Ultrasonic Characteristics and Cellular Properties of Anabaena Gas Vesicles, Ultrasound Med Biol 43(12) (2017) 2862-2870.

[55] M.S. Muthu, D.T. Leong, L. Mei, S.S. Feng, Nanotheranostics - application and further development of nanomedicine strategies for advanced theranostics, Theranostics 4(6) (2014) 660-77.

[56] K.K. Shung, Diagnostic Ultrasound: Past, Present, and Future, Journal of Medical and Biological Engineering 31(6) (2011).

[57] R. Guo, G. Lu, B. Qin, B. Fei, Ultrasound Imaging Technologies for Breast Cancer Detection and Management: A Review, Ultrasound Med Biol 44(1) (2018) 37-70.

[58] Q. Huang, Z. Zeng, A Review on Real-Time 3D Ultrasound Imaging Technology, Biomed Res Int 2017 (2017) 6027029.

[59] L. Abou-Elkacem, S.V. Bachawal, J.K. Willmann, Ultrasound molecular imaging: Moving

toward clinical translation, Eur J Radiol 84(9) (2015) 1685-1693.

[60] N. Deshpande, A. Needles, J.K. Willmann, Molecular ultrasound imaging: current status and future directions, Clin Radiol 65(7) (2010) 567-81.

[61] S. Hernot, A.L. Klibanov, Microbubbles in ultrasound-triggered drug and gene delivery, Adv Drug Deliv Rev 60(10) (2008) 1153-66.

[62] D. Cosgrove, C. Harvey, Clinical uses of microbubbles in diagnosis and treatment, Med Biol Eng Comput 47(8) (2009) 813-26.

[63] J. Shi, P.W. Kantoff, R. Wooster, O.C. Farokhzad, Cancer nanomedicine: progress, challenges and opportunities, Nat Rev Cancer 17(1) (2017) 20-37.

[64] S. Son, H.S. Min, D.G. You, B.S. Kim, I.C. Kwon, Echogenic nanoparticles for ultrasound technologies: Evolution from diagnostic imaging modality to multimodal theranostic agent, Nano Today 9(4) (2014) 525-540.

[65] W.B. Cai, H.L. Yang, J. Zhang, J.K. Yin, Y.L. Yang, L.J. Yuan, L. Zhang, Y.Y. Duan, The Optimized Fabrication of Nanobubbles as Ultrasound Contrast Agents for Tumor Imaging, Sci Rep 5 (2015) 13725.

[66] J. Zhang, Y. Chen, C. Deng, L. Zhang, Z. Sun, J. Wang, Y. Yang, Q. Lv, W. Han, M. Xie, The Optimized Fabrication of a Novel Nanobubble for Tumor Imaging, Front Pharmacol 10 (2019) 610.

[67] A. Lakshmanan, A. Farhadi, S.P. Nety, A. Lee-Gosselin, R.W. Bourdeau, D. Maresca, M.G. Shapiro, Molecular Engineering of Acoustic Protein Nanostructures, ACS Nano 10(8) (2016) 7314-22.

[68] R.W. Bourdeau, A. Lee-Gosselin, A. Lakshmanan, A. Farhadi, S.R. Kumar, S.P. Nety, M.G. Shapiro, Acoustic reporter genes for noninvasive imaging of microorganisms in mammalian hosts, Nature 553(7686) (2018) 86-90.

[69] J. Le Floc'h, A. Zlitni, H.A. Bilton, M. Yin, A. Farhadi, N.R. Janzen, M.G. Shapiro, J.F. Valliant, F.S. Foster, In vivo Biodistribution of Radiolabeled Acoustic Protein Nanostructures, Mol Imaging Biol 20(2) (2018) 230-239.

[70] K.Y. Choi, K.H. Min, H.Y. Yoon, K. Kim, J.H. Park, I.C. Kwon, K. Choi, S.Y. Jeong,

PEGylation of hyaluronic acid nanoparticles improves tumor targetability in vivo, Biomaterials 32(7) (2011) 1880-9.

[71] K.H. Min, J.H. Kim, S.M. Bae, H. Shin, M.S. Kim, S. Park, H. Lee, R.W. Park, I.S. Kim, K. Kim, I.C. Kwon, S.Y. Jeong, D.S. Lee, Tumoral acidic pH-responsive MPEG-poly(beta-amino ester) polymeric micelles for cancer targeting therapy, J Control Release 144(2) (2010) 259-66.

[72] A.N. Koo, H.J. Lee, S.E. Kim, J.H. Chang, C. Park, C. Kim, J.H. Park, S.C. Lee, Disulfide-cross-linked PEG-poly(amino acid)s copolymer micelles for glutathione-mediated intracellular drug delivery, Chem Commun (Camb) (48) (2008) 6570-2.

[73] L.J. Cruz, P.J. Tacken, R. Fokkink, C.G. Figdor, The influence of PEG chain length and targeting moiety on antibody-mediated delivery of nanoparticle vaccines to human dendritic cells, Biomaterials 32(28) (2011) 6791-803.

[74] V.M. Platt, F.C. Szoka, Jr., Anticancer therapeutics: targeting macromolecules and nanocarriers to hyaluronan or CD44, a hyaluronan receptor, Mol Pharm 5(4) (2008) 474-86.

[75] E. Auzenne, S.C. Ghosh, M. Khodadadian, B. Rivera, D. Farquhar, R.E. Price, M. Ravoori, V. Kundra, R.S. Freedman, J. Klostergaard, Hyaluronic acid-paclitaxel: antitumor efficacy against CD44(+) human ovarian carcinoma xenografts, Neoplasia 9(6) (2007) 479-86.

[76] J.D. Byrne, T. Betancourt, L. Brannon-Peppas, Active targeting schemes for nanoparticle systems in cancer therapeutics, Adv Drug Deliv Rev 60(15) (2008) 1615-26.

[77] J. Huang, H. Zhang, Y. Yu, Y. Chen, D. Wang, G. Zhang, G. Zhou, J. Liu, Z. Sun, D. Sun, Y. Lu, Y. Zhong, Biodegradable self-assembled nanoparticles of poly (D,L-lactide-co-glycolide)/hyaluronic acid block copolymers for target delivery of docetaxel to breast cancer, Biomaterials 35(1) (2014) 550-66.

[78] H.S. Qhattal, X. Liu, Characterization of CD44-mediated cancer cell uptake and intracellular distribution of hyaluronan-grafted liposomes, Mol Pharm 8(4) (2011) 1233-46.

[79] K.Y. Choi, K.H. Min, J.H. Na, K. Choi, K. Kim, J.H. Park, I.C. Kwon, S.Y. Jeong, Self-assembled hyaluronic acid nanoparticles as a potential drug carrier for cancer therapy: synthesis, characterization, and in vivo biodistribution, Journal of Materials Chemistry 19(24) (2009) 4102-4107.

[80] K.Y. Choi, H. Chung, K.H. Min, H.Y. Yoon, K. Kim, J.H. Park, I.C. Kwon, S.Y. Jeong, Self-assembled hyaluronic acid nanoparticles for active tumor targeting, Biomaterials 31(1) (2010) 106-114.

[81] S. Honary, F. Zahir, Effect of Zeta Potential on the Properties of Nano-Drug Delivery Systems - A Review (Part 2), Tropical Journal of Pharmaceutical Research 12(2) (2013).

[82] S. Dallavalle, V. Dobricic, L. Lazzarato, E. Gazzano, M. Machuqueiro, I. Pajeva, I. Tsakovska, N. Zidar, R. Fruttero, Improvement of conventional anti-cancer drugs as new tools against multidrug resistant tumors, Drug Resist Updat 50 (2020) 100682.

[83] G. Delaney, S. Jacob, C. Featherstone, M. Barton, The role of radiotherapy in cancer treatment: estimating optimal utilization from a review of evidence-based clinical guidelines, Cancer 104(6) (2005) 1129-37.

[84] L. Song, Y. Huang, X. Hou, Y. Yang, S. Kala, Z. Qiu, R. Zhang, L. Sun, PINK1/Parkin-Mediated Mitophagy Promotes Resistance to Sonodynamic Therapy, Cell Physiol Biochem 49(5) (2018) 1825-1839.

[85] W. Duco, V. Grosso, D. Zaccari, A.T. Soltermann, Generation of ROS mediated by mechanical waves (ultrasound) and its possible applications, Methods 109 (2016) 141-148.

[86] S. Son, J.H. Kim, X. Wang, C. Zhang, S.A. Yoon, J. Shin, A. Sharma, M.H. Lee, L. Cheng, J. Wu, J.S. Kim, Multifunctional sonosensitizers in sonodynamic cancer therapy, Chem Soc Rev (2020).

[87] E. Beguin, S. Shrivastava, N.V. Dezhkunov, A.P. McHale, J.F. Callan, E. Stride, Direct Evidence of Multibubble Sonoluminescence Using Therapeutic Ultrasound and Microbubbles, ACS Appl Mater Interfaces 11(22) (2019) 19913-19919.

[88] Y. Lin, L. Lin, M. Cheng, L. Jin, L. Du, T. Han, L. Xu, A.C.H. Yu, P. Qin, Effect of acoustic parameters on the cavitation behavior of SonoVue microbubbles induced by pulsed ultrasound, Ultrason Sonochem 35(Pt A) (2017) 176-184.

[89] K.B. Bader, E. Vlaisavljevich, A.D. Maxwell, For Whom the Bubble Grows: Physical Principles of Bubble Nucleation and Dynamics in Histotripsy Ultrasound Therapy, Ultrasound Med Biol 45(5) (2019) 1056-1080.

[90] A. Gnanaskandan, C.T. Hsiao, G. Chahine, Modeling of Microbubble-Enhanced High-Intensity Focused Ultrasound, Ultrasound Med Biol 45(7) (2019) 1743-1761.

[91] J.O. Szablowski, A. Bar-Zion, M.G. Shapiro, Achieving Spatial and Molecular Specificity with Ultrasound-Targeted Biomolecular Nanotherapeutics, Acc Chem Res 52(9) (2019) 2427-2434.

[92] G. Wang, L. Song, X. Hou, S. Kala, K.F. Wong, L. Tang, Y. Dai, L. Sun, Surface-modified GVs as nanosized contrast agents for molecular ultrasound imaging of tumor, Biomaterials 236 (2020) 119803.

[93] B. Muz, P. de la Puente, F. Azab, A.K. Azab, The role of hypoxia in cancer progression, angiogenesis, metastasis, and resistance to therapy, Hypoxia (Auckl) 3 (2015) 83-92.

[94] M.C. Bosco, G. D'Orazi, D. Del Bufalo, Targeting hypoxia in tumor: a new promising therapeutic strategy, J Exp Clin Cancer Res 39(1) (2020) 8.

[95] X. Zhou, H. Liu, Y. Zheng, Y. Han, T. Wang, H. Zhang, Q. Sun, Z. Li, Overcoming Radioresistance in Tumor Therapy by Alleviating Hypoxia and Using HIF-1 Inhibitor, ACS Applied Materials & Interfaces (2020).

[96] I. Moen, L.E. Stuhr, Hyperbaric oxygen therapy and cancer--a review, Target Oncol 7(4) (2012) 233-42.

[97] K. Stepien, R.P. Ostrowski, E. Matyja, Hyperbaric oxygen as an adjunctive therapy in treatment of malignancies, including brain tumours, Med Oncol 33(9) (2016) 101.

[98] M. Heyboer, 3rd, D. Sharma, W. Santiago, N. McCulloch, Hyperbaric Oxygen Therapy: Side Effects Defined and Quantified, Adv Wound Care (New Rochelle) 6(6) (2017) 210-224.

[99] S. Moradi, A. Jahanian-Najafabadi, M.H. Roudkenar, Artificial Blood Substitutes: First Steps on the Long Route to Clinical Utility, Clin Med Insights Blood Disord 9 (2016) 33-41.

[100] F. Alam, N. Yadav, M. Ahmad, M. Shadan, Blood substitutes: possibilities with nanotechnology, Indian J Hematol Blood Transfus 30(3) (2014) 155-62.

[101] C.L. Varnado, T.L. Mollan, I. Birukou, B.J. Smith, D.P. Henderson, J.S. Olson, Development of recombinant hemoglobin-based oxygen carriers, Antioxid Redox Signal 18(17) (2013) 2314-28.

[102] J.R. Eisenbrey, L. Albala, M.R. Kramer, N. Daroshefski, D. Brown, J.B. Liu, M. Stanczak,

P. O'Kane, F. Forsberg, M.A. Wheatley, Development of an ultrasound sensitive oxygen carrier for oxygen delivery to hypoxic tissue, Int J Pharm 478(1) (2015) 361-367.

[103] S.M. Fix, M.A. Borden, P.A. Dayton, Therapeutic gas delivery via microbubbles and liposomes, J Control Release 209 (2015) 139-49.

[104] J.J. Kwan, M. Kaya, M.A. Borden, P.A. Dayton, Theranostic oxygen delivery using ultrasound and microbubbles, Theranostics 2(12) (2012) 1174-84.

[105] E.J. Swanson, V. Mohan, J. Kheir, M.A. Borden, Phospholipid-stabilized microbubble foam for injectable oxygen delivery, Langmuir 26(20) (2010) 15726-9.

[106] M.S. Khan, J. Hwang, K. Lee, Y. Choi, K. Kim, H.J. Koo, J.W. Hong, J. Choi, Oxygen-Carrying Micro/Nanobubbles: Composition, Synthesis Techniques and Potential Prospects in Photo-Triggered Theranostics, Molecules 23(9) (2018).

[107] T. Luo, J. Sun, S. Zhu, J. He, L. Hao, L. Xiao, Y. Zhu, Q. Wang, X. Pan, Z. Wang, S. Chang, Ultrasound-mediated destruction of oxygen and paclitaxel loaded dual-targeting microbubbles for intraperitoneal treatment of ovarian cancer xenografts, Cancer Lett 391 (2017) 1-11.

[108] J.R. Eisenbrey, R. Shraim, J.B. Liu, J. Li, M. Stanczak, B. Oeffinger, D.B. Leeper, S.W. Keith, L.J. Jablonowski, F. Forsberg, P. O'Kane, M.A. Wheatley, Sensitization of Hypoxic Tumors to Radiation Therapy Using Ultrasound-Sensitive Oxygen Microbubbles, Int J Radiat Oncol Biol Phys 101(1) (2018) 88-96.

[109] B.D. Polizzotti, L.M. Thomson, D.W. O'Connell, F.X. McGowan, J.N. Kheir, Optimization and characterization of stable lipid-based, oxygen-filled microbubbles by mixture design, J Biomed Mater Res B Appl Biomater 102(6) (2014) 1148-56.

[110] J.N. Kheir, B.D. Polizzotti, L.M. Thomson, D.W. O'Connell, K.J. Black, R.W. Lee, J.N. Wilking, A.C. Graham, D.C. Bell, F.X. McGowan, Bulk manufacture of concentrated oxygen gas-filled microparticles for intravenous oxygen delivery, Adv Healthc Mater 2(8) (2013) 1131-41.

[111] K.H. Martin, P.A. Dayton, Current status and prospects for microbubbles in ultrasound theranostics, Wiley Interdiscip Rev Nanomed Nanobiotechnol 5(4) (2013) 329-45.

[112] C. Liu, F. Yan, Y. Xu, H. Zheng, L. Sun, InVivo Molecular Ultrasound Assessment of

Glioblastoma Neovasculature with Endoglin-Targeted Microbubbles, Contrast Media Mol Imaging 2018 (2018) 8425495.

[113] Y. Nakamura, A. Mochida, P.L. Choyke, H. Kobayashi, Nanodrug Delivery: Is the Enhanced Permeability and Retention Effect Sufficient for Curing Cancer?, Bioconjug Chem 27(10) (2016) 2225-2238.

[114] R. Ngoune, A. Peters, D. von Elverfeldt, K. Winkler, G. Putz, Accumulating nanoparticles by EPR: A route of no return, J Control Release 238 (2016) 58-70.

[115] R. Cavalli, A. Bisazza, P. Giustetto, A. Civra, D. Lembo, G. Trotta, C. Guiot, M. Trotta, Preparation and characterization of dextran nanobubbles for oxygen delivery, Int J Pharm 381(2) (2009) 160-5.

[116] R. Song, D. Hu, H.Y. Chung, Z. Sheng, S. Yao, Lipid-Polymer Bilaminar Oxygen Nanobubbles for Enhanced Photodynamic Therapy of Cancer, ACS Appl Mater Interfaces 10(43) (2018) 36805-36813.

[117] M.S. Khan, J. Hwang, Y. Seo, K. Shin, K. Lee, C. Park, Y. Choi, J.W. Hong, J. Choi, Engineering oxygen nanobubbles for the effective reversal of hypoxia, Artif Cells Nanomed Biotechnol 46(sup3) (2018) S318-S327.

[118] M.S. Khan, J. Hwang, K. Lee, Y. Choi, J. Jang, Y. Kwon, J.W. Hong, J. Choi, Surface Composition and Preparation Method for Oxygen Nanobubbles for Drug Delivery and Ultrasound Imaging Applications, Nanomaterials (Basel) 9(1) (2019).

[119] H.S. Min, D.G. You, S. Son, S. Jeon, J.H. Park, S. Lee, I.C. Kwon, K. Kim, Echogenic Glycol Chitosan Nanoparticles for Ultrasound-Triggered Cancer Theranostics, Theranostics 5(12) (2015) 1402-18.

[120] D. Maresca, A. Lakshmanan, M. Abedi, A. Bar-Zion, A. Farhadi, G.J. Lu, J.O. Szablowski, D. Wu, S. Yoo, M.G. Shapiro, Biomolecular Ultrasound and Sonogenetics, Annu Rev Chem Biomol Eng 9 (2018) 229-252.

[121] D. van Straten, V. Mashayekhi, H.S. de Bruijn, S. Oliveira, D.J. Robinson, Oncologic Photodynamic Therapy: Basic Principles, Current Clinical Status and Future Directions, Cancers (Basel) 9(2) (2017).

[122] C. Zhang, J. Ren, J. Hua, L. Xia, J. He, D. Huo, Y. Hu, Multifunctional Bi2WO6 Nanoparticles for CT-Guided Photothermal and Oxygen-free Photodynamic Therapy, ACS Appl Mater Interfaces 10(1) (2018) 1132-1146.

[123] P. Zhao, S. Ren, Y. Liu, W. Huang, C. Zhang, J. He, PL-W18O49-TPZ Nanoparticles for Simultaneous Hypoxia-Activated Chemotherapy and Photothermal Therapy, ACS Appl Mater Interfaces 10(4) (2018) 3405-3413.

[124] H. Zuo, J. Tao, H. Shi, J. He, Z. Zhou, C. Zhang, Platelet-mimicking nanoparticles co-loaded with W18O49 and metformin alleviate tumor hypoxia for enhanced photodynamic therapy and photothermal therapy, Acta Biomater 80 (2018) 296-307.

[125] F. Xu, A. Bandara, H. Akiyama, B. Eshaghi, D. Stelter, T. Keyes, J.E. Straub, S. Gummuluru, B.M. Reinhard, Membrane-wrapped nanoparticles probe divergent roles of GM3 and phosphatidylserine in lipid-mediated viral entry pathways, Proc Natl Acad Sci U S A 115(39) (2018) E9041-E9050.

[126] F. Tamura, Y. Tanimoto, R. Nagai, F. Hayashi, K. Morigaki, Self-Spreading of Phospholipid Bilayer in a Patterned Framework of Polymeric Bilayer, Langmuir 35(45) (2019) 14696-14703.

[127] D. Stelter, T. Keyes, Lipid Packing in Lipid-Wrapped Nanoparticles, J Phys Chem B 122(26) (2018) 6755-6762.

[128] J.C. Kraft, R.J. Ho, Interactions of indocyanine green and lipid in enhancing near-infrared fluorescence properties: the basis for near-infrared imaging in vivo, Biochemistry 53(8) (2014) 1275-83.

[129] T. Burkholder, C. Foltz, E. Karlsson, C.G. Linton, J.M. Smith, Health Evaluation of Experimental Laboratory Mice, Current protocols in mouse biology 2 (2012) 145-165.

[130] M.A. Borden, M.L. Longo, Oxygen Permeability of Fully Condensed Lipid Monolayers, The Journal of Physical Chemistry B 108(19) (2004) 6009-6016.

[131] J.J. Kwan, M.A. Borden, Lipid monolayer dilatational mechanics during microbubble gas exchange, Soft Matter 8(17) (2012).